國立臺灣大學理學院地質科學系

碩士論文

Department of Geosciences

College of Science

National Taiwan University

Master Thesis

利用永久散射體雷達干涉技術分析地表變形：以臺灣西南部平原為例

Analysis of surface deformation based on PS-InSAR technique: Case studies in coastal plain, SW Taiwan

童　忻

Hsin Tung

指導教授：胡植慶 博士

Advisor: Jyr-Ching Hu, Ph.D.

中華民國 97 年 7 月

July, 2008

國立臺灣大學碩士學位論文
口試委員會審定書

利用永久散射體雷達干涉技術分析地表變形 ：

以臺灣西南部平原為例

Analysis of surface deformation based on PS-InSAR technique: Case studies in coastal plain, SW Taiwan

本論文係童忻君（R95224206）在國立臺灣大學地質科學所完成之碩士學位論文，於民國九十七年七月九日承下列考試委員審查通過及口試及格，特此證明

口試委員：胡植慶（簽名）

（指導教授）

余騰鐸　　謝嘉聲

陳文山

Abstract

Differential Interferometric Synthetic Aperture Radar (DInSAR) technique has increasingly been applied in geosciences as a powerful tool to monitor land surface deformation. In addition, the large archives of SAR data enable us to monitor ground deformation continually. However, temporal and spatial decorrelations of radar signal have prevented this technique from more frequent utilization. An advanced InSAR processing technique that tracks the signals of discreted point-wise targets called Persistent Scatterers Interferometry Technique (PSInSAR) was herein applied to our research area in order to better understand the deformation patterns. Thus the PSInSAR method allows us to know the deformation of these discrete points that were minimally affected by decorrelation of radar signals through time.

The active orogeny of Taiwan generated large amount of surface deformation that were partitioned throughout the island, which provides a great opportunity for analyzing tectonic displacements through interferometric methods. Here we present a PS-InSAR result deduced from 1996-1999 time spans in and around Tainan Tableland of southwestern Taiwan close to the deformation front. About 1,650 persistent scatterers are deduced from the processing of 33 SAR images (Tract: 232, frame, 3141) in an area of 144 km^2. The maximum slant range displacement (SRD) rate along the radar line of sight (LOS) toward to satellite is about 8 mm which is close to the borehole data after transferring SRD rate to vertical deformation rate. Besides, the nonlinear deformation evolutions show a respectable correlation with seasonal rainfall on the Tainan Tableland near the Houchiali fault. One of the reasons might be the behaviors of fault creeping during the rainy seasons. These results indicate that the Tainan Tableland is an aseismic area.

In addition, anthropogenic ground subsidence due to massive pumping of groundwater is one of problems in Taiwan. The Yunlin County located in the southwestern coastal region of Taiwan is one of the most counties with serious land subsidence because of the agricultural needs. Here, we also represented a both stacking DInSAR and PSInSAR results deduced from 1996-1999 time spans for monitoring of land subsidence in this area. Both DInSAR and PSInSAR results show the Baojhou, Tuku Township and northern Mailiao reveal a maximum subsidence rate of about 6 cm/yr along LOS and the Taishi Township located on the coastal area reveals a subsidence rate of 1.58 cm/yr, which is quite coincident with precise leveling result. These two results have proven that the effective reduction of labor and cost could be achieved by using this technique on monitoring land subsidence in Yunlin County.

Key words: InSAR, DInSAR, PSInSAR, Tainan Tableland, Houchiali Fault, Tawan Lowland, Yunlin County, Surface Deformation, Land Subsidence.

摘要

近年來，差分合成孔徑雷達干涉技術已經成為地球科學研究上一項利於觀測地表變形的工具。透過所獲取的大量影像，有助於我們更能夠連續性的觀測地表變形。但是，雷達訊號隨著空間基線的增大和時間的增長，降低雷達訊號的相關性，限制了此項技術無法更廣泛的應用。永久散射體雷達干涉技術，利用萃取分散的穩定點目標，能有效克服時間以及空間上低相關的限制；因此，本研究將此項技術應用在所選取的研究區域內，以期能更清楚的了解地表變化的時空演變。

台灣位於歐亞大陸板塊與菲律賓海板塊之間的碰撞縫合帶，構造活動相當劇烈，提供了差分合成孔徑雷達干涉技術一個良好的材料來分析地表變形。本研究利用 1996 年至 2000 年間所接收的 33 張雷達影像，以永久散射體雷達干涉技術分析位於變形前緣的台南台地之地表變形；在 144 平方公里區域內，挑選約有 1,650 個永久散射點做為分析的點目標。分析結果顯示，台南台地上最大視衛星方向上的抬升速率為每年 8 公厘，將其座標轉換至垂直方向上的抬升速率，與層序沉積定年的結果相當接近，暗示此區長期抬升速率與短期抬升速率相近，屬於無震區。除此之外，靠近後甲里斷層的永久散射體的變形行為皆呈現出與季節性降雨有高度的相關性，其原因可能是斷層在雨季發生潛移活動的行為，呼應了此區為無震區的推論，但此推論還需要更多的測量結果才能確定。

除了構造活動外，人為活動也是造成地表位移的原因之一。台灣西南沿海的雲林縣是以農業為主的區域，因灌溉而長期抽取地下水造成此地區地層下陷的情況相當嚴重；因此，本研究再利用累加差分合成孔徑雷達干涉技術與永久散射體干涉技術，監測雲林地區 1996 年至 1999 年 6 月間的地層下陷時空演變。兩項結果都顯示出，位於內陸的褒忠鄉、土庫鄉以及麥寮鄉北部區域擁有最大的下陷量，約為每年 6 公分，沿海地區的台西鄉則呈現出每年 1.58 公分的下陷量，與精密水準測量結果相當吻合。此結果證明了利用此項技術，能夠有效的減少人力以及財力的花費，得到雲林地區地層下陷點狀以及面狀的資訊。

關鍵字：差分合成孔徑雷達干涉技術、永久散射體雷達干涉技術、台南台地、後甲里斷層、大灣低地、雲林縣、地表變形、地層下陷。

致謝

兩年的研究所生涯，終於告一段落。這一篇論文能夠順利完成，首先要感謝我的指導老師－胡植慶博士；感謝老師在研究以及課業方面的協助，給我極高的自由度，讓我能夠選擇有興趣的研究目標與方向。在遙測的世界裡，我很開心。再來要感謝我的口試委員，陳文山博士、余騰鐸博士、謝嘉聲博士以及顏君毅博士，於學生口試期間撥冗擔任我的口試委員，對於本論文以及研究上不足之處給予非常多的指導和幫助，使本論文接近完整。陳文山老師在地質解釋方面多次的教導，提供了我遙測以外的資料與觀念。余騰鐸老師是讓我對遙測產生興趣的最初原因，慶幸自己能在大學時遇見了老師，真的非常感謝。謝嘉聲老師總是提供我另外一層思考，也給與我很大的肯定，讓我有信心走下去。顏君毅老師時常一大早就被我用 MSN 攻擊，還要一直忍受我的糾纏與笨，如果沒有你，我應該早就放棄了吧。除此之外，盧佳遇博士與中央大學張中白博士教導了我許多報告上以及研究上的要領，從老師身上，我得到不只是研究上面的精進，還有更多處事的態度。真的感謝各位老師，希望我還有機會能向各位老師學習。

除此之外，要特別感謝香港理工大學丁曉利博士、大陸西南交通大學劉國祥博士以及陳強博士；有了你們的協助，讓我度過了研究途中最大的瓶頸，成功的在今年達成目標，順利畢業。另外提供論文重要資料的吳逸民老師、賈儀平老師，饒瑞鈞博士以及成功大學的志憲，感謝有你們，我的論文才能完整。

再來，我要感謝黃孟涵學長，幫我一點一點的建立遙測的觀念，就像是我的指導老師一般；一起工作的週末，台灣中部、南部都有我們工作的紀錄，真的謝謝你對我的百般協助。而四人小組中善解人意的雅琳、聰明認真的黃蓉、氣質出眾的婷兒，加上採購部主任宜芬，真的是我這段期間最美好也最捨不得的回憶。感謝妳們在我傷心、開心的時候在我身邊，聆聽我的煩惱，解決我的問題，在這段期間備受妳們的照顧。有妳們在身邊，是我每天開心的原動力，超愛妳們的，希望有機會再一起工作唷。

另外，實驗室一起奮鬥的顏色、詠恬，以及昭榮學長、育雅老師、宜蓉、佳漢、黃鐘、蚯蚓、冠全、彭彭、Maple、偉聖，謝謝你們這段日子的包容。中央的貓王、小黑、嘉貞、育芳、萬慧、勤怡、小熊、偉恆，認識你們，是我很大的收穫。乙君、踢哀恩、液晶、Ray、鴉哥、阿和、珀儂、信樺、阿天、林桑，因為有你們，我的研究生活才如此的充實與快樂。還有進上、張立、中正的學長姐們以及其他在這裡認識的好朋友們，兩年的時間，承蒙了大家的照顧，也祝福大家都能夠一切順心。

最後我想感謝的是我最重要的家人，爸爸媽媽和姊姊。謝謝爸爸媽媽每天辛苦的工作，讓我的學生生活無後顧之憂，還有忍受我回台北以來的壞脾氣；謝謝姊姊每天載我上學，讓我可以早早到學校工作。還要謝謝楹丰一直以來的陪伴。謝謝你們在生活上的照顧和支持，謹以此論文獻給我最愛的你們。

另外還有很多曾經幫助過我的朋友，因為有大家的幫助，我才能有今天的成果。謝謝大家。

Contents

List of Figures

Lists of Tables

Lists of Abbreviations

ALOS	advanced land observing satellite
CNES	Centre National D'Etudes Spatiales
CSA	Canadian Space Agency
CWB	Central Weather Bureau
DEM	digital elevation model
DEOS	Delft Institute of Earth oriented space research
DIAPASON	differential interferometric automated process applied to survey of nature
DInSAR	differential InSAR
EMD	empirical mode decomposition
ENVISAT	European Space Agency environment satellite
ERS	European Space Agency Earth remote sensing satellite
ESA	European Space Agency
EU	Eurasian plate
GPS	global positioning system
InSAR	interferometric synthetic aperture radar
ITRI	Industrial Technology Research Institute
JERS-1	Japanese Earth resources satellite-1
JPL	Jet Propulsion Laboratory
LOS	line of sight
NSDAJ	National Space Development Agency of Japan
NASA	National Aeronautics and Space Administration
PALSAR	phased array type L-band synthetic aperture radar
PS	persistent scatterers
PRF	pulse repetition frequency

PSP	Philippine Sea plate
Radar	radio detection and range
RAR	real aperture radar
SAR	synthetic aperture radar
SBAS	small baseline subset
SLAR	side-looking RAR
SNAPHU	statistical-cost, network-flow algorithm for phase unwrapping
SNR	signal to noise ratio
SRD	slant range displacement
SRTM	shuttle radar topography mission
StaMPS	Stanford method for persistent scatterers
THSR	Taiwan High Speed Rail
WRA	Water Resources Agency

Chapter 1

Introduction

國立臺灣大學 · 敦品勵學 · 愛國愛人

1.1 Motivation

Recently, **InSAR** (**In**terferometric **S**ynthetic **A**perture **R**adar) has been used widely in many fields such as glacial processes, landslide, terrain classifications, ocean current and vegetation parameters [*Massonnet and Feigl*, 1998; *Rosen et al.*, 2000] due to its "all weather" capability and the day/night access of the sensors. This remote-sensing tool distinguishes itself from other geodetic measurements in that requires no presence in the filed and is available worldwide. Basically, InSAR could map surface deformation at dense pixel of 20-100 m over almost unlimited spatial distances and is particularly sensitive to vertical displacements comparable to the precision of leveling measurements. As a result, InSAR is also applied to monitor crust deformation, volcanism and land subsidence [*Bürgmann et al.*, 2000].

Although spaceborne **D**ifferential **InSAR** (**DInSAR**) has already proven its potential for mapping ground deformation, the atmospheric perturbation and phase decorrelation have prevented conventional DInSAR from achieving full operational capability. On the other hand, the **P**ersistent **S**catterers (**PS**) technique is a powerful and fully operational tool for monitoring ground deformation on a high spatial density of point-wise targets by an extensive time series of SAR data [e.g. *Ferretti et al.*, 2000, 2001; *Colesanti et al.*, 2003]. Moreover, the analysis of pixel-by-pixel character of the phase stable targets makes it feasible to detect the ground deformation in dense vegetation or mountainous area as long as the men-made structures or exposed rocks are available.

Taiwan Island is located along a segment of the oblique convergent boundary between the **P**hilippine **S**ea **P**late (**PSP**) and **E**urasian **P**late (**EP**), where collision and subduction processes occur (Figure 1.1). The convergent rate between these two plates is about 82 mm/yr [*Yu et al.*, 1999; *Zang et al.*, 2002], due to this oblique convergence, the young Taiwan orogenic belt is an ideal natural laboratory to study the tectonic processes based on geodetic measurements. Consequently, the island-wide GPS (global positioning system) network was established from 1991 to meet acquirement of the assessment of seismic hazards [e.g., *Yu et al.*, 1997]. In addition, the conventional DInSAR has been applied to detect the coseismic deformation of the 1999 Chi-Chi earthquake [*Pathier et al.*, 2003; *Chang et al.*, 2004] and the active deformation in Tainan area [*Fruneau et al.*, 2001; *Huang et al.*, 2006]. However, the limitations of conventional DInSAR offer lots of uncertain of deformation measurements. Thus, one of the goals of this study is to apply PSInSAR technique and discuss the feasibility in Tainan area.

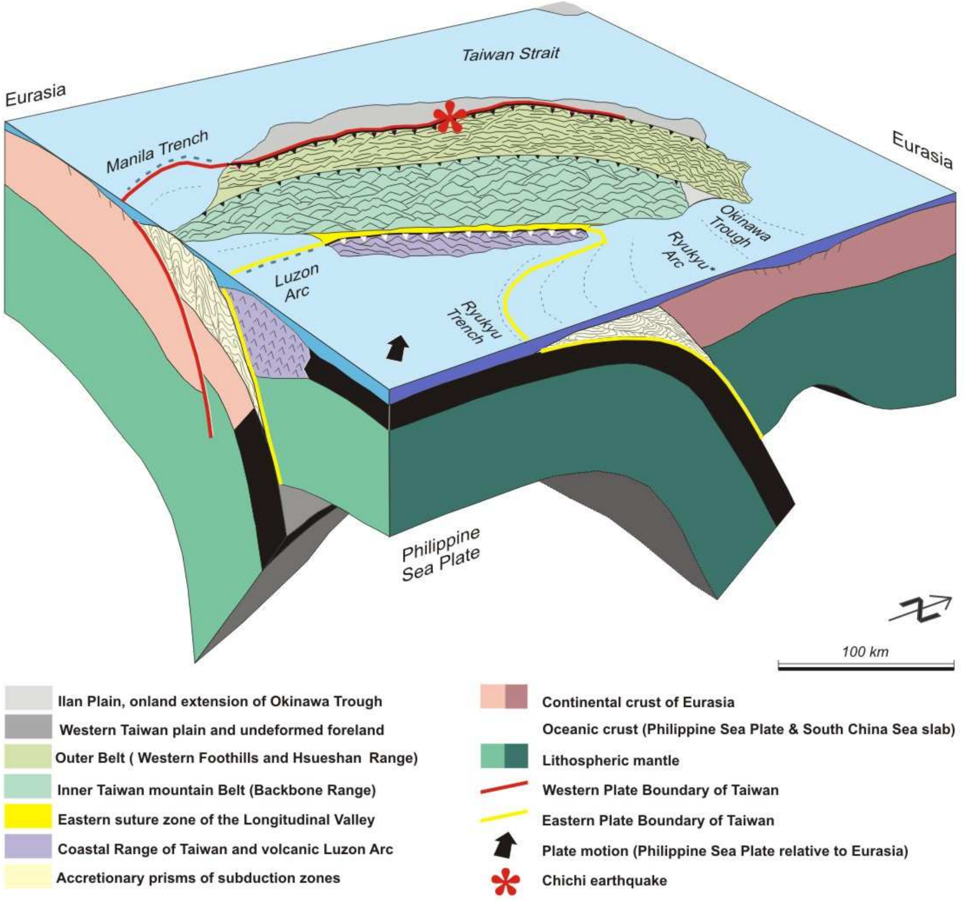

Figure 1.1. Tectonic framework of Taiwan in 3-D [*Angelier et al.*, 1999].

Ground subsidence induced by heavy withdrawal of groundwater has resulted in environmental hazard and potential risk in Taiwan (Figure 1.2), particularly in the Chou-Shui River alluvial fan where the Yunlin section of the **T**aiwan **H**igh **S**peed **R**ail (**THSR**) had been constructed. Seasonal effects of land subsidence occurring in the study area had been estimated using a regression analysis of a series of weekly GPS height solutions. The average rate of ground subsidence in this area over the period of 1995-2001 was 3 cm/yr. Based on data collected at the piezometer, the variation of land subsidence rate appears to be associated with an groundwater level, which drop gradually during winter and either remains constant or rises during summer time. Consequently, land subsidence rates vary considerably from 1.5 cm/yr for the summer time to 9.0 cm/yr for the winter time [*Chang and Wang*, 2006].

Therefore, the second aim of this study is to monitor land subsidence using SAR interferometry. However, due to the dense vegetation in Yunlin area, it is hard to get the time series distribution of land deformation by using conventional DInSAR technique. I used the stacking DInSAR and PSInSAR technique in order to obtain the temporal and spatial variations of land subsidence. For the PSInSAR technique, I adopt the idea from *Ferretti et al.* [2000, 2001] and *Mora et al.* [2003] to develop the programs for this study.

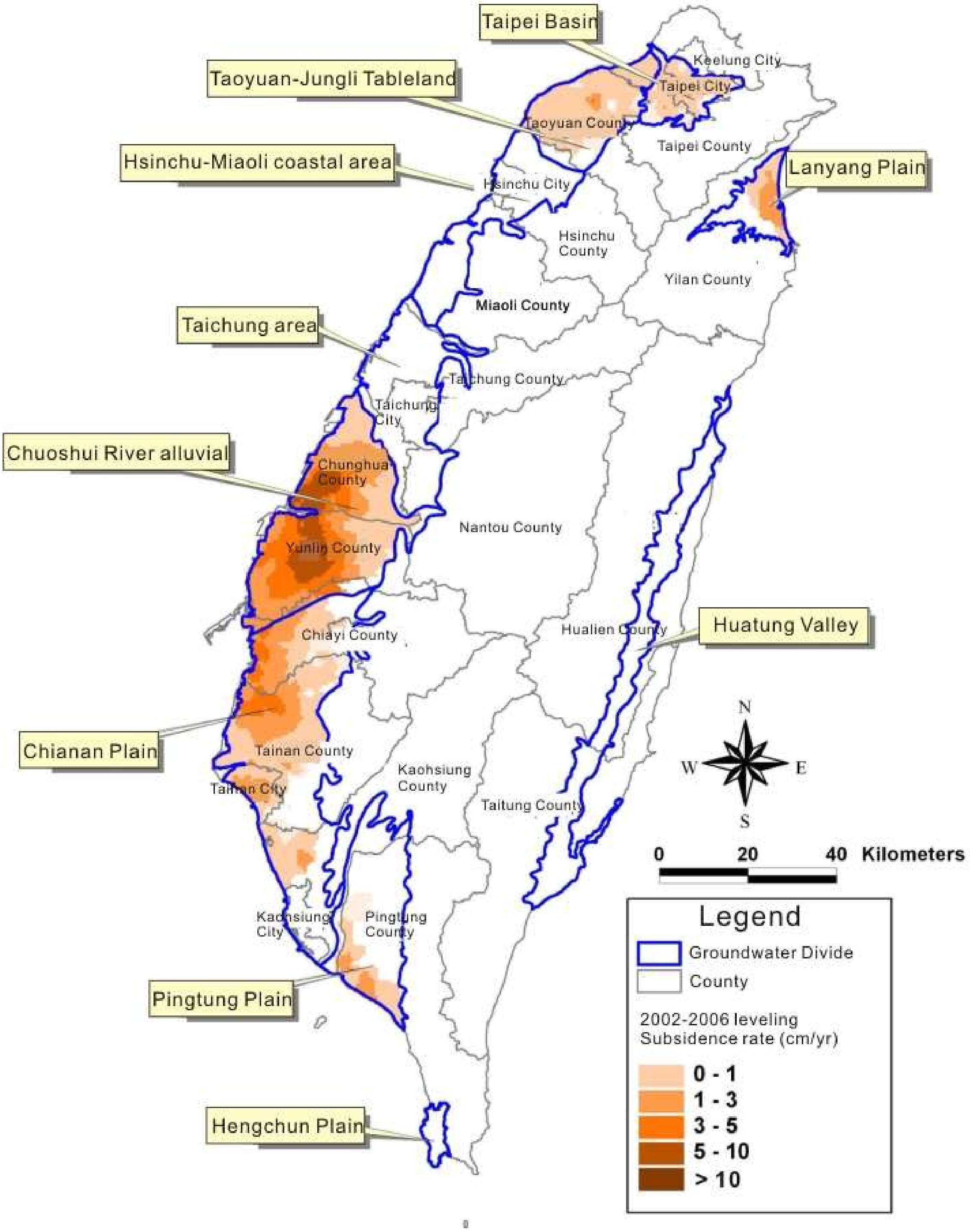

Figure 1.2. Average subsidence rate in Taiwan Island from 2002 to 2006 [*Land Subsidence Database*].

1.2 Spaceborne Radar History

Seasat is the first SAR mission in space lunched in July 1978 primarily for ocean studies by **NASA/JPL** (**N**ational **A**eronautics and **S**pace **A**dministration/**J**et **P**ropulsion **L**aboratory). It was a L-band (23 cm wavelength) synthetic aperture radar system with horizontal (HH) polarization. Unfortunately, it stopped operating after 99 days of lunching. However, the imagery was found to have a great deal of potential for scientific purposes.

Base on the success of Seasat, two shuttle missions of one week duration called *SIR-A* and *SIR-B* were operated in November 1981 and October 1984 respectively. Both *SIR-A* and *SIR-B* were L-band synthetic aperture radars with HH polarization. Unlike *Seasat* and *SIR-A* were recorded analogously on tapes, *SIR-B* was already equipped with full digital recording [*Hanssen*, 2001].

The **E**uropean **S**pace **A**gency (**ESA**) started to launch its first satellite equipped with a SAR in July 1991, the *ERS-1*. It was a C-band (5.66 cm wavelength) radar operating in VV polarization. In April 1995, an identical mission satellite named ***ERS****-2* (European Space Agency **E**arth **R**emote Sensing **S**atellite 2) was launched and put in the same orbit as *ERS-1*. From July 1995 to May 1996, six so-called 'tandem pair' were collected with an exact 24 hours interval between these two satellite.

The ***JERS-1*** (**J**apanese **E**arth **R**esources **S**atellite**-1**) was launched in early 1992 by **N**ational **S**pace **D**evelopment **A**gency of **J**apan (**NSDAJ**). The L-band gave choices of analyzing due to its capability of passing through the land surface.

Started in 1995, the **C**anadian **S**pace **A**gency (**CSA**) operated *Radarsat*, designed to perform ice coverage of Arctic. It was a C-band SAR system with HH polarization. It has several imaging modes with different incidence angle, resolution, and swath width providing various data for observations.

The ***ENVISAT*** (European Space Agency **Envi**ronment **sat**ellite) satellite was launched put in the same orbit as ERS-1/ERS-2 in February 2002 by ESA. It also has various imaging modes with different incidence angle, resolution, and swath width. In addition, the satellite has multi-polarization modes.

The **P**hased **A**rray type **L**-band **S**ynthetic **A**perture **R**adar (**PALSAR**) mounted on the ***ALOS*** (**A**dvanced **L**and **O**bserving **S**atellite) launched in January 2006 is the Japanese second-generation spaceborne SAR following the JERS-1. It is the first L-band SAR system with full-polarization.

1.3 Geodetic Data and Methodology

The SAR images used in this study were took by ERS-1 and ERS-2 launched by ESA. For the Tainan area in Chapter 3, 33 SAR images have been chosen during January 1996 to August 1999 from track 232, frame 3141. For the Yunlin area in chapter 4, 33 SAR images have been chosen during January 1996 to June 1999 from track 232, frame 3123 (Figure 1.3). In addition, the 'Precise Orbit' data are downloaded from the **D**elft Institute of **E**arth **O**riented **S**pace Research (**DEOS**).

The procedure of differential InSAR is processed by the software **DIAPASON** V4.0 (**D**ifferential **I**nterferometric **A**utomated **P**rocess **A**pplied to **S**urvey **o**f **N**ature) developed by **C**entre **N**ational D'**E**tudes **S**patiales (**CNES**), France, and now maintained by Altamira Information, Spain. The phase unwrapping procedure for Chapter 4 is processed by the software **SNAPHU** (**S**tatistical-Cost, **N**etwork-Flow **A**lgorithm for **Ph**ase **U**nwrapping) from Stanford University, USA. Furthermore, the

PSInSAR processes are compiled by MATLAB 7.1 language.

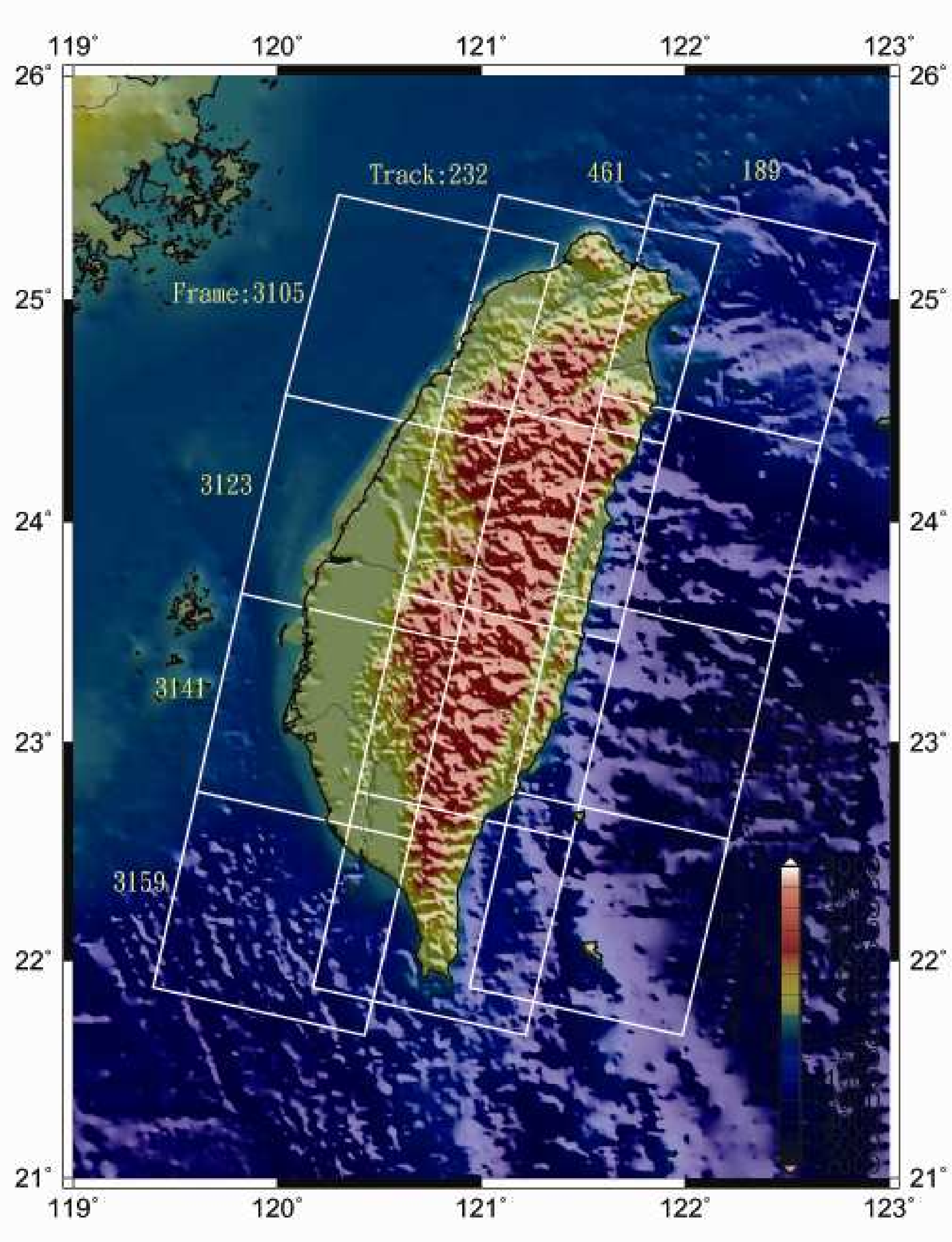

Figure 1.3. SAR images of track 232 and frames 3141 and 3123 are used in this study.

1.4 Thesis Roadmap

The aim of this study is to apply **p**ersistent **s**catterers **InSAR** (**PSInSAR**) technique on Tainan Tableland and Yunlin County caused by tectonic activity and land subsidence, respectively. First I introduce the principles of PSInSAR technique that have been published in scientific journals, and adopt these ideas to develop the procedurals of PSInSAR processes of our own.

Chapter 2 provides a brief overview of InSAR and then introduces the persistent scatterer InSAR methods used in this study. Chapter 3 is primarily concerned with the exactitude of procedures and concepts for isolating and extracting the deformation signal from persistent scatterer pixels. I apply this method on datasets from Tainan Tableland as a test site, and validate the technique by comparing results with sequence stratigraphy dating, precipitation, groundwater level data and seismicities. Chapter 4 demonstrates both conventional DInSAR and PSInSAR techniques applied in a land subsidence area, the Yunlin County, where dense vegetation causes significant perturbation of measuring by conventional DInSAR in wet seasons. As a consequence, I apply PSInSAR in order to obtain the deformation evolution close to the Yunlin section of THSR. Chapter 5 provides a summary of the thesis and suggestions for future work.

Chapter 2

Synthetic Aperture Radar Interferometry

2.1 Synthetic Aperture Radar

Radio **D**etection **a**nd **R**ange (**Radar**) is a technique to determine the distance between transmitter and target by emitting electromagnetic waves of microwave frequency and receiving the reflected signals. The usage of imaging the Earth by radar arose in late 1950s, but the first time came into scientific use by *Seasat* satellite built by JPL/NASA in 1987, which was the first task to analyse Earth by radar images [*Massonnet and Feigl*, 1998;].

Real **A**perture **R**adar (**RAR**) is the earliest radar image system, which was focused on measuring Earth surface. The resolution in the flight direction was obtained by using a physically long antenna. Figure 2.1 shows a **S**ide-**L**ooking R**AR** (**SLAR**) mounted on an aircraft or satellite to illuminate the Earth surface; hence it could receive the information on ground range by delay time. As the spacecraft traveled with a constant velocity along the flight direction, images on nearby area can be received continually. Nevertheless, the resolution in the flight direction (Ra) with constant wavelength λ was decided by the length of antenna (La).

$$Ra = \frac{\lambda}{La} \cdot \frac{h_{sat}}{\cos\theta} = \frac{\lambda}{La \cdot r} \tag{2- 1}$$

where h_{sat} is the height of satellite. Taking ERS1 for example, 25 meters azimuth resolution needs an antenna for 440 meters. It is unfeasible to carry an antenna with such size when traveling in the space.

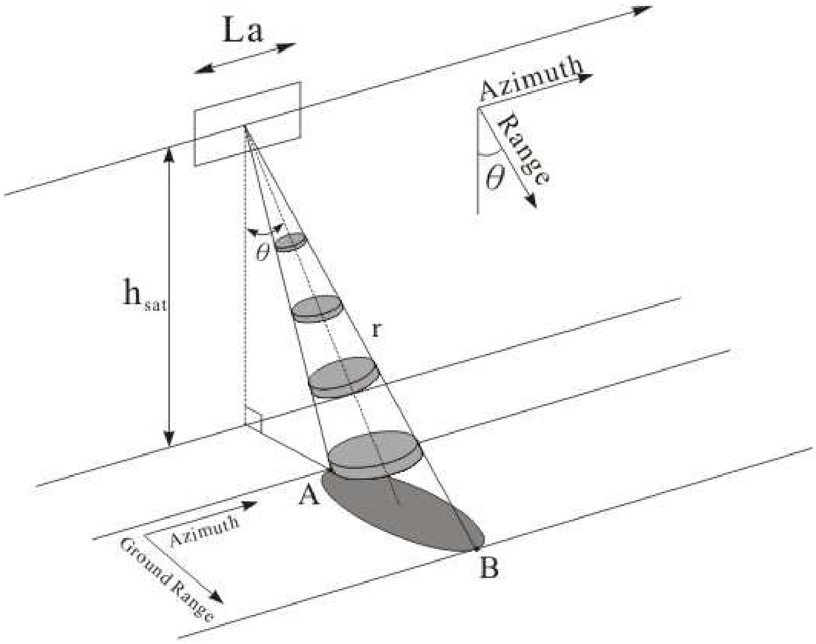

Figure 2.1. Imaging geometry of a RAR acquisition. The pulses illuminate a swath parallel to the satellite track. The resolution of footprint depends on antenna bandwidth and ground range. θ is the looking angle, r represents the range distance (modified from [*Hanssen*, 2001]).

In order to improve the azimuth resolution, fixed antenna is no longer used in an aircraft or a satellite. Thus, the **S**ynthetic **A**perture **R**adar (**SAR**) was developed. SAR system mounted on a moving spacecraft from position 1 to 11 around the Earth with a series of microwave pulses to illuminate the Earth surface (Figure 2.2). As the moving antenna passes, all return signals with different Doppler frequency shift from multiple locations were used to synthesize a large antenna. SAR system significantly improves the resolution of point target in both the cross-track (range) and along-track (azimuth) direction by focusing the raw radar echoes [*Elachi*, 1988; *Curlander and McDonough*, 1991].

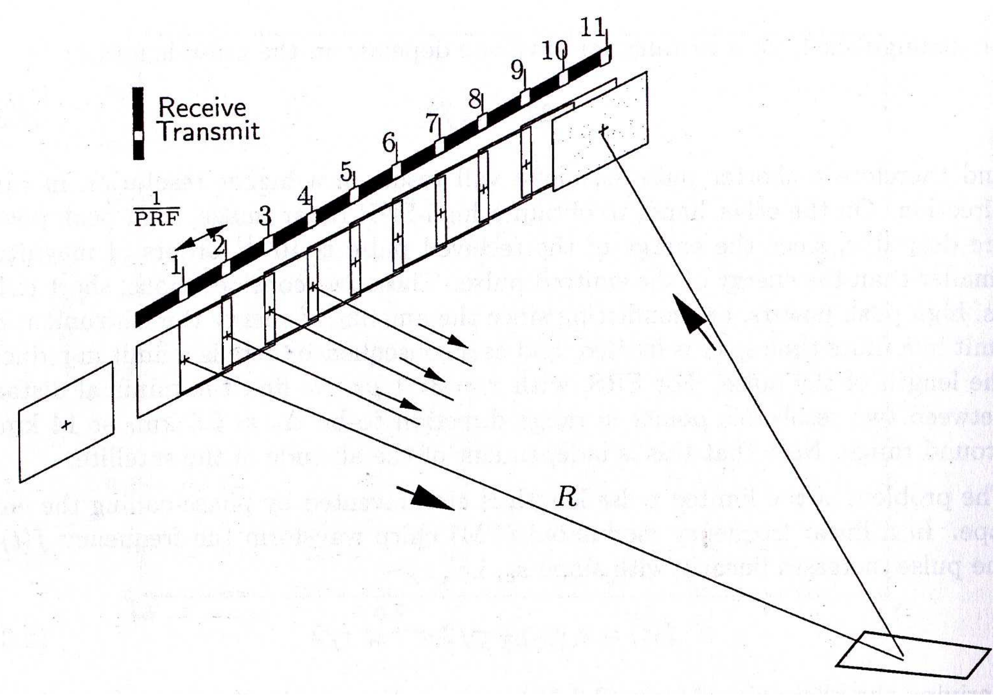

Figure 2.2. SAR pulse transmitting and receiving mode. Here, a pulse emitted at position 1 is received between position 10 and 11. The time interval between the pulse transmission is the inverse **p**ulse **r**epetition **f**requency (**PRF**) [*Hanssen*, 2001].

2.2 Interferometry Synthetic Aperture Radar

A single SAR image contains the information of *phase* and *amplitude* (Figure 2.3). By comparing the phase of two different images with different position (two antennas mounted on the same spacecraft received at the same time) or different time (one antenna received at different time), which can acquire the Z-direction representing the height of surface target. After coregistering and calculating the different phase of received echoes, the interferogram could be reproduced (Figure 2.4).

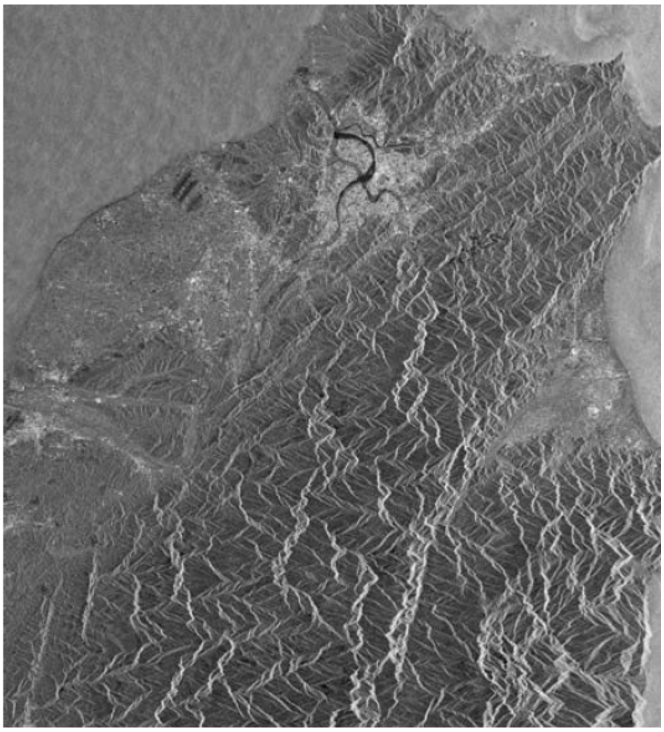

Figure 2.3. Amplitude image of ERS SAR in Northern Taiwan represents by gray color. The areas with brighter signals mean the stronger reflective signals.

This technique is called **In**terferometric **S**ynthetic **A**perture **R**adar (**InSAR**). InSAR technique was developed after the Second World War and was first applied in earth-based observations of Venus to separate ambiguous echoes from the northern and southern hemispheres [*Rogers and Ingalls*, 1969]. Subsequently, the elevation data of the Moon [*Zisk*, 1972] and the Venus [*Rumsey et al.*, 1974] were acquired by InSAR. Not until the late 1980s, scientists started using InSAR to measure the elevation of Earth [*Zebker and Goldstein*, 1986].

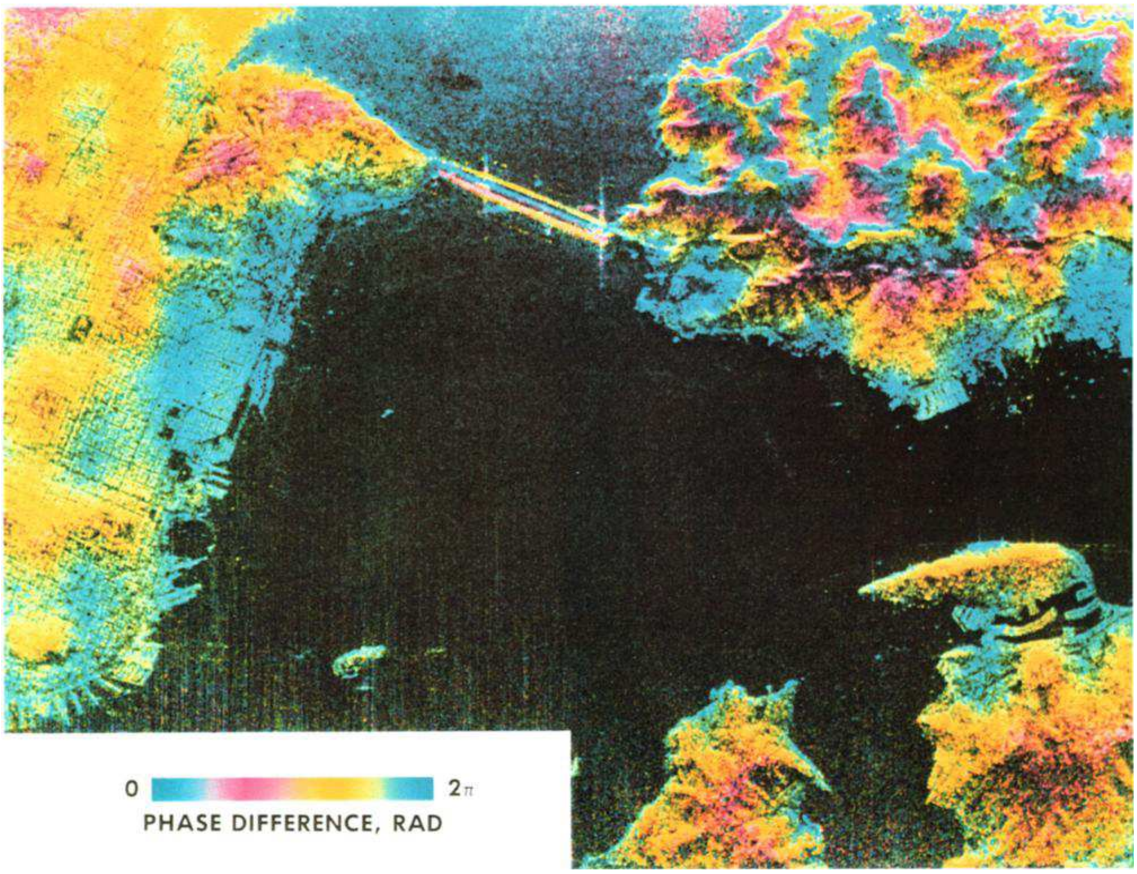

Figure 2.4. Radar interferogram of a region near San Francisco, California, representing measured amplitude (brightness of each point) and phase (color) [*Zebker and Goldstein*, 1986]

Shuttle **R**adar **T**opography **Mi**ssion (**SRTM**) was performed between 11 and 23 February 2000 by using a single-pass configuration with a fixed 60 m boom (baseline) to carry two radar antennas, which produced a precise global **D**igital **E**levation **M**odel (**DEM**) by this SAR interferometry (Figure 2.5). Furthermore, with ERS-1 and ERS-2 launched into identical orbits, but with the ground tracks separated by 24 hours during the tandem operation, the repeat-pass interferometry became feasible. Moreover, these two missions maintained in the 35 day repeat orbit keep providing abundant data to continuously monitor the crust deformation.

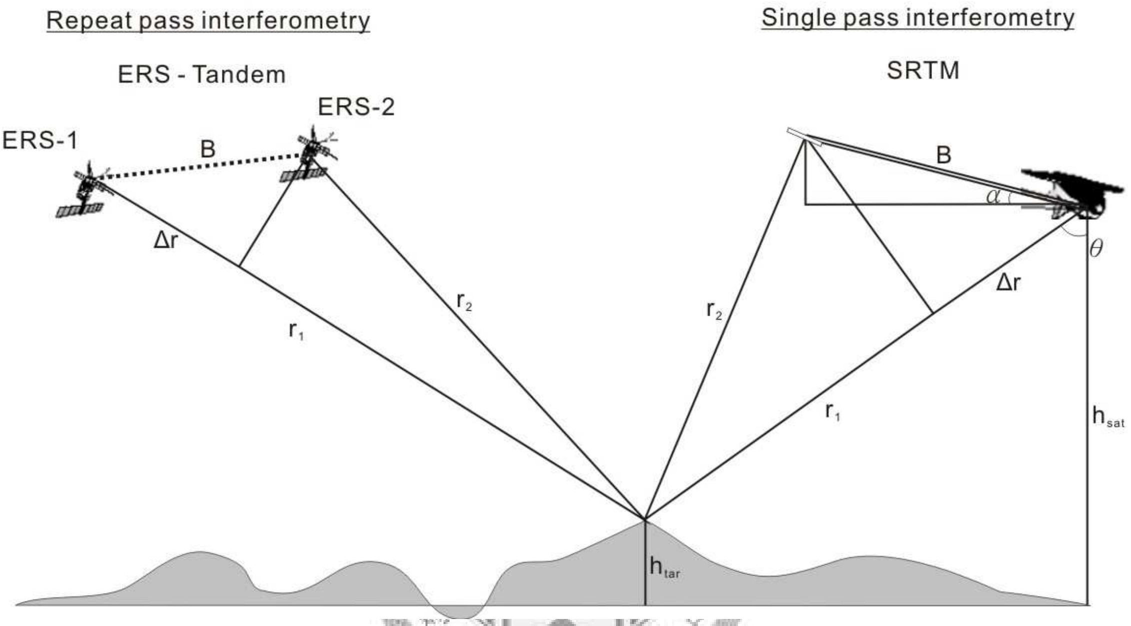

Figure 2.5. Imaging geometry for repeat- and single-pass radar interferometry [*Knöpfle et al.*, 1998].

In an interferogram, the phase was determined by the difference between the phase values of the signal in the two SAR images (master and slave). Assuming that no changes in surface properties, surface elevation, or atmospheric path delay occurred during the short time interval between the two satellite passes. The interferogram phase ϕ is directly related to the difference in path Δr according to the following formula (Figure 2.6):

$$\phi = \phi_s - \phi_m = -\frac{4\pi}{\lambda}(r_s - r_m) = -\frac{4\pi}{\lambda}\cdot\triangle r \tag{2- 2}$$

Where m is the position of “master” and s is the position of “slave”; r is the range distance.

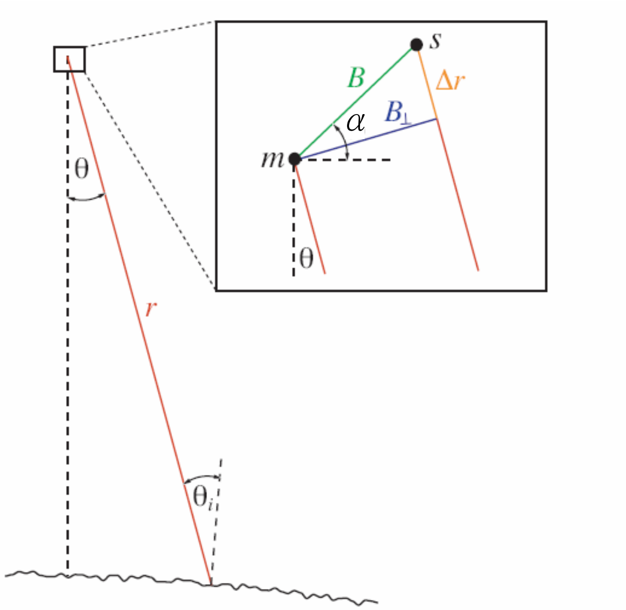

Figure 2.6. Imaging geometry for satellite radar interferometry. B is spatial baseline between two SAR acquisitions, and $B_{\perp}$ refers to the perpendicular baseline. α is the angle between the baseline vector and the horizontal, θ is the looking angle, and θ_i is the incidence angle [*Hooper*, 2006].

2.3 Differential Interferometry Synthetic Aperture Radar

Supposing a target with height h_{tar} above the reference surface moved during two passes, the phase in the interferogram contains not only topographic contributions (Figure 2.7) but also surface displacements (Figure 2.8). For the topographic contributions, the interferometric phase can be written as:

$$\delta\phi = -\frac{4\pi}{\lambda}\partial\Delta r = -\frac{4\pi}{\lambda}B\cos(\theta-\alpha)\delta\theta \approx -\frac{4\pi}{\lambda}B\cos(\theta-\alpha)\frac{h_{tar}}{r\sin\theta} \tag{2- 3}$$

In fact, the sensitivity of topography is controlled by the position of satellites. The baseline between two flights decides the value of ambiguity high [*Hanssen*, 2001], which means the elevation of a complete fringe (i.e. $-\pi$ to π) when $\delta\phi$ is equal to 2π:

$$h_a = h_{2\pi} = \left|\frac{\lambda r\sin\theta}{2B_\perp}\right| \tag{2- 4}$$

where

$$B_\perp = B\cos(\theta-\omega) \tag{2- 5}$$

From equation (2-4), the bigger baseline between two flights causes the more sensitive of topography, and increases the phase error by target elevation. It is hard to create clear fringes in interferogram when two flights with big baseline value. Therefore, baseline value is the most important parameter when picking up two SAR image for InSAR.

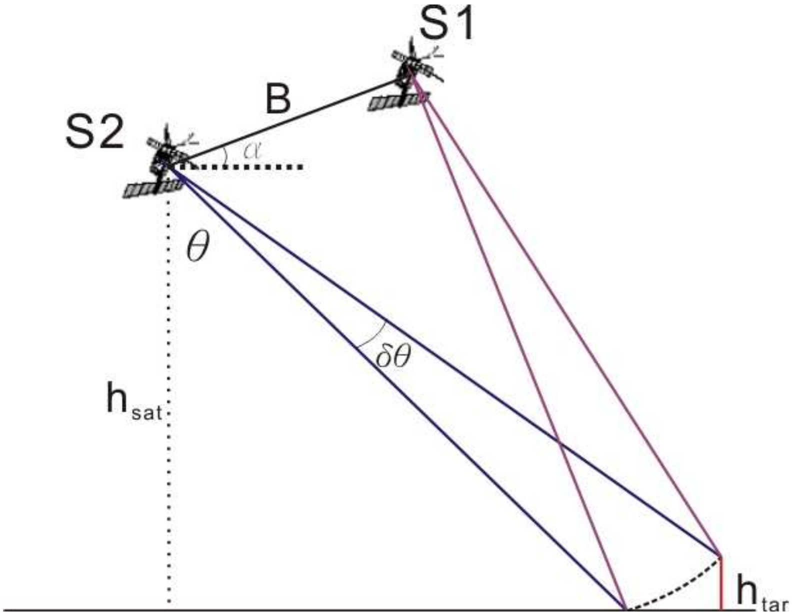

Figure 2.7. Interferometric configuration. Two SAR sensors are separated by a baseline B. The changes in looking angle $\delta\theta$ can be determined from the interferometric phase. Using the range change and the height of satellite it is possible to determine the height of point P (modified from [*Hanssen*, 2001]).

To conclude this evaluation, taking the influences of topography h_{tar} and surface displacement h_{dis} into account. The phase value $\partial\phi$ to satellite can be written as:

$$\partial\phi = -\frac{4\pi}{\lambda}\left(h_{dis} + \frac{B_{\perp}}{r_1 \sin\theta} h_{tar}\right) \tag{2- 6}$$

For the sake of simplicity, the phase delay due to differential atmosphere conditions and random noises were ignored. The interferogram phase can be defined as the difference between the measured phase ϕ and the expected phase ϑ from the geometry, so

$$\partial\phi = \phi - \vartheta \tag{2- 7}$$

where

$$\vartheta = \frac{4\pi}{\lambda} B\sin(\theta-\alpha) \qquad (2\text{- }8)$$

According to equations (2-6), (2-7) and (2-8), the measured phase at target would be:

$$\phi = \frac{4\pi}{\lambda}\left[B\sin(\theta-\alpha) - h_{dis} - \frac{B_{\perp}}{R_1\sin(\theta-\alpha)} h_{tar} \right] \qquad (2\text{- }9)$$

Therefore, the displacement along the **L**ine **o**f **S**ight (**LOS**) direction by removing the affection of topography by using two interferograms with different time interval could be got. This technique called **D**ifferential **InSAR** (**DInSAR**) has been proved its great usages with centimeter precision in applying on measuring coseismic deformation [e.g., *Massonnet et al.*, 1993], glacier and ice motion [e.g., *Goldstein et al.*, 1993], and volcanic eruption [e.g., *Amelung et al.*, 2000].

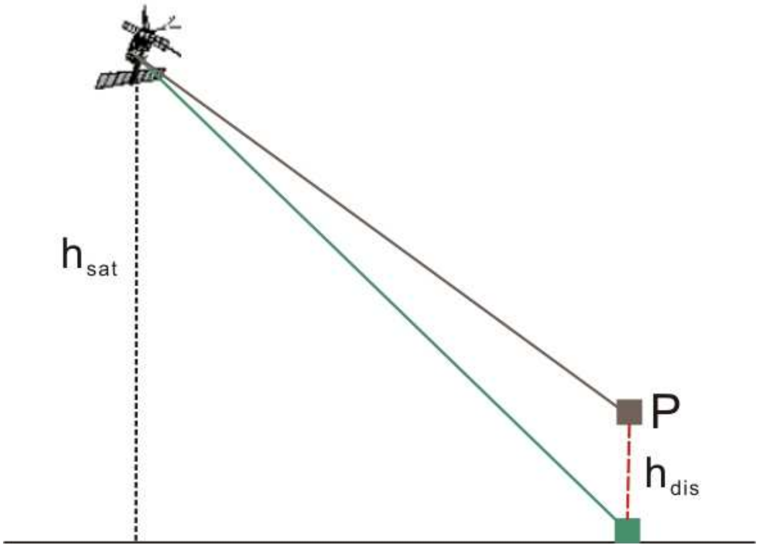

Figure 2.8. Imaging geometry for differential interferometry. Using interferograms to differentiate the DEM or that from tandem pair interferograms, the target P with a displacement h_{dis} during two passes can be determined.

DInSAR is based on using two interferograms with different time. The first one is called topographic pair (e.g., only with topography contribution), and the other one is called deformation pair (e.g., with topography and deformation contribution). Thus, as long as subtracting two interferograms, the interferogram only with deformation can be got. There are three ways to construct a differential interferogram:

Two-pass Differential Interferometry

The *two-pass* method [*Massonnet et al.*, 1993] uses an existed DEM that is converted to radar coordinates for the topographic pair, and chooses an interferogram interested with deformation for the deformation pair. After subtracting the simulated DEM from the interferogram, deformation information is propagated.

Three-pass Differential Interferometry

The *three-pass* method [*Zebker et al.*, 1994] uses three SAR acquisitions. First, chooses two suitable SAR images S1 and S2 to create the so-called topographic pair. This pair is assumed to have no deformation. The deformation occurs between A1 and S2' to create the deformation pair (Figure 2.9). After subtracting the topographic pair from the deformation pair, deformation information is propagated. The advantage of this method is the differential interferogram can be created even without an external DEM. Nevertheless, this method can only be applied when both the topographic pair and the deformation pair have a joint image. For some baseline limitation, it is hard to find the suitable pair.

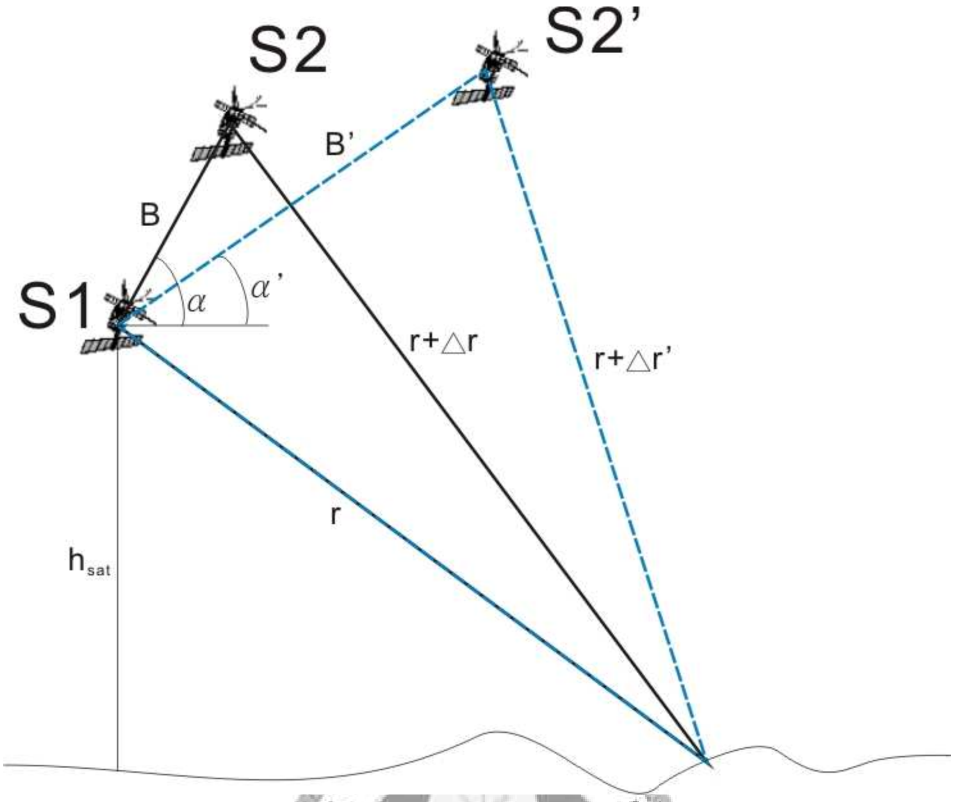

Figure 2.9. Three-pass differential interferometry configuration and radar imaging geometry. The solid lines show that radar signal paths for the first interferogram pair formed by antennas at S1 and S2. Dashed lines show signal path for second interferogram acquired over the same site with antennas located at S1 and S2' [*Zebker et al.*, 1994].

Four-pass Differential Interferometry

According to the limitation of the three-pass method, *four-pass* method uses four SAR acquisitions. In this case, the topographic pair and the deformation pair are independent, i.e. they share no common SAR acquisition. Here, there is no deformation between S1 and S2 to create the topographic pair, and the deformation occurs between S3 and S4 to create the deformation pair. After subtracting the topographic pair from the deformation pair, deformation information is propagated. In this method, the deformation occurs between S2 and S3 may cause big error of measuring the real deformation.

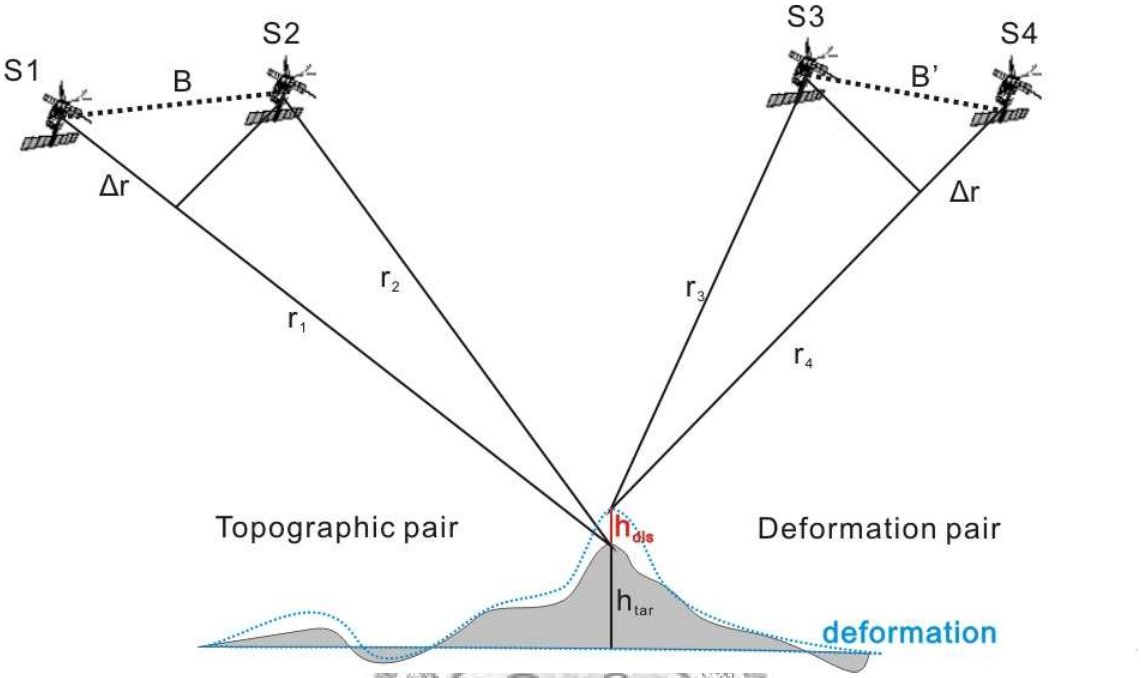

Figure 2.10. Four-pass differential interferometry configuration and radar imaging geometry.

2.4 Persistent Scatterers InSAR

2.4.1 Introduction

The **P**ersistent **S**catterers (**PS**) InSAR is an advanced technique in comparison with conventional InSAR technique, which addresses to overcome the problems of decorrelation for generating a time series of phase changes without atmospheric and DEM residual effects. This technique has been developed in the late 1990s by *A. Ferretti*, *F. Rocca*, and *C. Prati* of the Technical University of Milan (POLIMI). The first algorithm to find out the PS pixels was brought up by *Ferretti et al.* [2000; 2001], and trademarked it as the "Permanent Scatterers technique^{TM}". After that, similar processing algorithms have since been developed by *Colesanti et al.* [2003], and *Kampes* [2005]. Besides, the **SBAS** (**S**mall **Ba**seline **S**ubset) technique developed by *Berardino et al.* [2002] and **StaMPS** (**Sta**nford **M**ethod for **P**ersistent **S**catterers) developed by *Hopper et al.* [2004] are also the same idea of the PSInSAR technique with different names.

In a radar image, a signal of a resolution element was decided by the average signal of all individual scatterers within an area. Therefore, there will be either construction or destruction contribution to phase and amplitude in a resolution element developed a lot of noises in a pixel (Figure 2.11a). That is why that good conventional InSAR result can not be revealed in an area with dense vegetation. Persistent scatterers technique uses the largest contributor signals (i.e. bridges, buildings. Figure 2.11b) as the signals of a resolution element which were called persistent scatterers. In the time series, these PS points are stable enough could refer the information in the whole area. According to the conditions between neighborhood within an area are similar, using the PS point to represent the information of a resolution element can reduce the uncertain signal of back scatters and continuously get the phase changes of any PS point easily in the time series.

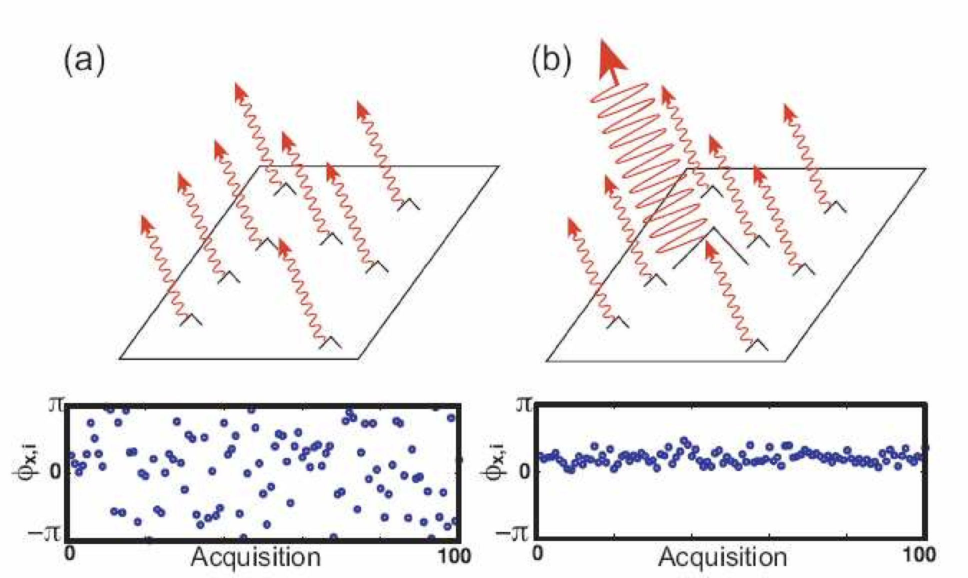

Figure 2.11. Phase simulated for (a) a distributed scatterer pixel and (b) a persistent scatterer pixel. The cartoons above represent the scatterers contributing to the phase, and the plots below show the phase values [*Hooper*, 2006].

The main steps of the PSInSAR technique can be summarized as following steps [*Ferretti et al.*, 2000, 2001; *Mora et al.*, 2003].

1) *Formation of Differential Interferograms:* Giving N+1 SAR images (same area) to form N interferograms with the same master image (detail in **2.4.2**).

2) *Selection of Stable Point Target:* Calculating the stability of each pixel to select PS candidates using analysis steps in **2.4.3**.

3) *Extraction of Linear Deformation and DEM Residual:* Using the information of temporal baseline and perpendicular spatial baseline to generate a deformation

model of the study area. Then, the linear deformation and DEM residual over each PS pixel is extracted in comparison with generated models and the real interferogram patterns (detail in **2.4.4**).

4) *Extraction of Nonlinear Deformation and Atmospheric Artifacts:* Due to different phase characters in atmosphere and nonlinear motion, the spatial and temporal filters are used to separate different phase contributions (detail in **2.4.5**).

5) *Deformation of Temporal Evolution Construction:* Finally, integrating the linear and nonlinear deformation; the deformation evolution can be obtained.

2.4.2 Choice of "Master" Image

The first step is to choose the one SAR image that minimizes the sum decorrelation, i.e., maximizes the sum correlation, of all the interferograms in the data set. The correlation depends on four terms: temporal baseline (T), perpendicular spatial baseline $\left(B_{\perp}\right)$, Doppler centroid frequency baseline (F_{DC}) and thermal noise [*Zebker and Villasenor*, 1992]:

$$\begin{aligned}\rho_{total} &= \rho_{temporal} \cdot \rho_{spatial} \cdot \rho_{doppler} \cdot \rho_{thermal} \\ &\approx \left[1 - f(\frac{T}{T^{c}})\right] \bullet \left[1 - f(\frac{B_{\perp}}{B^{c}{}_{\perp}})\right] \bullet \left[1 - f(\frac{F_{DC}}{F_{DC}^{c}})\right] \bullet \rho_{thermal}\end{aligned} \tag{2- 10}$$

where ρ denotes correlation and superscript c denotes the critical value which means the limit of producing a useable interferogram. For the ERS data only, the T = 5 yeras, $B_{\perp}^{c}$ = 1100 meters, F_{DC}^{c} = 1380 Hz, and $\rho_{thermal}$ is a constant value [*Hooper*, 2006].

2.4.3 Persistent Scatterers Identification

In the processes of PSInSAR, the algorithm is established on PS points selected. Thus, the selections of PS points are quite important. There are two common methods of selecting PS points, one based on pixel *amplitude stability* and the other on *spatial coherence*.

The ***Amplitude Dispersion Index*** (D_A) is defined by *Ferretti et al.* [2001] as:

$$D_A \equiv \frac{\sigma_A}{\mu_A} \tag{2- 11}$$

where σ_A and μ_A are respectively the standard deviation and mean of a series of amplitude values in each pixel. First, providing a complex reflectivity g and a complex circular Gaussian noise n with real (n_R) and imaginary components (n_I). Because the distribution of the amplitude value A is given by the Rice distribution:

$$f_A(a) = \frac{a}{\sigma_n^2} I_0\left(\frac{ag}{\sigma_n^2}\right) e^{-\left(a^2+g^2\right)/2\sigma_n^2} \qquad a > 0 \tag{2- 12}$$

where I_0 is the modified Bessel function. For the high **S**ignal to **N**oise **R**atio (**SNR**, $g/\sigma_n > 4$), f_A approaches a Guass distribution. Provided that $\sigma_n \ll |g|$, then:

$$\sigma_A \simeq \sigma_{nR} = \sigma_{nI} \tag{2- 13}$$

since the modulus is primarily affected by the noise component parallel to $g\left(n_R\right)$. The phase distribution (σ_v) can then be estimated starting from the amplitude dispersion:

$$\sigma_v \simeq \frac{\sigma_{nI}}{g} \simeq \frac{\sigma_A}{\mu_A} = D_A \tag{2- 14}$$

The D_A is then a measure of phase stability, at least for high SNR values (low D_A). Typically, D_A < 0.25 is usually chosen as the threshold [*Ferretti et al.*, 2001].

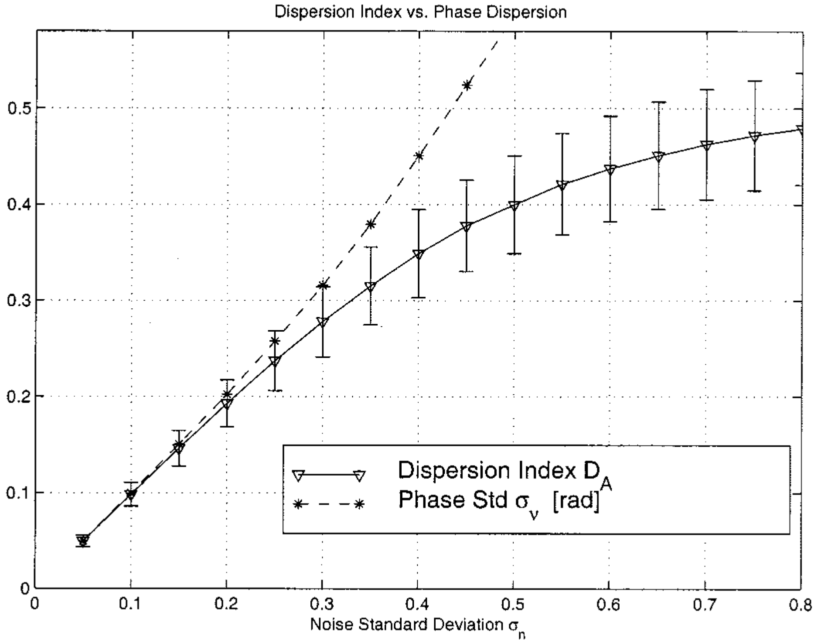

Figure 2.12. Numerical simulation results for D_A and phase stability. Small values of D_A are good estimates of the phase dispersion [*Ferretti et al.*, 2001].

For ***spatial coherence*** method, following the idea of PSInSAR, the correlation threshold would be the easiest approach. First, two SAR images $I_1(x,y)$ and $I_2(x,y)$ can be written as:

$$\begin{aligned} I_1(x,y) &= A_1(x,y)e^{j\phi_1(x,y)} \\ I_2(x,y) &= A_2(x,y)e^{j\phi_2(x,y)} \end{aligned} \tag{2- 15}$$

$A_1(x,y)$, $A_2(x,y)$ are the amplitude values, and $\phi_1(x,y)$, $\phi_2(x,y)$ are the phase values, then the coherence can be expressed as:

$$\gamma(x,y) = \frac{\left|\sum A_1(x,y)A_2(x,y)e^{j\phi_1(x,y)-j\phi_2(x,y)}\right|}{\sqrt{\sum A_1^2(x,y)}\sqrt{\sum A_2^2(x,y)}} \tag{2- 16}$$

where $\sum$ means average within a window. As long as the pixel exhibits coherence always greater than the threshold in all data set, provide that the phase stable enough. All these pixels with this character will be selected as PS candidates. Due to the principle of coherence, the value of coherence is based on the estimation window. The larger the window dimension, the higher the estimator accuracy, but the lower the resolution. Besides, the DEM residual cause significant contribution to phase. Supposing a SAR pair with big spatial baseline, the coherence value will be low even the pixel with strong stability. Thus, the suitable values of window dimension and coherence threshold are needed to be finding out.

After picking up the PS candidates, only these pixels will be analyzed in the following steps. It is important to point out that the PS candidates which selected by the above-mentioned algorithms were the preliminary result, they are not the final PS points. In the following steps, the points with bad correlation to the real deformation will be rejected to get the real PS points.

2.4.4 Extraction of Linear Deformation

When producing a DInSAR result by two SAR images, the phase can be written as the sum of four terms:

$$\phi_{diff} = \phi_{mov} + \phi_{topo\ error} + \phi_{atm} + \phi_{noise} \tag{2- 17}$$

where

ϕ_{mov} : Phase change due to movement of the pixel in the range distance;

$\phi_{topo\ error}$: Residual topographic phase due to misfit with the DEM;

ϕ_{atm} : Phase due to different atmospheric condition between passes;

ϕ_{noise} : Noise term due to temporal and spatial decorrelation and thermal.

Here, the movement term (ϕ_{mov}) has two contributions: linear movement and nonlinear movement only correlate with velocity, and the DEM error is proportional to the perpendicular spatial baseline:

$$\phi_{mov} = \phi_{linear} + \phi_{nonlinear} = \frac{4\pi}{\lambda} \cdot v \cdot T + \phi_{nonlinear} \tag{2- 18}$$

$$\phi_{topo\ error} = \frac{4\pi}{\lambda} \cdot \frac{B_{\perp} \cdot \varepsilon}{r \cdot \sin\theta} \tag{2- 19}$$

where

λ: System wavelength (5.6 cm for ERS);
v: Constant velocity of the linear displacement;
T: Temporal baseline between two SAR acquisitions;
r: Range increment between two SAR acquisitions;
ε: DEM error;
θ: Incidence angle.

Because the phase is wrapped, the phase of individual pixel has an infinite solution. In order to calculate the best solution, the usage of Delauney triangulation is joining to connect all the discrete points for controlling each two points with each other. This kind of triangulations relates all the neighboring pixels of irregularly girded data generating non-overlapped triangles. In Figure 2.13, all the discrete points are connected to form a network to calculate the best solution.

The phase difference between two points (x_a, y_a) and (x_b, y_b) in Figure 2.13 can be expressed as:

$$\delta\phi_{diff} = \delta\phi_{\varepsilon} + \delta\phi_{mov} + \delta\phi_{atm} + \delta\phi_{noise} \tag{2- 20}$$

For the whole data set, it becomes as:

$$\begin{aligned}\delta\phi_{diff}(x_a,y_a,x_b,y_b,T_i) &= \frac{4\pi}{\lambda}\cdot T_i\cdot\left[v(x_a,y_a)-v(x_b,y_b)\right]\\ &+\frac{4\pi}{\lambda}\cdot\frac{B(T_i)}{r(T_i)\cdot\sin(\theta_i)}\cdot\left[\varepsilon(x_a,y_a)-\varepsilon(x_b,y_b)\right]\\ &+\left[\beta(x_a,y_a,T_i)-\beta(x_b,y_b,T_i)\right] \qquad (2\text{-}21)\\ &+\left[a(x_a,y_a,T_i)-a(x_b,y_b,T_i)\right]\\ &+\left[n(x_a,y_a,T_i)-n(x_b,y_b,T_i)\right]\end{aligned}$$

where

x, y:	Position coordinates of the pixel;
T_i:	Temporal baseline of the ith interferogram;
β:	Nonlinear component of velocity;
a:	Atmospheric artifacts;
n:	Noise.

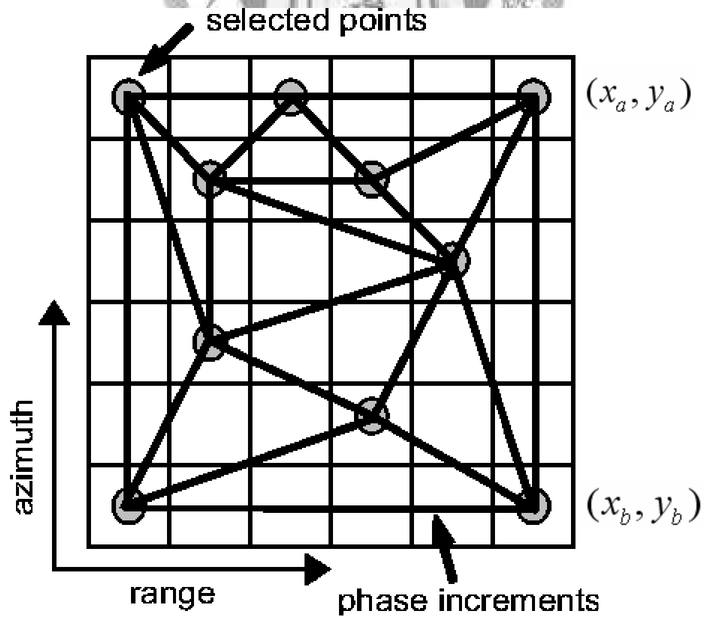

Figure 2.13. Example of Delauney triangulation. (x, y) are the position coordinates of PS point a and b [*Mora et al.*, 2003].

Here, a limitation that atmospheric perturbations are the same in the neighboring pixels in a small area was added. The maximum distance allowed to connect two separate pixels is limited to approximately 1 kilometer. For this reason, first reject the connection with distance longer than the limitation distance.

Using the information of temporal and spatial baseline that already known and assuming a velocity and DEM error range in (2-18) and (2-19), a model can be assumed as:

$$\begin{aligned}\delta\phi_{model}(x_a, y_a, x_b, y_b, T_i) &= \frac{4\pi}{\lambda}\cdot T_i \cdot \left[v_{model}(x_a, y_a) - v_{model}(x_b, y_b)\right] \\ &\quad + \frac{4\pi}{\lambda}\cdot\frac{B(T_i)}{r(T_i)\cdot\sin(\theta_i)}\cdot\left[\varepsilon_{model}(x_a, y_a) - \varepsilon_{model}(x_b, y_b)\right] \end{aligned} \tag{2- 22}$$

Then, Using the following model coherence function to perform maximization γ_{model}:

$$\gamma_{model} = \frac{1}{N}\left|\sum_{i=0}^{N}\exp\left[j\cdot(\delta\phi_{diff}(T_i) - \delta\phi_{model}(T_i))\right]\right| \tag{2- 23}$$

where N is the number of interferograms. This function is equal to 1 when the adjustment to data is perfect, and zero in case of total decorrelation. Once the maximization process has been done for each connection, the result is the following set of velocity and DEM error:

$$\begin{aligned}\Delta v_{estimated}(x_a, y_a, x_b, y_b) &= \left[v_{model}(x_a, y_a) - v_{model}(x_b, y_b)\right]_{maximize\,\gamma} \\ \Delta\varepsilon_{estimated}(x_a, y_a, x_b, y_b) &= \left[\varepsilon_{model}(x_a, y_a) - \varepsilon_{model}(x_b, y_b)\right]_{maximize\,\gamma}\end{aligned} \tag{2- 24}$$

At this point, a new quality test is performed and all the connections with coherence below a threshold are rejected. Good results have been obtained with coherence thresholds larger than 0.7 [*Mora et al.*, 2003]. As a consequence of the quality test, some pixels left without connection will be eliminated. Besides, the velocity and DEM error in each connection can be written as:

$$\begin{aligned}\Delta v_{estimated} &= v\left(x_{a,}y_{a}\right)-v\left(x_{b,}y_{b}\right)\\ \Delta \varepsilon_{estimated} &= \varepsilon\left(x_{a,}y_{a}\right)-\varepsilon\left(x_{b,}y_{b}\right)\end{aligned} \tag{2- 25}$$

Then, A least mean square process is necessary to obtain absolute values for each point. Figure 2.14 shows a detailed layout of linear deformation and DEM error extraction.

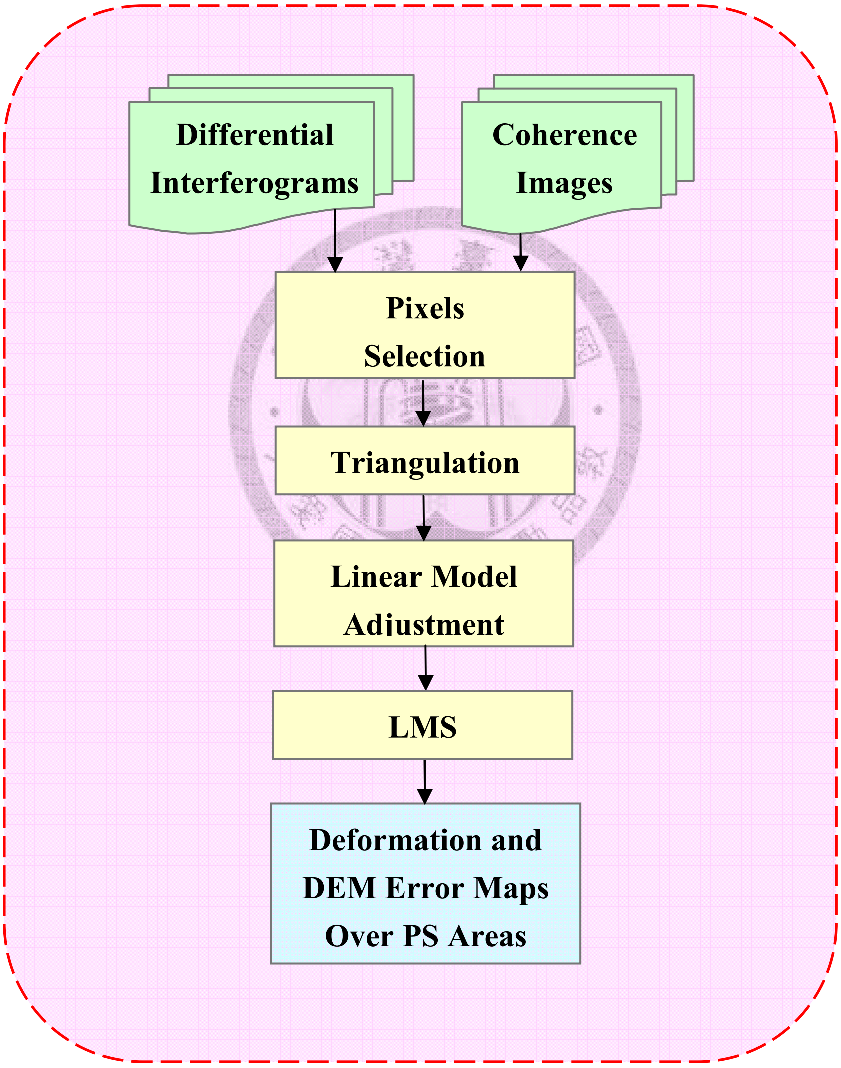

Figure 2.14. Layout of linear deformation and DEM error extraction.

2.4.5 Extraction of Nonlinear Deformation and Atmospheric Artifacts

After finishing the linear velocity and DEM error, it is possible to obtain the nonlinear component to complete the whole deformation in interested area. At first, the residual phases obtained by subtracting the previously estimated linear deformation and DEM error from the original differential interferometric phases. Then, the phase residual can be expressed as:

$$\begin{aligned}\delta\phi_{residual}(x,y,T_i) &= \delta\phi_{nonlinear}(x,y,T_i)\\ &+\delta\phi_{atmos}(x,y,T_i)+\delta\phi_{noise}(x,y,T_i)\end{aligned} \tag{2- 26}$$

where two important terms (the nonlinear contribution $\delta\phi_{nonlinear}$ and the atmospheric artifacts contribution $\delta\phi_{atmos}$) can be isolated taking advantage of their different frequency characteristics in space and time [*Ferretti et al.*, 2000]. The mean value of the residual phases ($\overline{\delta\phi}_{residual}$) is an estimation of the atmospheric phase contribution of the master image in each PS point (common to all the differential interferograms, said correlate in temporal). Beside, the nonlinear motion contribution was also considered to reveal a high correlation in temporal. Thus, the estimation of the nonlinear motion contribution should be considered as the low pass component of this function:

$$\delta\phi_{nonlinear}=\left[\delta\phi_{residual}(T_i)-\overline{\delta\phi}_{residual}\right]_{LP\_Time} \tag{2- 27}$$

Furthermore, atmospheric retardation is spatial correlated over distance of a specified length scale, said 1 kilometer. Atmospheric perturbations are considered as a low spatial frequency signal in each interferogram, and a random phase in time for each pixel (for slave images). Thus, the atmospheric estimation is then carried out by smoothing spatially the high pass filtered residual phase time series:

$$\delta\phi_{atmos}=\left[\left[\delta\phi_{residual}(T_i)\right]_{HP\_Time}\right]_{LP\_Space}+\left[\overline{\delta\phi}_{residual}\right]_{LP\_Space} \tag{2- 28}$$

where the first term is an estimation of the atmospheric phase contribution superimposed on the single SAR image acquired at time T_i. The filtered atmospheric component relative to the master acquisition is then added back to get the atmospheric artifacts of each differential interferogram. Figure 2.15 shows a detailed layout of nonlinear deformation and atmospheric artifacts extraction.

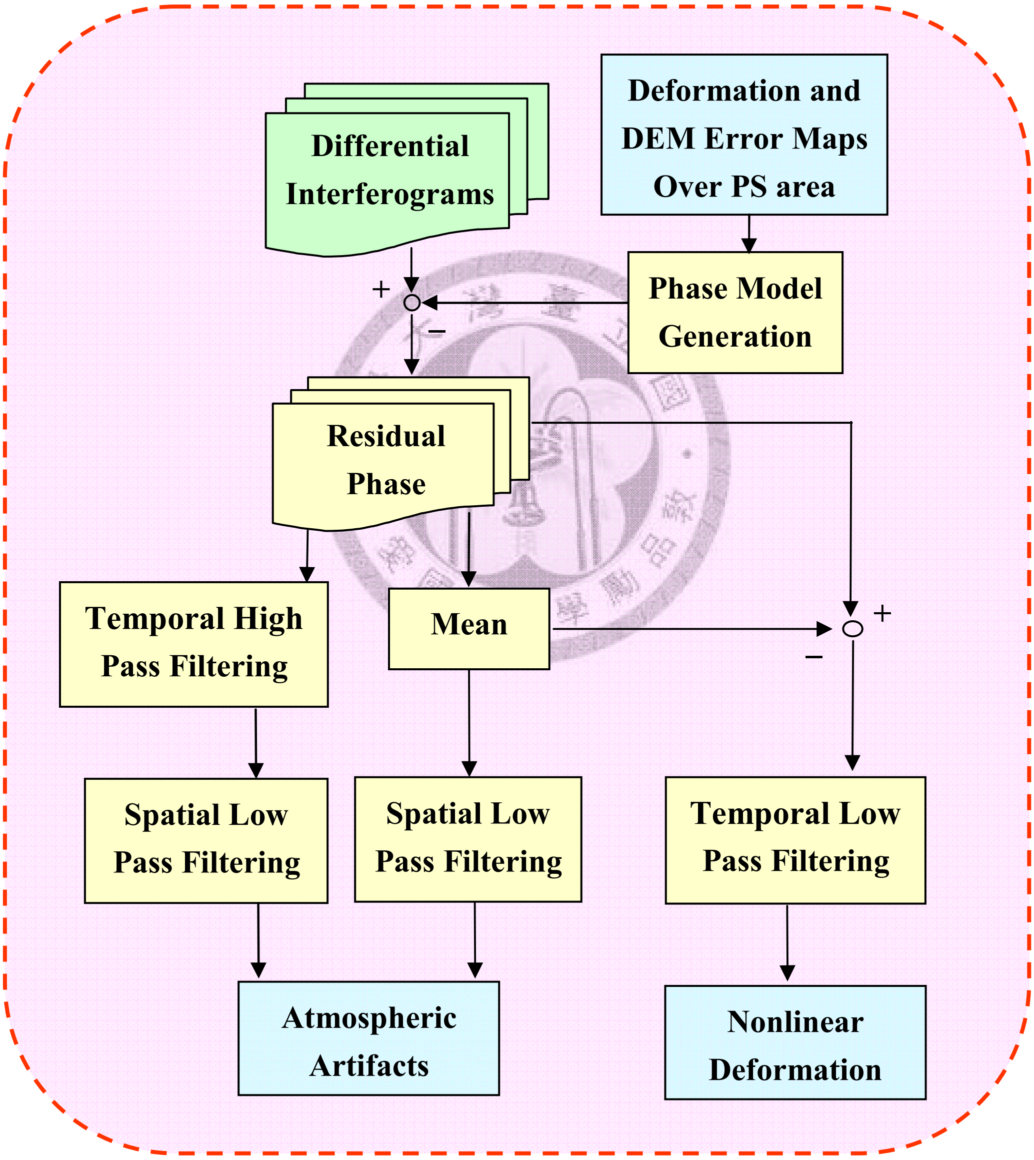

Figure 2.15. Layout of nonlinear deformation and atmospheric artifacts extraction.

Chapter 3

Active Deformation in Southwestern Taiwan

In this chapter, I present an application of PSInSAR technique based on SAR images deduced from 1996-1999 time periods in and around Tainan Tableland of southwestern Taiwan, which is an active fault-related folding near the deformation front. First, I want to characterize the deformation pattern due to the evolution of this active structure. Second, the relationship between nonlinear behavior demonstrated by PSInSAR results and precipitation, groundwater level, and microseismicities will be investigated.

Here, I adopt the idea from *Ferretti et al.* [2000; 2001] and *Mora et al.* [2003] to develop the procedures of PSInSAR processing by Matlab for this study. In order to ensure the reliability of our programs, I choose the Tainan area as a test site where it had been well studied by using conventional DInSAR technique [*Fruneau et al.*, 2001; *Huang et al.*, 2006] and the geodetic measurements [*Rau et al.*, 2004]. Thus, the Tainan area is expected to be an ideal urbanized site to validate the PSInSAR results.

3.1 Introduction

Taiwan is located in an active collision boundary where the EP has collided with the PSP since late Miocene (Figure 3.1). Because of the oblique convergence between the two plates, strong crustal deformation is demonstrated by frequent seismicities and active structures [e.g. *Hu et al.*, 2001]. The Tainan Plain of southwestern Taiwan is incorporated into active deformation by a regional fold-and-thrust belt associated with the convergent plate margin of the Luzon Arc and the Eurasian continent.

The Tainan city surrounded Tainan Tableland, which is considered to be located close to the deformation front in southwestern Taiwan [*Sun*, 1964]. Previous DInSAR research from *Fruneau et al.* [2000] revealed a ground motion of 28 mm along the radar line of sight towards the satellite during the period 1996 to 1998. Also, *Ho* [2006] showed a decreasing SRD from the southern Tainan Tableland (12 mm/yr) to the northern Tainan Tableland (10 mm/yr). Furthermore, *Huang* [2006] predicted an average SRD rate of 12.5 mm/yr during the period 1996 to 2001 on the Tainan Tableland which is quite consistent with the precise leveling data measured by *Rau et al.* [2004] (Figure 3.2). The precise leveling data reveals maximum uplift rates on the Tainan Tableland of about 12 mm/yr relative to TN01 (Figure 3.3). However, a borehole data near TN01 shows a long term subsidence rate is about 6.6 mm/yr [*Zhou*, 2007]. Thus, the uplift rate predicted by precise leveling by using TN01 as a reference station should be overestimated. In addition, *Chen and Lin.* [2000] demonstrated that the long term uplift rate on the Tainan Tableland is about 5 mm/yr and revealed an eastward increasing in uplift rates based on radiocarbon ages and relative sea-level curves of late Holocene. These entire results figure out the Tainan Tableland is a significant growing structure.

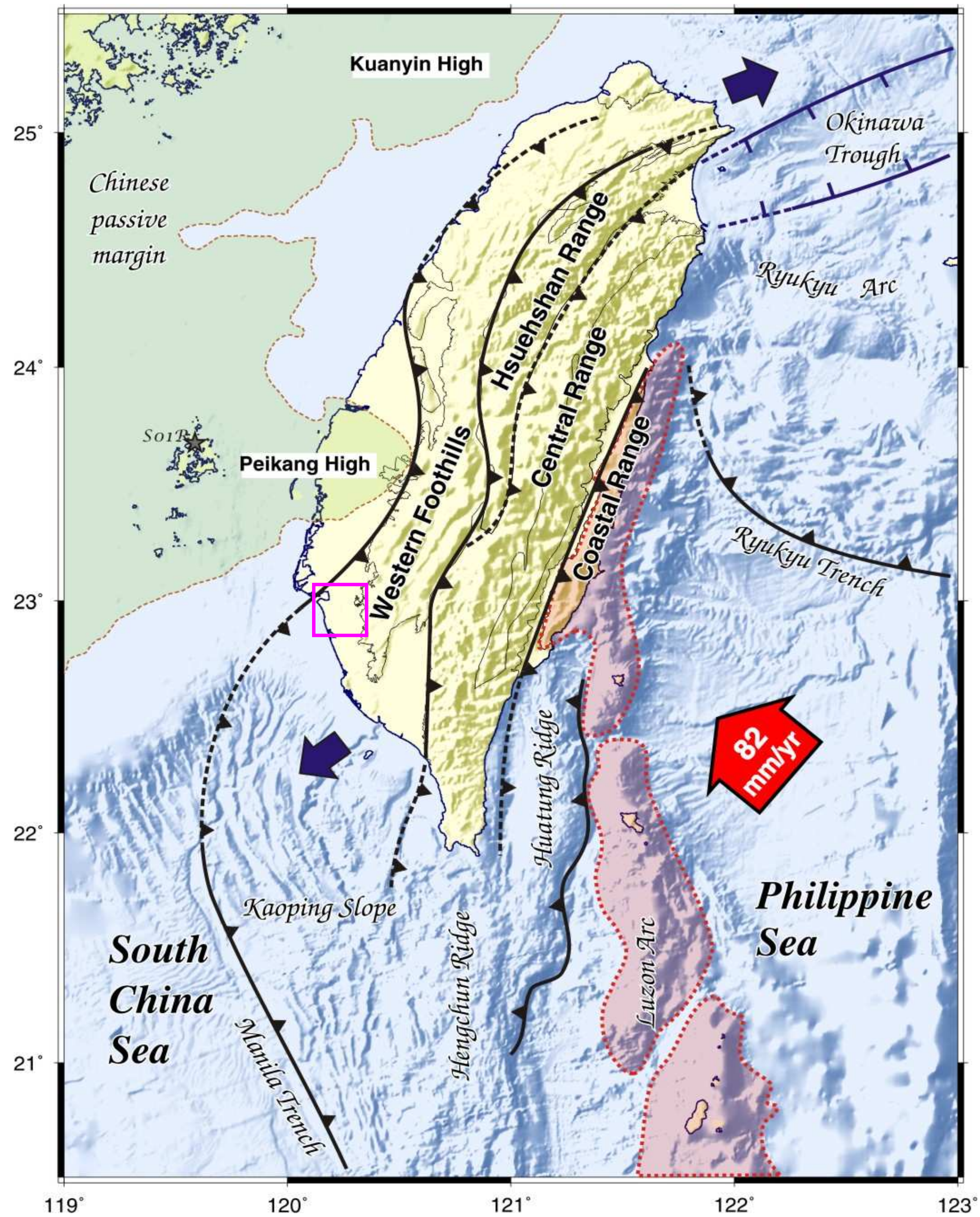

Figure 3.1. Geodynamic framework and structural map of Taiwan [after *Ching et al.*, 2007]. Red arrow indicates the relative velocity across Taiwan Island with 82 mm/yr along N309 ° E from the PSP [*Yu et al.*, 1997]. Pink rectangle indicates the study area, the Tainan tableland.

According to these abundant geologic and geodetic observations in Tainan area, the Tainan Tableland is the most suitable study area to validate our PSInSAR technique. The goal of this case study is focus on PSInSAR technique to obtain the deformationpattern in the Tainan area in comparsion with geodetic measurements to better understand the correlation between the deformation patterns and geological structure in Tainan area.

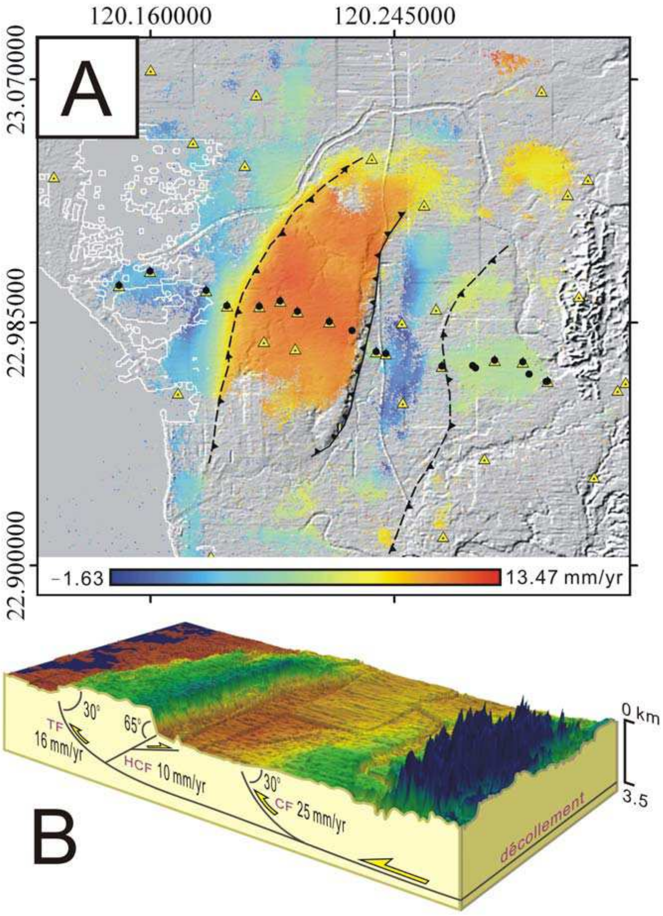

Figure 3.2. Active deformation in Tainan Tableland revealed by D-InSAR and dislocation model. (A) SRD of interferogram after phase unwrapping on shaded topography, which can indicate the deformation pattern of a pup-up structure. (B) Inferred structural model as a decollément-related pop-up structure [*Huang et al.*, 2006].

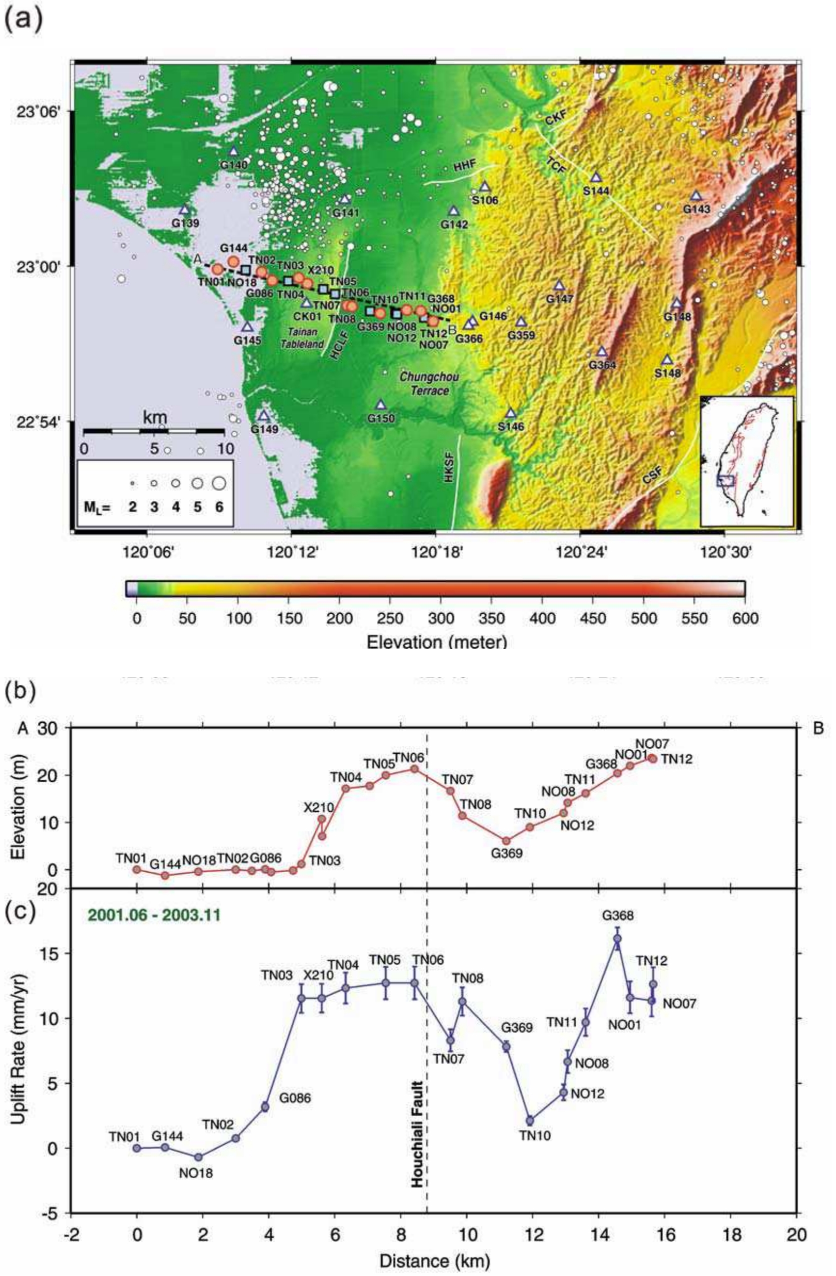

Figure 3.3. (a) Southwestern Taiwan geological structural setting and location of GPS (triangles and circles) and leveling stations (rectangle and circles). (b) Elevation measurement of precise leveling (relative to TN01) project to AB profile. (c) Uplift rate measurement of precise leveling relative to TN01 [*Rau et al.*, 2004].

3.2 Tectonic Setting and Geological Background

The investigating area of southwestern Taiwan represents the Plio-Pleistocene foreland basin developed by lithospheric flexure due to the tectonic loading of the Central Range [*Lin and Watts*, 2002]. Under the influence of convergence of PSP and EP, the fold-and-thrust belt propagates westward into the foreland basin. The westernmost surface exposures of the fold-and-thrust belt reach near the region of Tainan plain [*Sun et al.*, 1998]. From the west to the east, the Tainan Plain can be divided into three parallel geomorphic units with different altitudes: the Tainan Tableland, the Tawan Lowland and the Chungchou terrace (Figure 3.3a).

Tainan Tableland

The Tainan Tableland is a structural high with active folding, which lies about 30 m above sea-level. The geomorphic feature demonstrates a north-southward elongated convex shape with a 12.5 km long and 4 km wide along a N020°E trending axis. Its topography shows an east-west asymmetry with dipping gently westward into the Taiwan Strait, whereas the eastern edge is a scarp bordering the Tawan Lowland. *Sun* [1964] interpreted this scrape as a surface expression of the Houchiali fault in the eastern edge of the Tainan Tableland using the aerial photographs. Later on, *Hsieh* [1972] interpreted the Tainan Tableland as an anticline due to diapiric folding based on gravity data. Based on the shallow seismic profile, the Houchiali fault had been interpreted as a normal fault located on the eastern edge of Tainan Tableland [*Kuo et al.*, 1998]. On the other hand, several authors [*Deffontaines et al.*, 1997; *Lacombe et al.*, 1999; *Mouthereau et al.*, 2002] proposed a pop-up model related to a shallow decollement underling the Tainan Anticline. In addition, *Fruneau et al.* [2001] proposed three schematic models (Figure 3.4) on the Tainan Tableland based on the deformation pattern revealed by DInSAR results. Furthermore, *Huang et al.* [2004] suggested that the Tainan Anticline is probably associated with back-trusting mechanism due to lack of clear offset between reflected horizons.

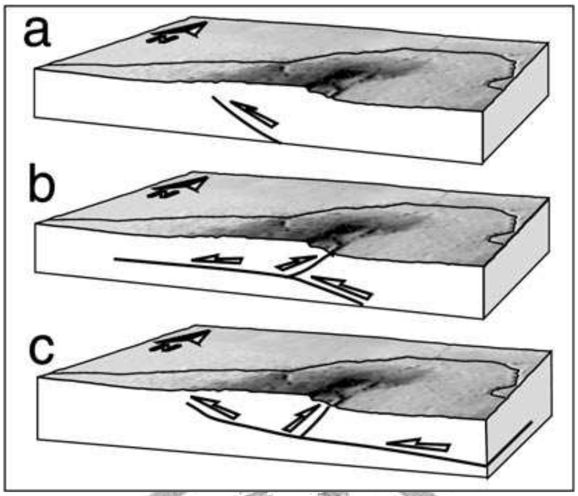

Figure 3.4. Three schematic structural models of the Tainan Tableland. (a) Blind thrust model; (b) Fish-tail model; (c) Pop-up model [*Fruneau et al.*, 2001].

Houchiali Fault

The trend of the Houchiali fault is in N-S direction with an 11 km long on the eastern margin of Tainan Tableland. It turns to northwestward direction on the north edge and southwestward direction on the south edge to be an S-shape. *Lin* [1957; 1963] suggested that the Houchiali fault is normal fault with high dip angle along the western Tainan Tableland. However, *Chang* [2005] prove the Houchiali fault is a high angle reverse fault by exploration seismology data.

Tawan Lowland

The Tawan Lowland has an average altitude of about 6 m above sea-level. It is located between the Tainan Tableland and the Chungchou Terrace and its trend is in

NNE-SSW direction. Its surface elevation increases eastward and gradually merges with the Chungchou Terrace. *Chen* [1993] considered the subsidence on the Tawan Lowland is caused by the activity of the Houchiali fault.

Southwestern Taiwan has been the foreland basin since the Pliocene period [*Teng*, 1987; *Lee et al.*, 1999; *Lin*, 2001]. Based on the seismic section and typical subsurface geological column from borehole [*Huang et al.,* 2004], the stratigraphy of Tainan area can be divided into five formations (Figure 3.4, see Kaohsiung and Chishan area):

Tainan Formation (Terrace Deposit)

The Tainan Formation is deposited during Holocene [*Lin*, 1969; *Hashimoto*, 1972] and has a thickness of 10 to 100 meters. It consists of unconsolidicated sand and mudstone characterized by sedimentary structures representing coastal marine environments [*Wu*, 1990, 1992; *Chen*, 1993].

Liushuang Formation

The Liushuang Formation is the youngest unit of the Pleistocene and has a thickness of 500 to 830 meters. It shows the inter-layer of gray mudstone and shale with thick-bedded sandstone on the upper and lower part with abundant fossils [*Ho*, 1975].

Erhchungchi Formation

The Erhchungchi Formation has a thickness of 1040 meters, which shows the inter-layer of shale and sandstone with abundant marine deposit [*Ho*, 1975].

Upper Gutingkeng Formation

The Upper Gutingkeng Formation has a thickness of 540 to 1000 meters, which consists of gray sandy siltstone and sandy mudstone intercalated with lenticular greywacke and subgraywacke with abundant mollusca.

Lower Gutingkeng Formation

The Lower Gutingkeng Formation has a thickness more than 4000 meters, which consists of gray siltstone or mudstone intercalated with thin-bedded sandstone.

The typical stratigraphic columns are shown in Figure 3.5 are occupied by mudstone intercrated with fine or very fine grain sandstones of the Plio-Pleistocene.

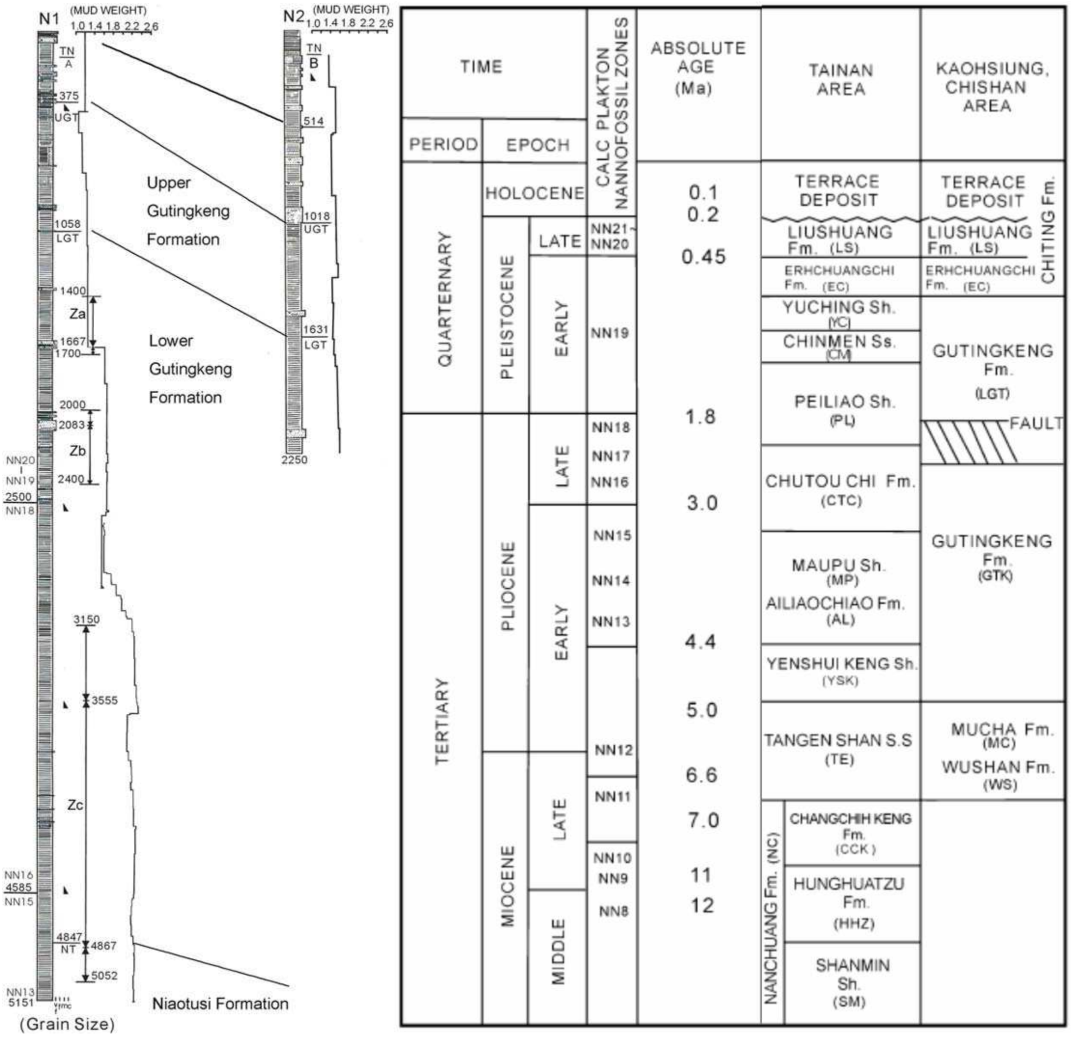

Figure 3.5. Left: Typical subsurface geological column on the Tainan Tableland. Right: The stratigraphy in Tainan area [*Huang et al.*, 2004].

3.3 Analyses and Results

3.3.1 Description of data analyses

The data set used is listed in Table 3.1, which includes 33 C-band radar images collected by the ERS-1 and ERS-2 satellites of the ESA in descending orbits (track: 232; frame: 3141) between January 1996 and August 1999 over the study area. An area of about 12 × 12 km^2 was selected from the images, corresponding to the urban area of Tainan. Meanwhile the 'Precise Orbit' data are downloaded from the DEOS.

For the conventional DInSAR processes, I use the software DIAPASON V4 from the Altamira Information, which is used for producing SAR images from raw data to differential InSAR by two-pass differential interferometry. The external DEM used to cancel the topographic component of the interferometric phase is the free distribution DEM from NASA's SRTM mission generated by InSAR technique; with this DEM which base on the same principle can effectively reduce error when generating DInSAR. This DEM is an approximately 90 × 90 m (3 s arc) global DEM with a standard deviation of 10 m in height. In order to increase resolution of geocoded interferograms, the original DEM was interpolated into a finer one (45 × 45 m).

For the PSInSAR processes, I use MATLAB 7.1 language for processing programs compiler. From step 1 to step 3 mentioned in 2.4.1 based on the journal paper by *Mora et al.* [2003], and step 4 based on the journal paper by *Ferretti et al.* [2000; 2001].

Table 3.1. Descending orbit data processed for the Tainan area (track: 232, frame: 3141). Perpendicular baseline is relative to 19960131 (orbit: 23767).

	Orbit	Date	Sensor	$B_{\perp}$ (m)	F_{DC} (Hz)
1	23767	1996/01/31	ERS-1	0	25.68
2	4094	1996/02/01	ERS-2	145	-10.31
3	24268	1996/03/06	ERS-1	248	26.99
4	5097	1996/04/11	ERS-2	44	-14.18
5	25271	1996/05/15	ERS-1	152	32.03
6	6099	1996/06/20	ERS-2	-498	-13.15
7	7100	1996/08/29	ERS-2	-828	-21.16
8	7602	1996/10/03	ERS-2	-520	-18.31
9	8604	1996/12/12	ERS-2	-542	-14.24
10	9104	1997/01/16	ERS-2	-182	-18.53
11	9606	1997/02/20	ERS-2	-376	-8.23
12	10106	1997/03/27	ERS-2	-111	-7.61
13	10607	1997/05/01	ERS-2	-573	-15.88
14	11108	1997/06/05	ERS-2	-433	-11.31
15	11609	1997/07/10	ERS-2	-398	-10.84
16	12111	1997/08/14	ERS-2	-141	-18.73
17	12611	1997/09/18	ERS-2	-662	-17.14
18	13613	1997/11/27	ERS-2	-23	-21.07
19	14114	1998/01/01	ERS-2	44	-19.51
20	14616	1998/02/05	ERS-2	-470	-32.12
21	15117	1998/03/12	ERS-2	-515	-16.82
22	16118	1998/05/21	ERS-2	-204	0.34
23	16620	1998/06/25	ERS-2	-1258	-1.37
24	17121	1998/07/30	ERS-2	-89	-4.96
25	17622	1998/09/03	ERS-2	58	-3.79
26	18623	1998/11/12	ERS-2	117	-10.10
27	19125	1998/12/17	ERS-2	-690	-15.55
28	19625	1999/01/21	ERS-2	105	-12.89
29	20627	1999/04/01	ERS-2	-614	-10.88
30	21128	1999/05/06	ERS-2	199	-5.42
31	21630	1999/06/10	ERS-2	-208	-6.10
32	22130	1999/07/15	ERS-2	-53	-6.22
33	22631	1999/08/19	ERS-2	978	-10.21

3.3.2 Results of surface deformation by conventional DInAR

I select the master image (1997/07/10) using equation 2-10, and then generate 32 interferograms by 33 SAR images (Figure 3.6). The 32 original results show not only the movement along the LOS, but also the contributions of topographic residuals, atmospheric artefacts and noises. Especially the perpendicular spatial baseline is greater than 400 m, there are few clear fringes can be generated. Also, the greater temporal baseline, the more perturbations can be seen in the interferograms.

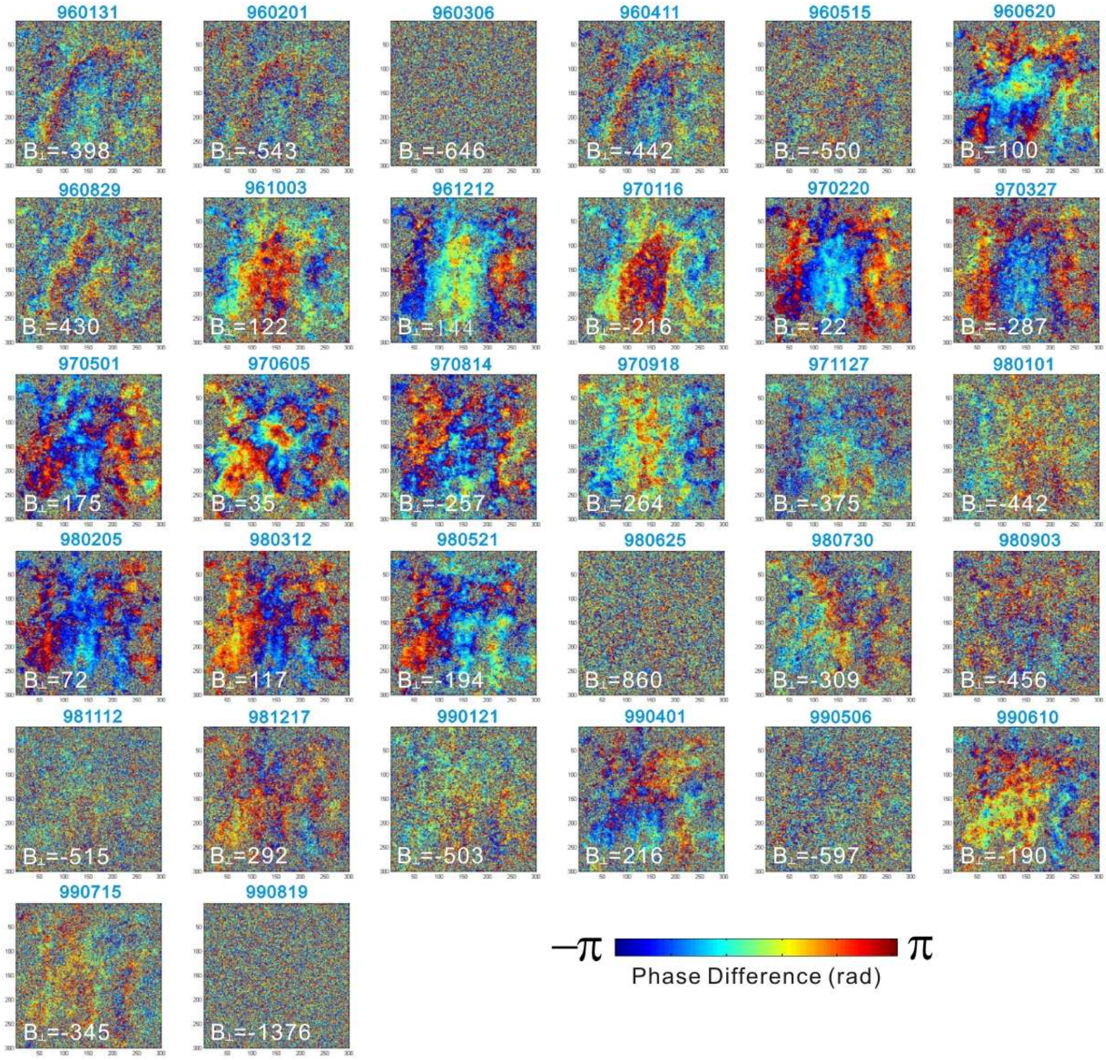

Figure 3.6. Totally 32 interferograms with phase wrapped are reproduced by 33 SAR images from 1996/01/31 to 1999/08/19. The master image is acquired on 10 July 1997.

3.3.3 Results of surface deformation by PSInSAR

The first step is the selection of PS candidates, which presents coherence stability in time. Due to the limitation of technique for separating the slave amplitude images from master one, I used spatial coherence method to select PS candidates. In our study, pixels with a stable coherence value higher than 0.3 in all data set have been selected. There are 1649 pixels have been chosen to connect using the Delaunay triangulation (Figure 3.7).

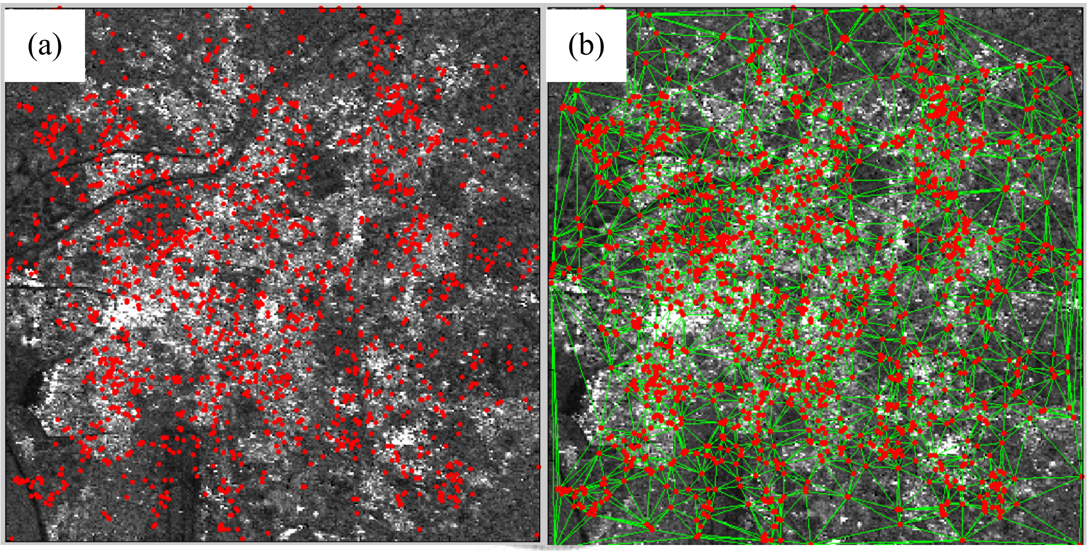

Figure 3.7. Selected points using (a) the coherence criterion and (b) the Delaunay Triangulations before removing the links over 1-km length above the amplitude image of the study area.

After processing the data using the algorithm for linear deformation estimation, there are 1236 points remained from the initial 1649 points according to the quality test ($\gamma_{model} \geq 0.7$). The result can be observed on the slant range deformation velocity in Figure 3.8. Most PS points are sat on the roads and buildings, which is fit in with what I expected. The linear deformation measurements show a maximum of SRD rate of about 8 mm/yr on the center of the Tainan Tableland. The subsidence area located in the west of the Tainan Tableland with a SRD rate of about -5 mm/yr and the Tawan Lowland with a SRD rate of about -10 mm/yr. However, the Chungchou Terrace is a stable terrace without obvious motion during the time period.

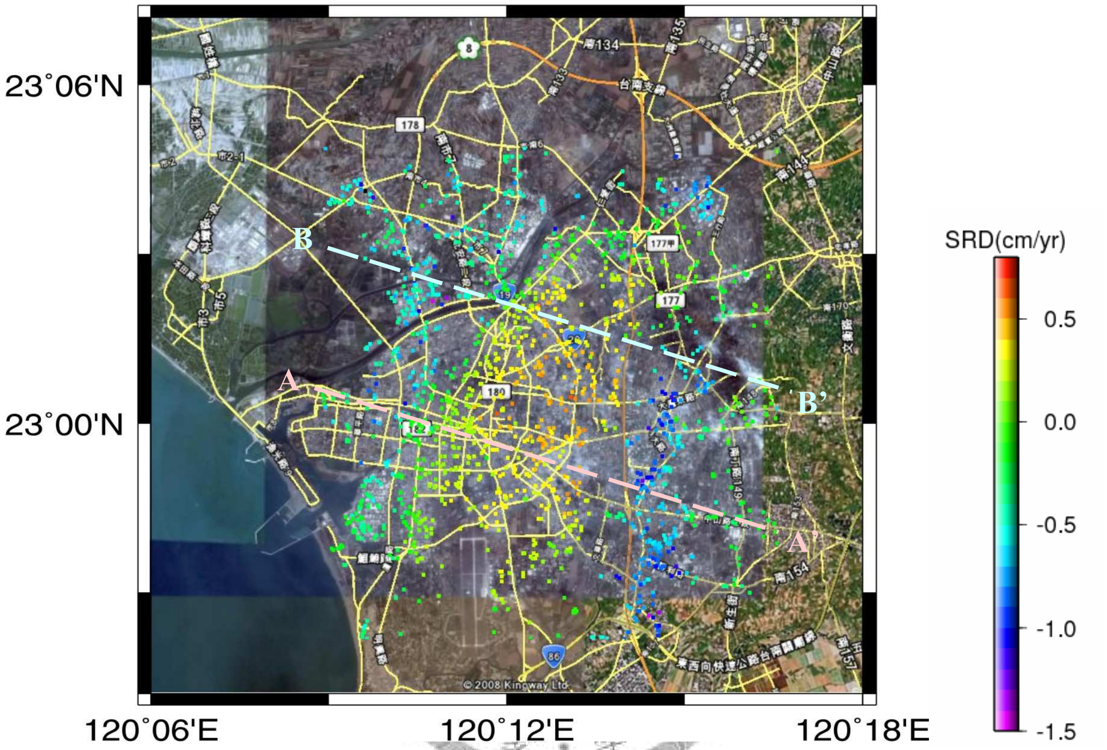

Figure 3.8. The SRD rate (cm per year) over PS points of the area under study superimposed on the map from Google Earth. The maximum velocity toward the satellite is 0.8 cm/yr on the central of the Tainan Tableland, and the maximum velocity away from the satellite is 1.5 cm/yr on the Tawan Lowland.

Along the profile AA' and BB' in Figure 3.8, the continuous deformation change on the Tainan area can be observed. The SRD rate on the northeastern (AA') is higher than southeastern (BB') Tainan Tableland (Figure 3.9). From the west, both AA' and BB' are manifest an increasing of SRD rate from western edge to eastern edge of the Tainan Tableland but a sudden and severe decreasing of SRD rate when going into the

Tawan Lowland, which indicates the location of the Houchiali fault. Interesting, the result coincides with the topographic profile across the Tainan area, and the predicted location of northern part of the Houchiali fault is close beneath the high way No. 1 (orange line in Figure 3.8).

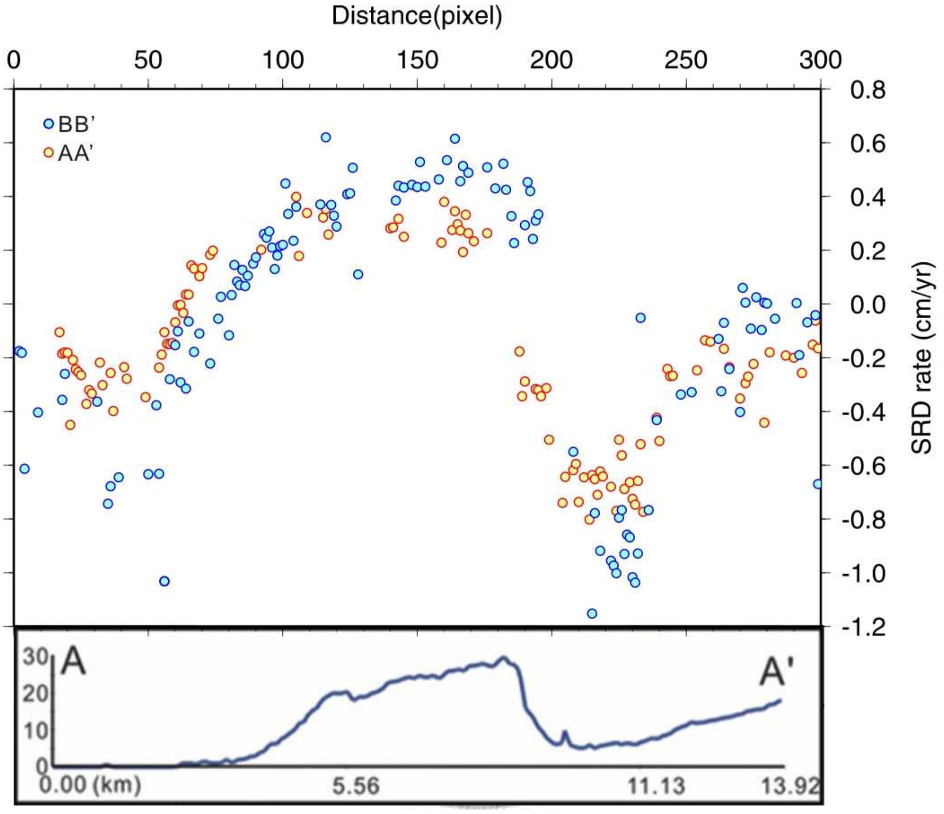

Figure 3.9. Upper Panel: Linear SRD rate along AA' and BB' profiles based on Figure 3.8. Lower Panel: Topographic profile across the central Tainan Tableland.

Once the linear deformation has been obtained, the nonlinear deformation estimation algorithm has been applied to retrieve the full deformation evolution. The time series of deformation for the whole processed region is shown in Figure 3.10. Although the parameter of the cut frequency to discriminate the nonlinear displacement component from the atmospheric is necessary, without *a priori* information it is difficult to estimate this frequency. In this case study, I use nonlinear deformation with a general 25% of the low band to produce the result [*Mora et al.*, 2003]. In the future, the suitable cut frequency for the Tainan area should be found out to complete the deformation evolution.

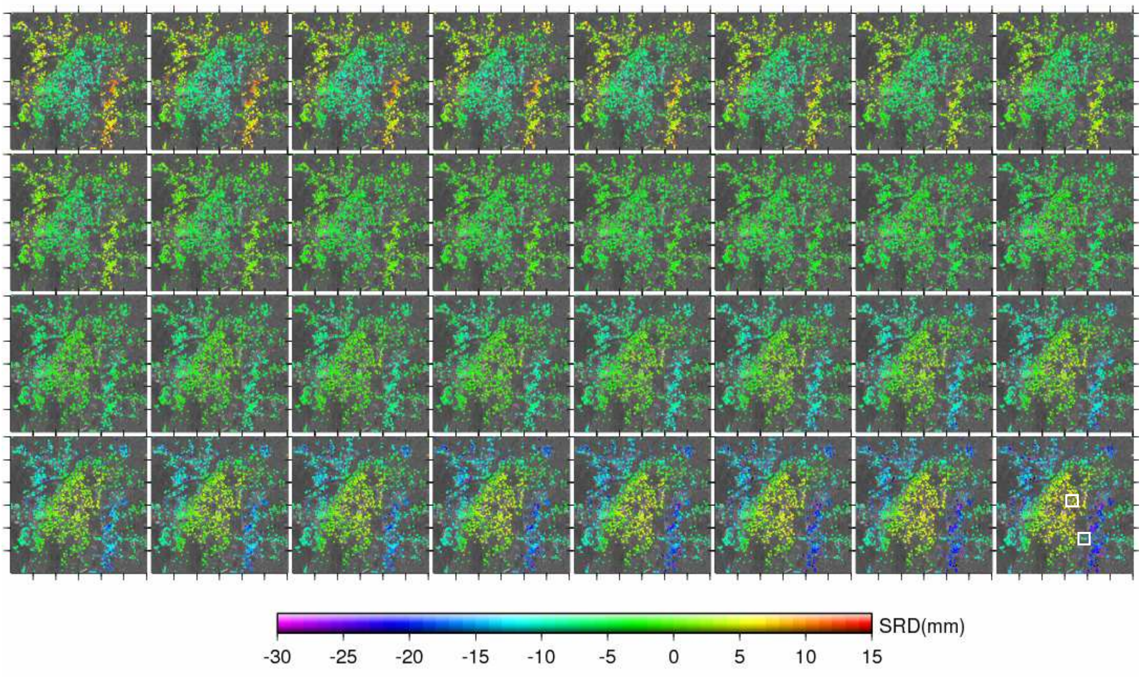

Figure 3.10. Time series of deformation superimposed on the amplitude image of study area. White rectangles in the last deformation pattern are the area location of selected six points. The master image is acquired on 10 July 1997.

From the PS phases I present a time series of deformation on six points individually in Figure 3.11 (area location in Figure 3.10). Point I, II and III located on the most uplift area on the Tainan Tableland. In addition, point I with the largest deformation presents a very linear trend of displacement from 1996 to August 1999 with slight perturbations. On the other hand, point IV, V and VI located on the area with subsidence with similar deformation pattern.

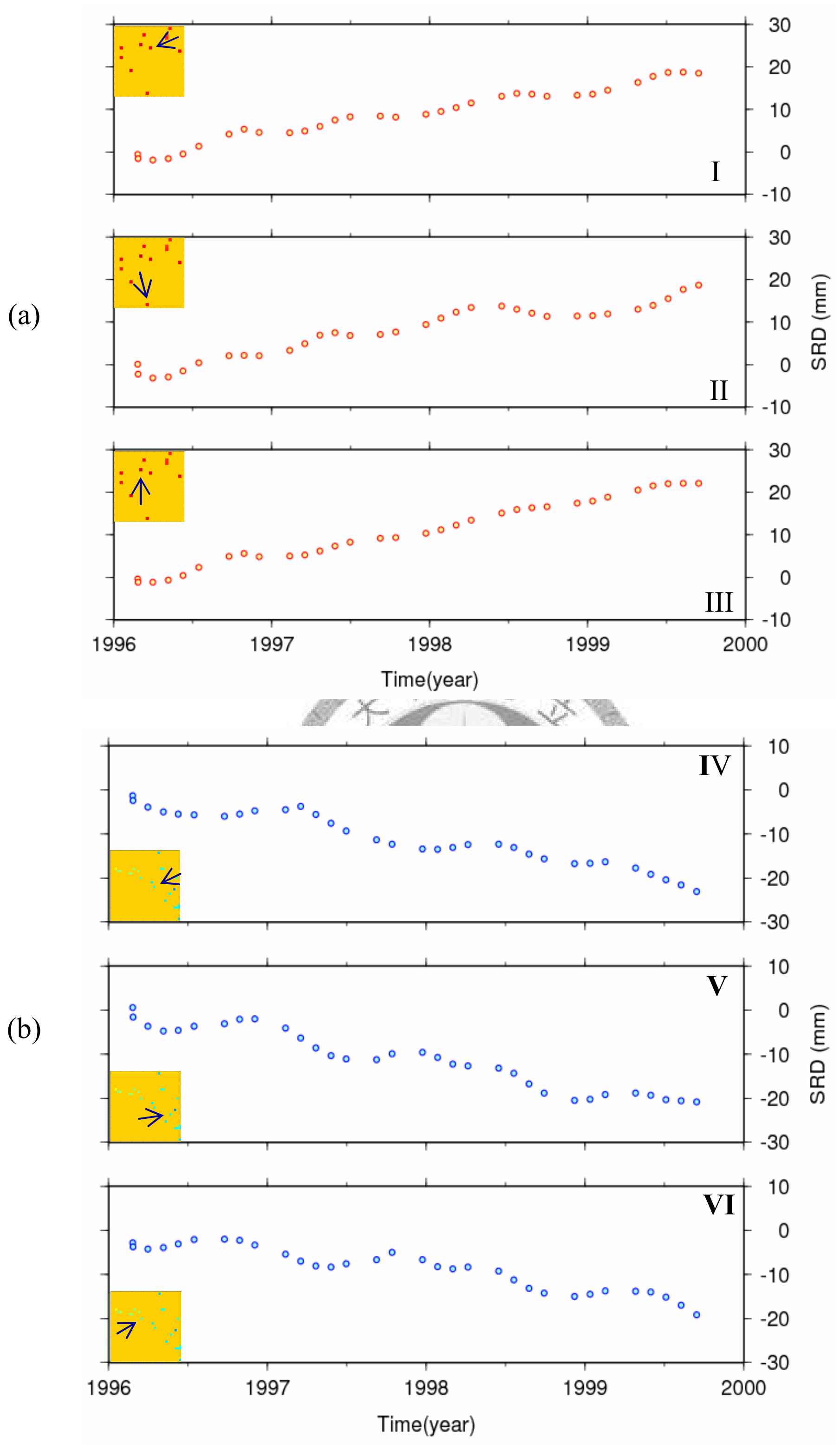

Figure 3.11. Deformation evolutions of points. (a) Red circles reveal deformation on the Tainan Tableland, and (b) blue circles on the Tawan Lowland.

3.4 Discussions

3.4.1 Sequence stratigraphy analysis

According to the data of boreholes revealed by *Zhou* [2007], the long-term deformation rate is close to the short-term deformation rate in Tainan area. The maximum uplift rate on the axis of Tainan Tableland is 4.6 mm/yr, and reduces to 0.6 mm/yr and 0.2 mm/yr on the eastern and western edge respectively. The subsidence rate is about 1.2 to 2.9 mm/yr on the Tawan Lowland (Figure 3.13).

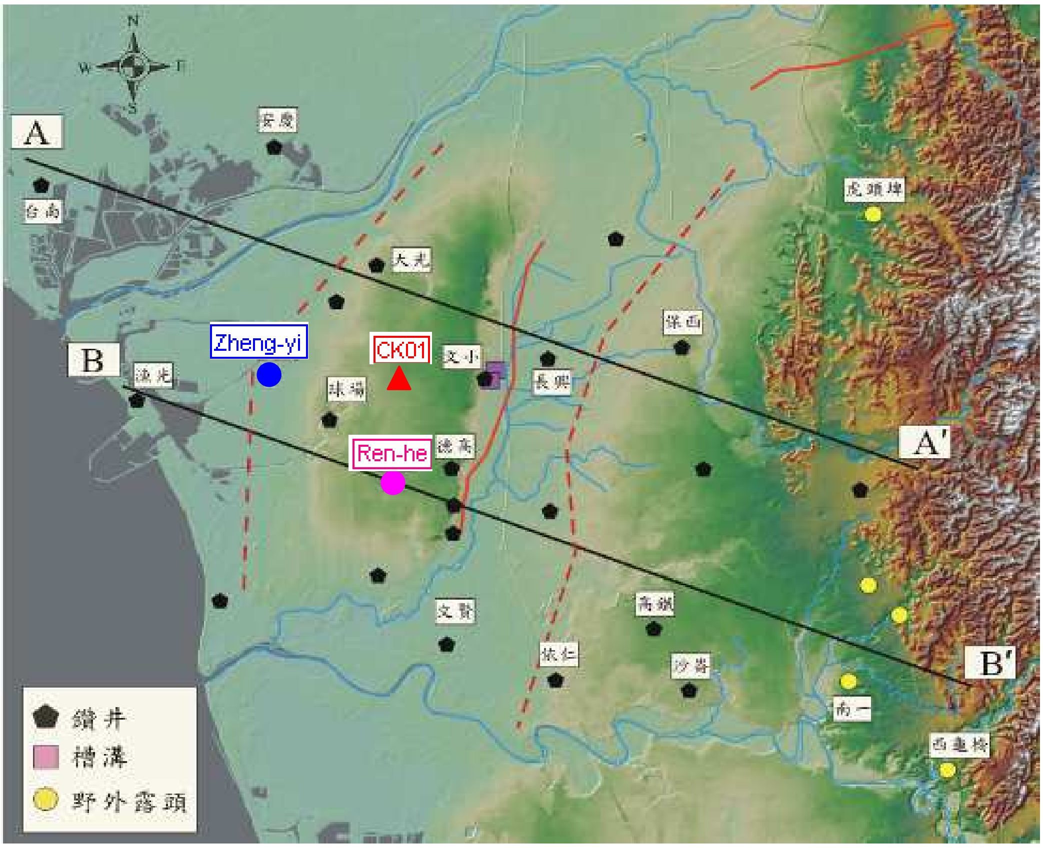

Figure 3.12. Locations of profiles, cores, trough ditch, and outcrops. Bule circle is Zheng-yi Park site with uplift rate close to zero and pink circle is Ren-he site which is the closest to continuous GPS station CK01 (red triangle).

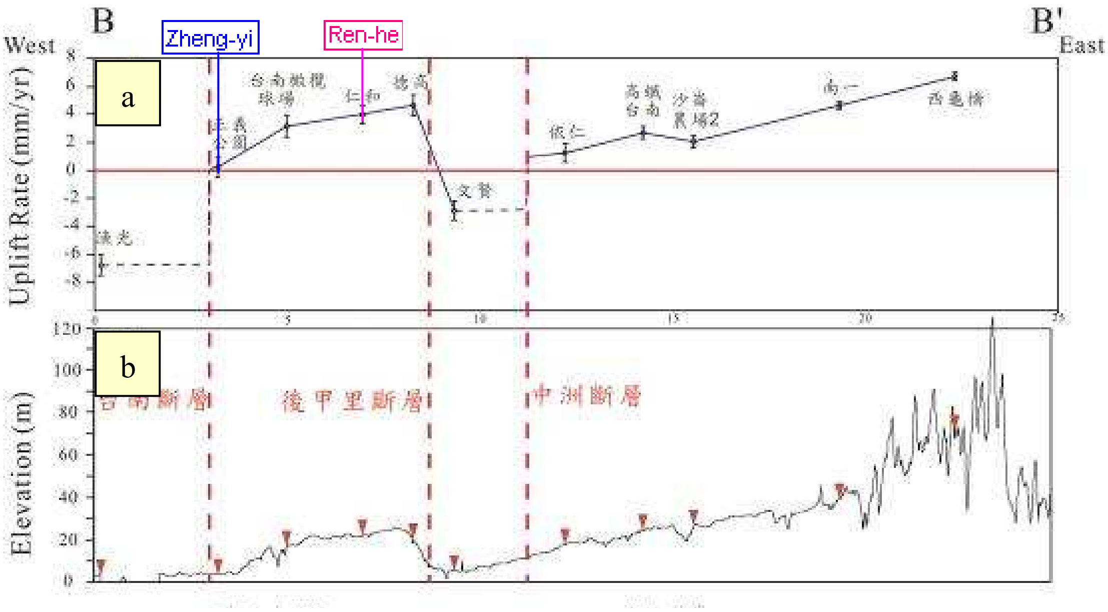

Figure 3.13. (a) Long-term deformation rate projected on to BB' cross section and (b) topographic profile along BB' cross section [*Zhou*, 2007].

Since the SRD can reveal only one-dimensional deformation information, I transfrom the LOS to vertical displacement by using 3D conversion developed by *Hunag* [2006] (Figure 3.14). The average horizontal velocity of continuous GPS at continues station CK01 (red triangle in Figure 3.12) during January 1996 to August 1999 is about 14 mm/yr in the direction 275 degrees (Figure 3.15). The PS points close to the CK01 station represent a velocity about 4.7 mm/yr along the LOS (pink circle in Figure 3.12) which indicate a vertical velocity 5.1 mm/yr by using Zheng-yi Park as a reference point equal to zero displacement (blue circle in Figure 3.12). According to the result of boreholes by *Zhou* [2007], the long-term uplift rate on the shallowest layer of Ren-he site is 5.1±0.2 mm/yr which is close to our data.

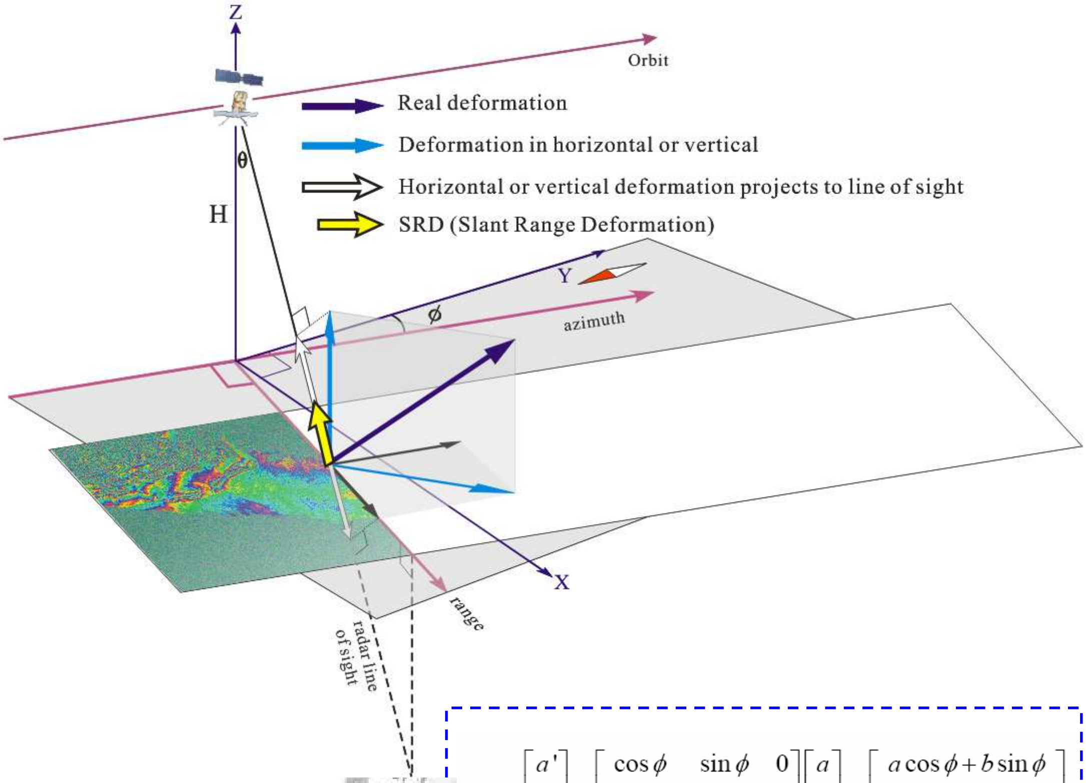

$$\mathbf{V}=\begin{bmatrix}a'\\b'\\c'\end{bmatrix}=\begin{bmatrix}\cos\phi & \sin\phi & 0\\-\sin\phi & \cos\phi & 0\\0 & 0 & 1\end{bmatrix}\begin{bmatrix}a\\b\\c\end{bmatrix}=\begin{bmatrix}a\cos\phi+b\sin\phi\\-a\sin\phi+b\cos\phi\\c\end{bmatrix}$$

$$h=\Delta r\sec\theta-(a\cos\phi+b\sin\phi)\tan\theta$$

Figure 3.14. The geometrical relationship of the SRD, observed deformation, horizontal and vertical deformation based on geodetic measurements and the projection of the vertical and horizontal components onto LOS towards satellite. Where ϕ is intersection angle between the trace of satellite and the north; a and b are the projection of displacement of GPS along east and north, respectively. a' and b' are the projection of V onto parallel and perpendicular the trace of the satellite, respectively. Δr is the SRD, θ is the looking angle of satellite, and h is the vertical displacement [Huang, 2006].

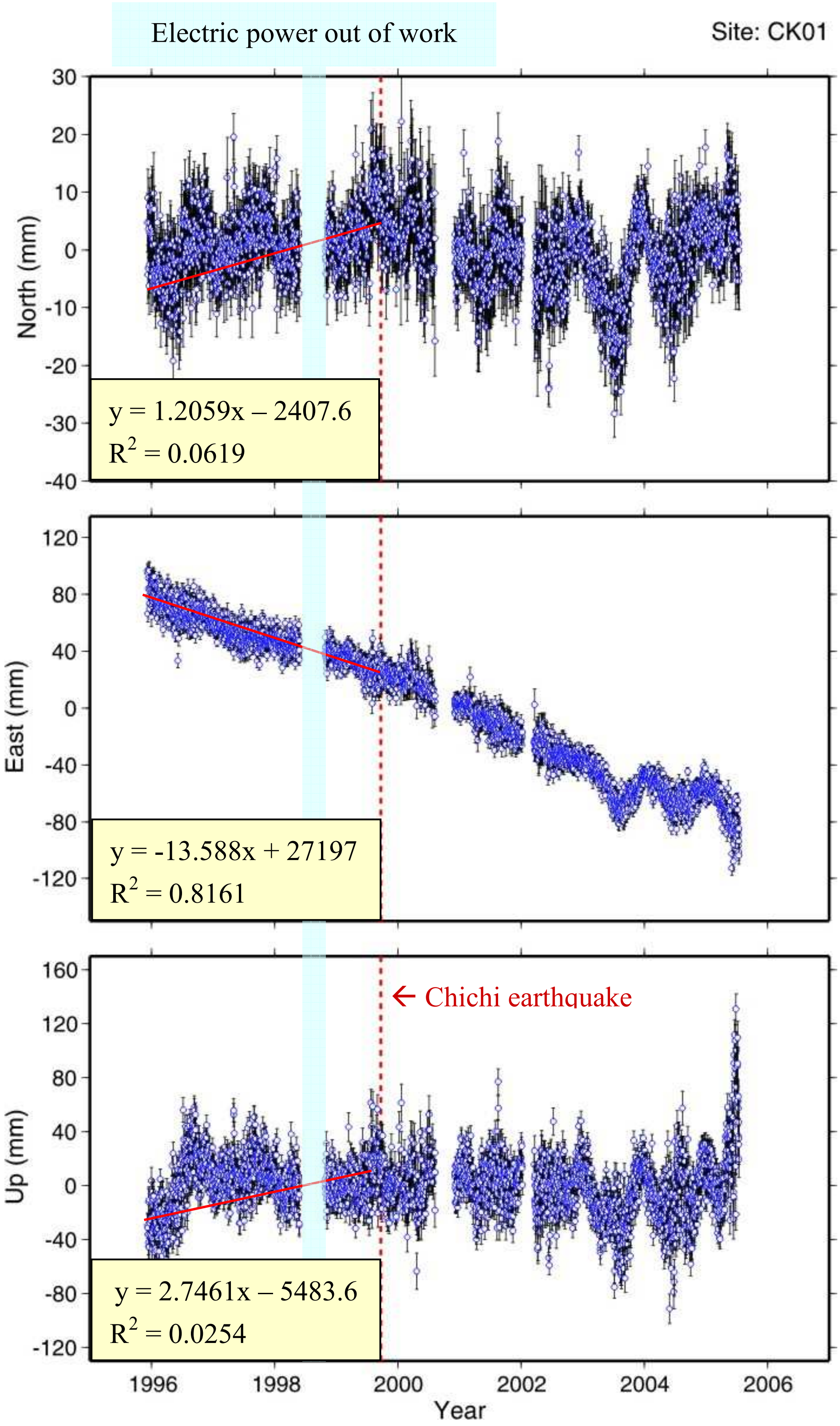

Figure 3.15. GPS components (N-S, E-W and up-down) at station CK01 during 1996 to 2006.

3.4.2 Precipitation and groundwater level data

Since the deformation evolution seems to have a vibratory pattern in each point, I compare the data with precipitation and groundwater level in order to better understand the relationship between nonlinear deformation pattern and hydrologic parameters.

The precipitation in study area here is presented as average rainfall data, which obtained from two nearby meteorological stations of the **C**entral **W**eather **B**ureau (**CWB**) at Tainan station during 1996 to 1998 and Yongkang station during 1998 to 2000 (Figure 3.16 for location). In summary, the wet season in the Tainan area is generally from April to August; however, it varies slightly each year. From the Figure 3.17, the wet/dry seasons for the period of the observation can be defined.

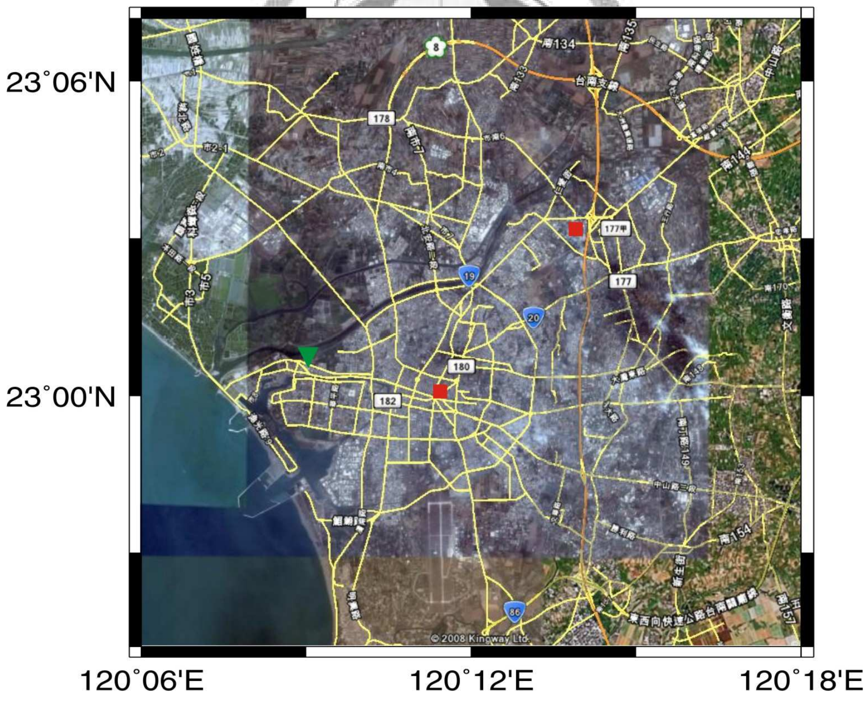

Figure 3.16. Location map of precipitation stations (red rectangles) and groundwater observation well (green inverted triangle) superimposed on the map from Google Earth.

The data of groundwater level presented here were obtained from an hourly measured observation well from **W**ater **R**esources **A**gency (**WRA**). This well is located at Anping near the Tainan city (Figure 3.16 for location). The groundwater level during the period of 1996 to 2000 shows a rapid rising when it comes to rainy season and in general dropping down during the dry season (Figure 3.17). Thus the water level also shows the seasonal change, it demonstrates a similar pattern with the precipitation data. However a decreasing of the groundwater level during the wet season is observed of 1998 to 1999. Therefore it becomes more difficult to determine the relationship with nonlinear deformation.

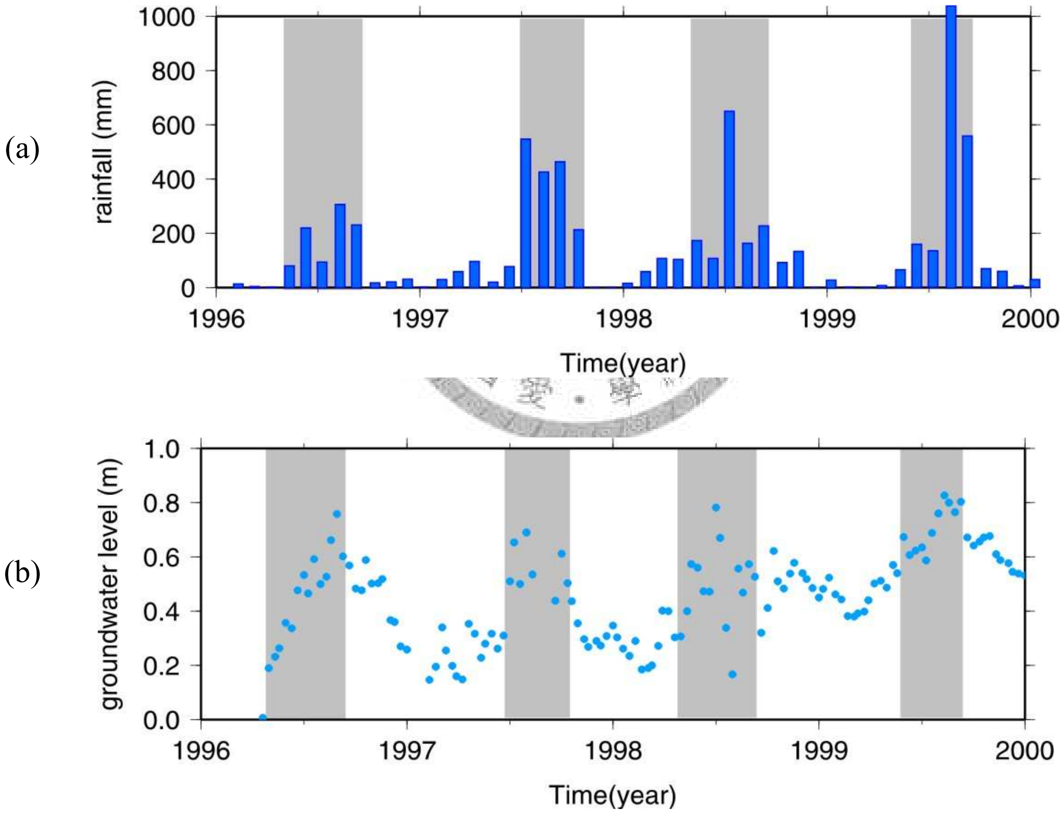

Figure 3.17. (a) Monthly rainfall data at Tainan during 1996 to 1998 and Yongkang during 1998 to 2000. There are more than 150 mm/month observed during the rainy season (in gray) generally from April to September. (b) Semimonthly groundwater level from the nearby observation well at the Anping station.

3.4.3 Seismicity data

The seismicity data used were recorded by CWB seismic network from 1996 to 2000, which coincides with the time span of our observation. Figure 3.18 reveals the seismicity with magnitudes between 0 with 5 on the southwestern Taiwan. Most of the seismicities are deeper than 10 km, which are under the décollement proposed by *Huang et al.* [2004]. Besides, there is no seismicity happened on and around the southern Tainan Tableland and the Houchiali Fault.

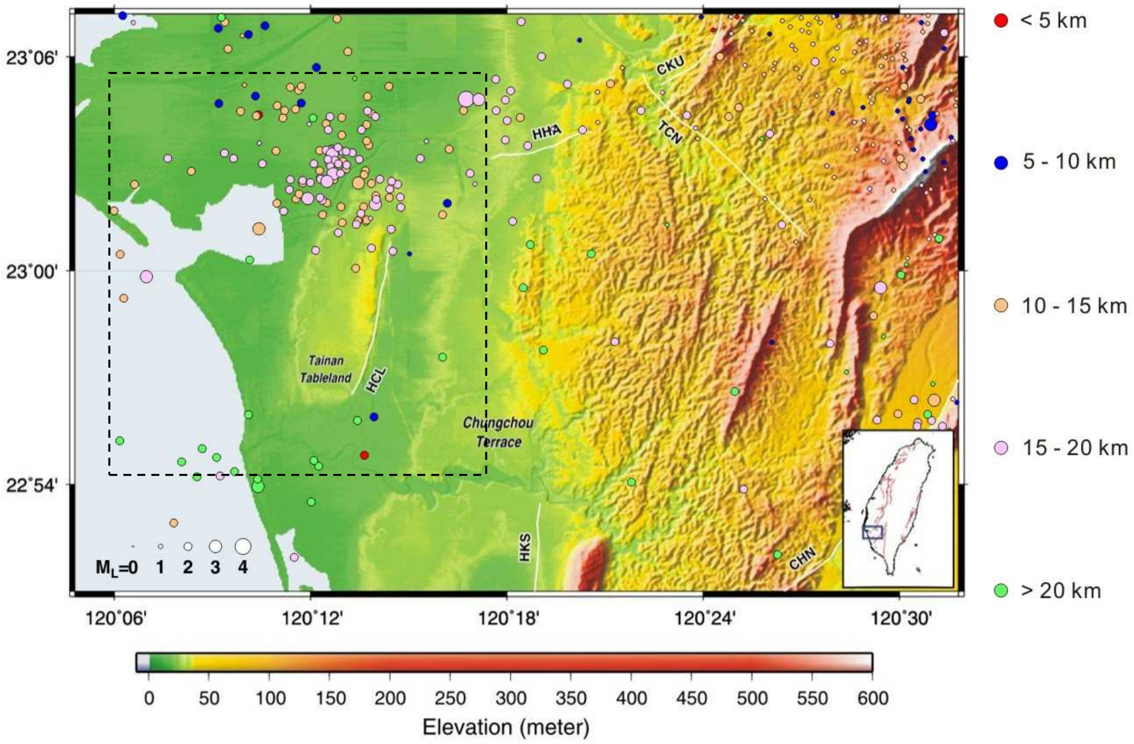

Figure 3.18. Map of seismicity in Tainan city and surrounding areas. Dot square is our study area.

Because there are just few shallow seismicities happened here, I also calculate the number of seismicity happened in each month (Figure 3.19). However, there is no clear relationship between rainfall and seismicity. Nevertheless, the moment of rupture is differ from image acquired. In Figure 3.6 there is no coseismic pattern can be observed in any interfergram. Therefore, the seismicities happened here should not cause the nonlinear deformation vibrations.

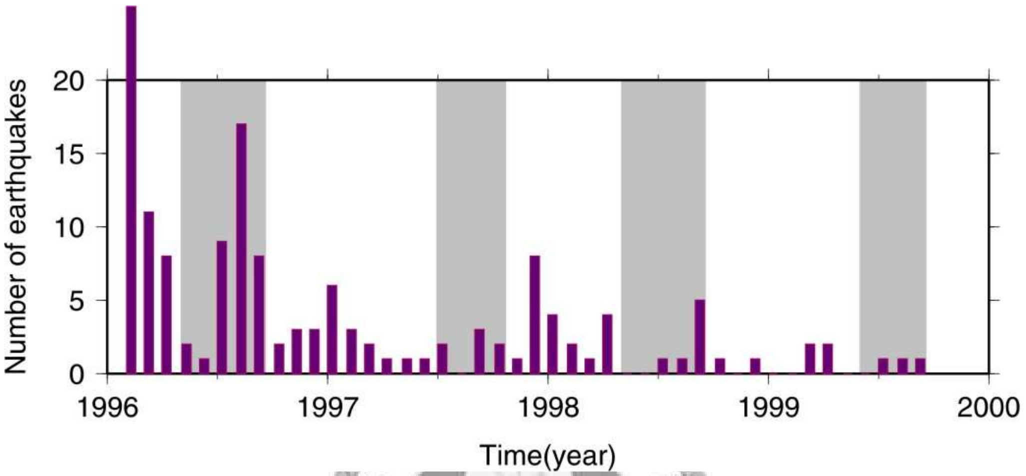

Figure 3.19. Numbers of earthquakes happened in study area from January 1996 to August 1999. There is no correlation between rainfall (in gray background) and numbers of earthquakes.

3.4.4 Nonlinear Deformation Analysis

Figure 3.20 illustrates the time series of nonlinear deformation of five PS points extracted from the deformation evolution on the eastern Tainan Tableland. Basically, the nonlinear deformation characterizes with high spatial correlation in each pixel within a small area. However, I use a general 25% of the low band to produce the nonlinear deformation. As a consequence, the average of whole PS points can reduce the spatial noises and represent the nonlinear deformation evolution on the Tainan Tableland (red rectangle) and Tawan Lowland (white rectangle) in Figure 3.21.

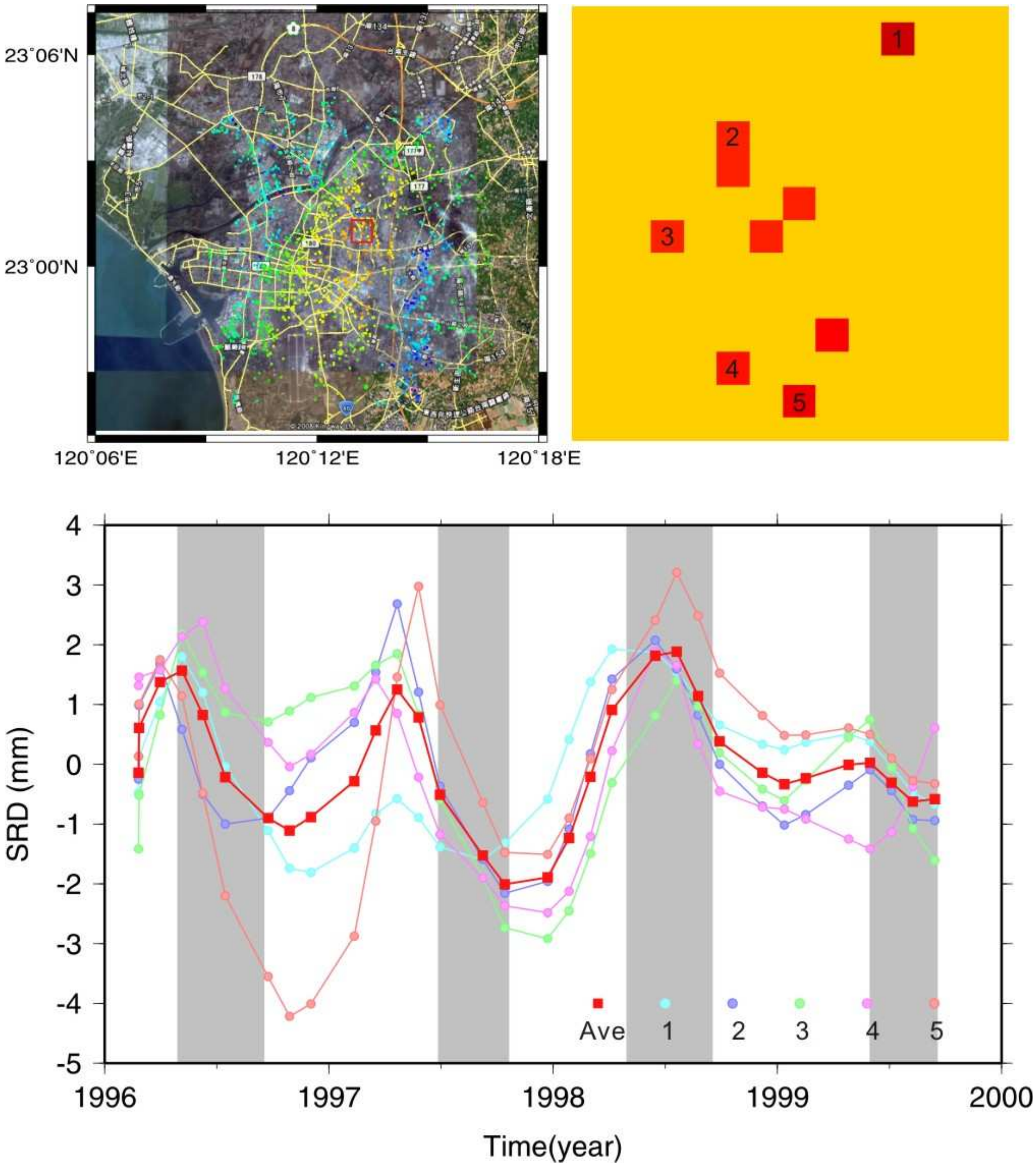

Figure 3.20. Nonlinear deformation of five PS points extracted from the deformation evolution on the eastern Tainan Tableland.

The nonlinear deformation evolutions in Figure 3.21 show a respectable correlation with seasonal rainfall near the Houchiali Fault on the Tainan Tableland (point 1 and 2). These two areas indicate that the SRD at a relatively high value when it comes to wet season. In contrast, it seems to drop after the wet season. However, the area away from the Houchiali fault does not show the correlative to seasonal rainfall (point 3 and 4). Moreover, the two areas on the Tawan Lowland show the same distribution but with an arrearage of time interval to return (point 5 and 6).

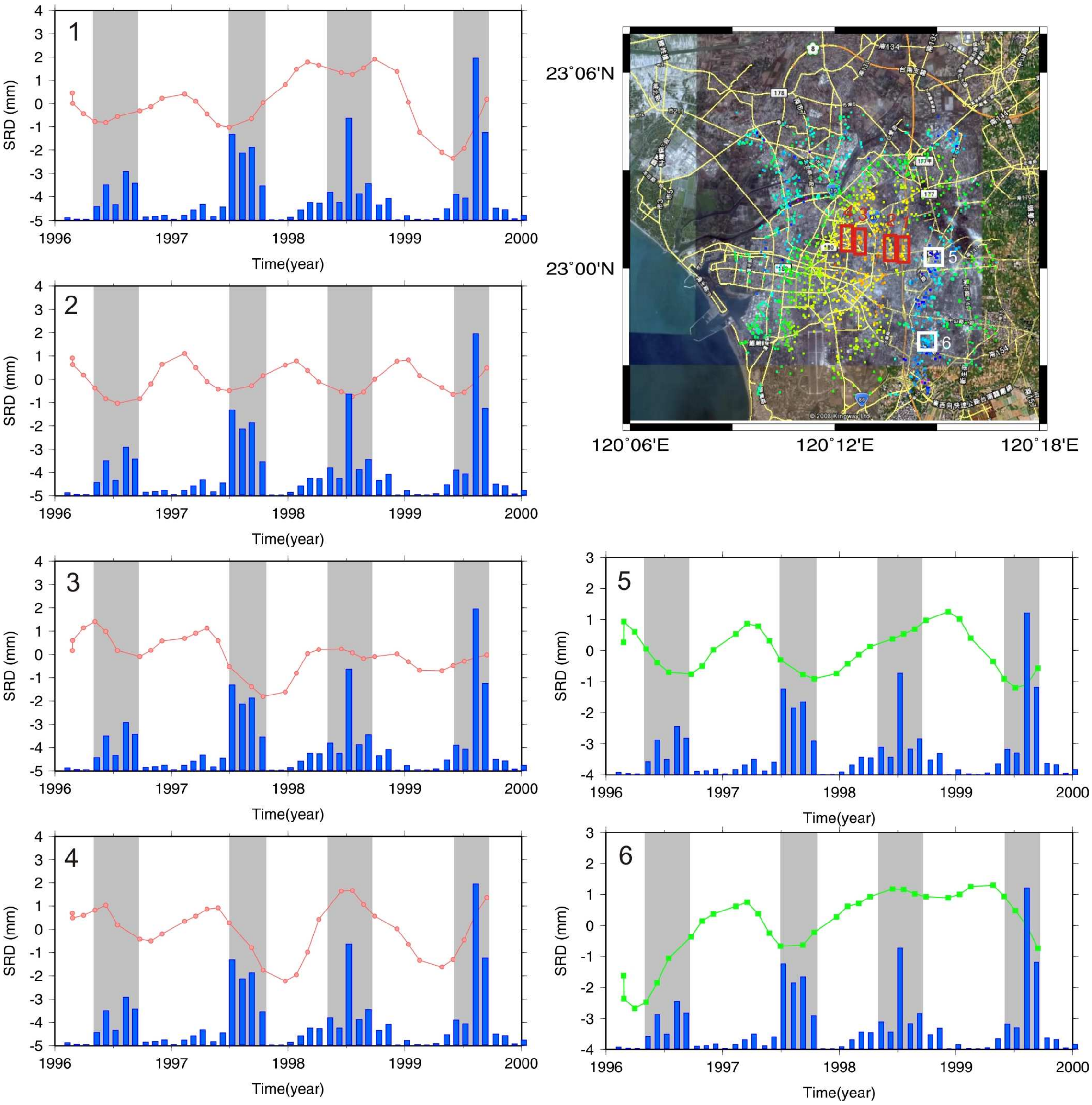

Figure 3.21. Comparison of nonlinear deformation evolution and seasonal rainfall data. Point 1, 2, 5 and 6 show a respectable correlation with seasonal rainfall, on the contrary, point 3 and 4 show no correlation with seasonal rainfall.

Due to the locations of precipitation station and difference of fault mechanism on hanging wall (Tainan Tableland) and footwall (Tawan Lowland), the nonlinear deformation show a slight difference of returning time on the Tainan Tableland and Tawan Lowland. However, both of them indicate that the Houchiali fault might have a behavior of fault creeping during the rainy seasons.

Based on the result from sequence stratigraphy dating, the long-term uplift rate from borehole data is close to the short-term uplift rate inferred from radar interferometry, which implies that the Houchiali fault should act as an aseismic creeping faulting from the viewpoint of seismic cycle. Thus the seismic hazard assessment is a crucial topic to evaluate the fault systems east of the Houchiali fault. As long as the cut frequency can be found out in the future, the fault mechanism in study area can be clearly understood.

3.5 Summary

This case study has presented a new InSAR technique, PSInSAR, for detecting active deformation in Tainan area by using ERS SAR images. The conclusions list as followings:

1. There are 1649 PS points have been identified by using spatial coherence. After the quality test there are 1236 points remained from the initial points. The PS density is about 8.6 PS/km^2, which is enough to overcome the atmospheric affections.
2. During the time period of 1996 to August 1999, the linear deformation measurements show a maximum SRD rate of 8 mm/yr on the central part of the Tainan Tableland. The Tawan Lowland indicates a SRD rate of about -10 mm/yr.
3. The PS points close to the CK01 station represent a SRD rate of about 4.7 mm/yr which indicate a vertical velocity 5.1 mm/yr by using Zheng Park as a reference point. This result is quite close to the borehole data.
4. The nonlinear deformation evolutions show a respectable correlation with seasonal rainfall near the Houchiali fault, and no correlation with seasonal rainfall away from the Houchiali fault.
5. The short-term uplift rate predicted by PSInSAR is close to short-term uplift rate, it implies that the Houchiali fault demonstrates an aseismic creeping behavior.

國立臺灣大學

Chapter 4

Land Subsidence in Central Taiwan

In the previous chapter I present the persistent scatterers result applied to the Tainan area. According to the successful test, I apply the PSInSAR to monitor heavy land subsidence in Yunlin area.

The Yunlin area is one of the counties with serious land subsidence in Taiwan [*Liu et al.*, 2004]. Furthermore the THSR just passes through the central of subsidence area [*Chang and Wang*, 2006]. The monitoring of this serious land subsidence has been made by precise leveling and GPS [*Chang and Wang*, 2006]. Furthermore the D-InSAR was also applied to characterize the land subsidence pattern and the change of land subsidence region [*LSPRC*, 2007]. However, the study area is full of vegetations, thus it causes difficulty using the conventional DInSAR, especially in wet season. Thus, the goal of this study is using PSInSAR technique to deduce the perturbation and to obtain the time series of land subsidence around a section of THSR in Yunlin.

4.1 Introduction

Land subsidence in Taiwan has increased rapidly over the past four decades, owing to heavy withdrawal of groundwater [*Tang and Tang*, 2006]. As a consequence, severe subsidence has occurred in several areas including Taipei, Taoyuan, Changhua, Yunlin, Chiayi, Kaohsiung, Pingtung and Yilan (Figure 4.1a). Thanks to the government's policy for water recharge and reducing of water pumping, most of subsidence area have been stopped subsiding. However, the Changhua and Yunlin area still suffer with the problems of heavy land subsidence (Figure 4.1b).

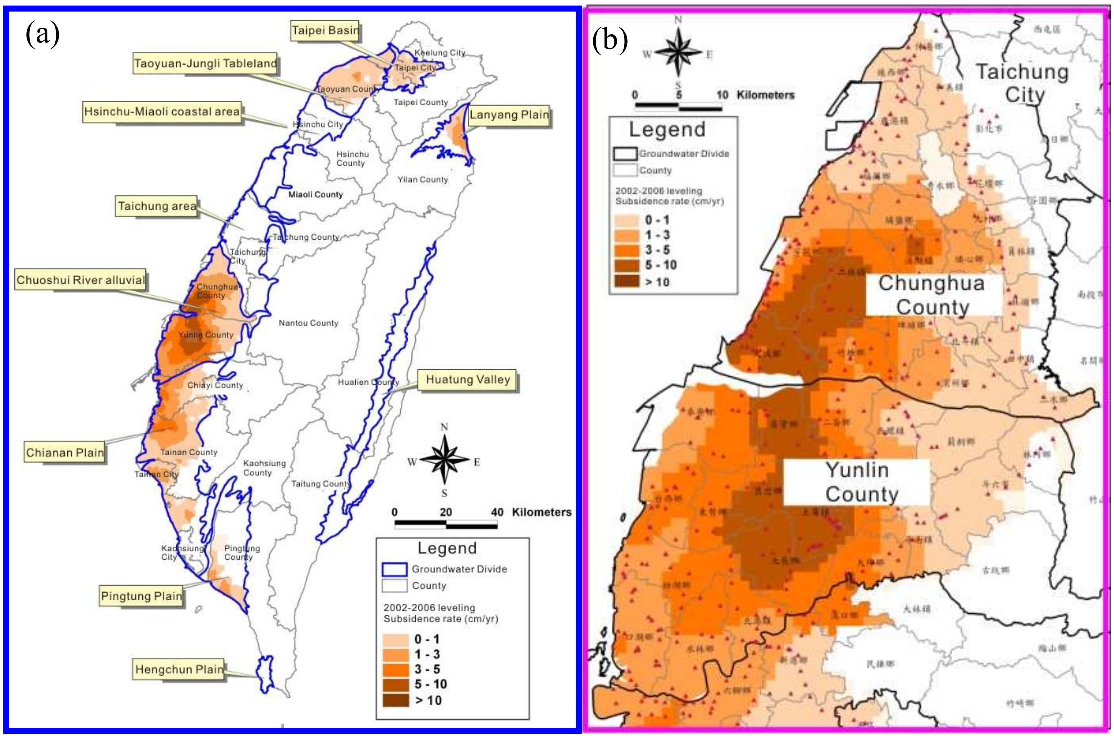

Figure 4.1. Average land subsidence area (a) in Taiwan Island and (b) Chunghua-Yunlin area during 2002 to 2006.

Yunlin County is one of the important agricultural production regions located in the southwestern coastal region of Taiwan where the irrigated area is up to 123,000 hectares and agricultural water consumption reaches approximate 90 percents of all available water resources in the Choshui River Basin [*Zhang*. 2006]. Moreover, since there is no sufficient surface water supplied, groundwater becomes a vital resource for every water consumption targets.

Land subsidence in this region resulting from groundwater over-pumping has been of great concerns since the 1970s, and the elevation change of the ground surface has been monitored since 1975 [*Liu et al.*, 2000]. According to the report of **I**ndustrial **T**echnology **R**esearch **I**nstitute (**ITRI**), the largest cumulative subsidence is more than 110 cm from 1992 to 2007 in the Yuanchang Township where is close to the Taiwan High Speed Railway (Figure 4.2).

The THSR passes through the considered subsidence central with an average speed of 300 km per hour and achieves a highest speed of 350 km per hour. With this extreme high speed, the safety problems for THSR are stringent so much.

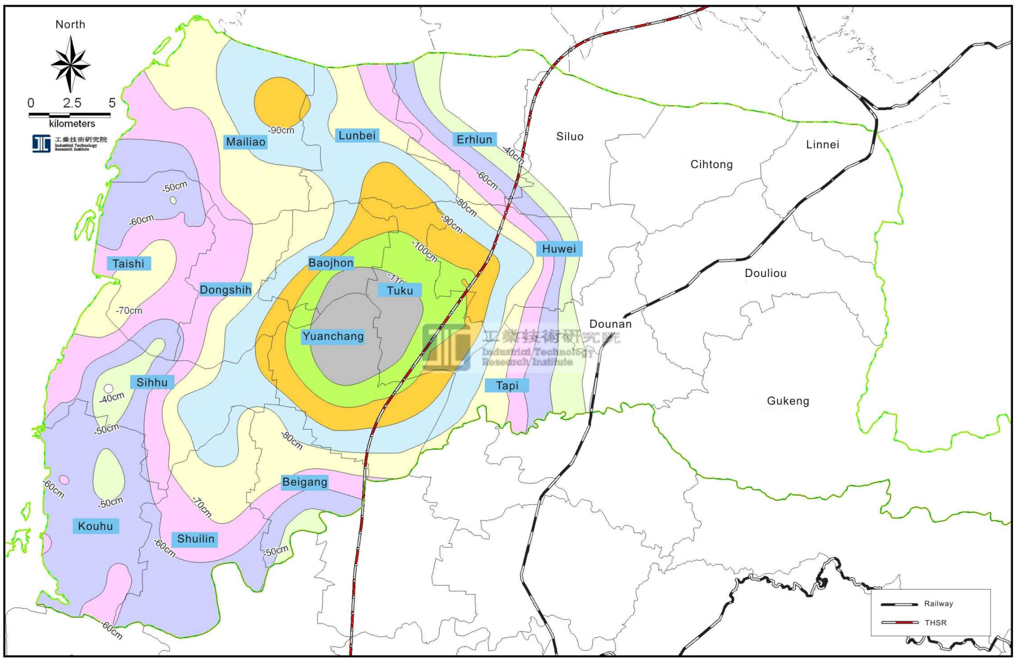

Figure 4.2. Cumulative subsidence in Yunlin County from 1992 to 2007 [*Land Subsidence Database*].

4.2 Regional Setting

4.2.1 Hydrogeologic framework and utilization of groundwater

Yunlin County is located in the in western coastal region of Taiwan and is in the southern part of Choushui River alluvial fan where the sediments are composed of gravel, silt, unconsolidated sand, and clay. Base on rock properties, permeability, dating, and fossils data, the stratigraphic stratum distribution is influenced by the changes in sea level [*Liu et al.*, 2000]. Choushui River alluvial fan can be divided into four marine sequences (aquitard I - aquitard IV) and four non-marine sequences (aquifer I - aquifer IV) at depth of 0 to 300 m (Figure 4.3 and Figure 4.4).

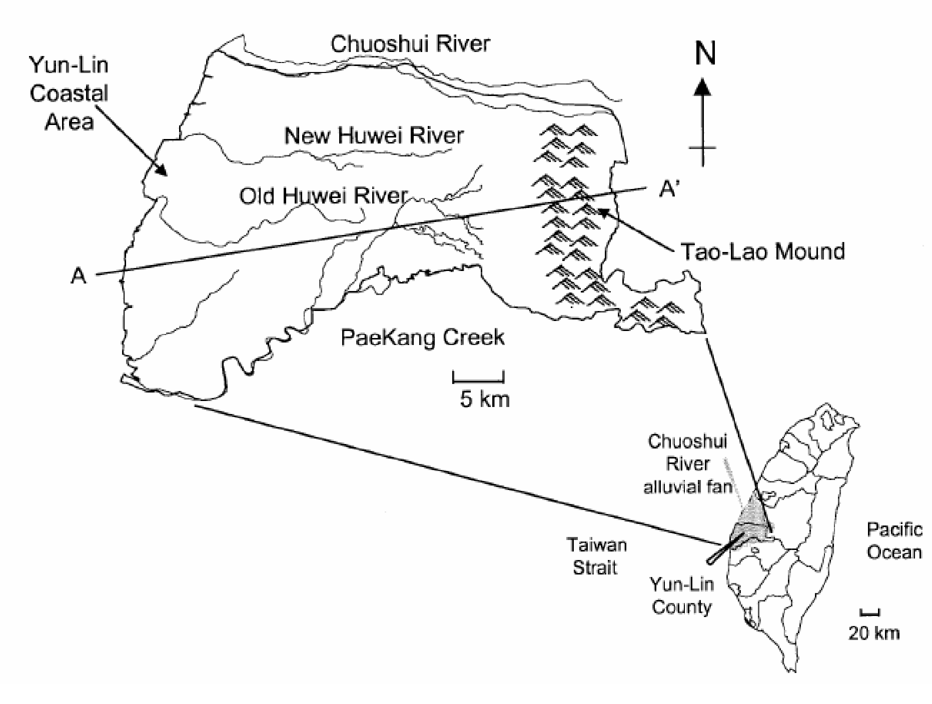

Figure 4.3. Geographical location and geographical environment of the Yunlin coastal area [*Liu et al.*, 2000].

Aquifers are mainly composed of gravel and coarse sand; these kinds of large grain sizes suggest that the aquifers have high hydraulic conductivity. In contrast, aquitards are mainly composed of mud, silt, and fine-grained sands, which contribute to low hydraulic conductivity. In these eight interlayering sequences, aquifer II is the most important water bearing formation of the fan area. It has the greatest extent, with a depth of 35–217 m below ground surface and a thickness of 76–145 m. Its average thickness is about 95 m which is the thickest of the four aquifers.

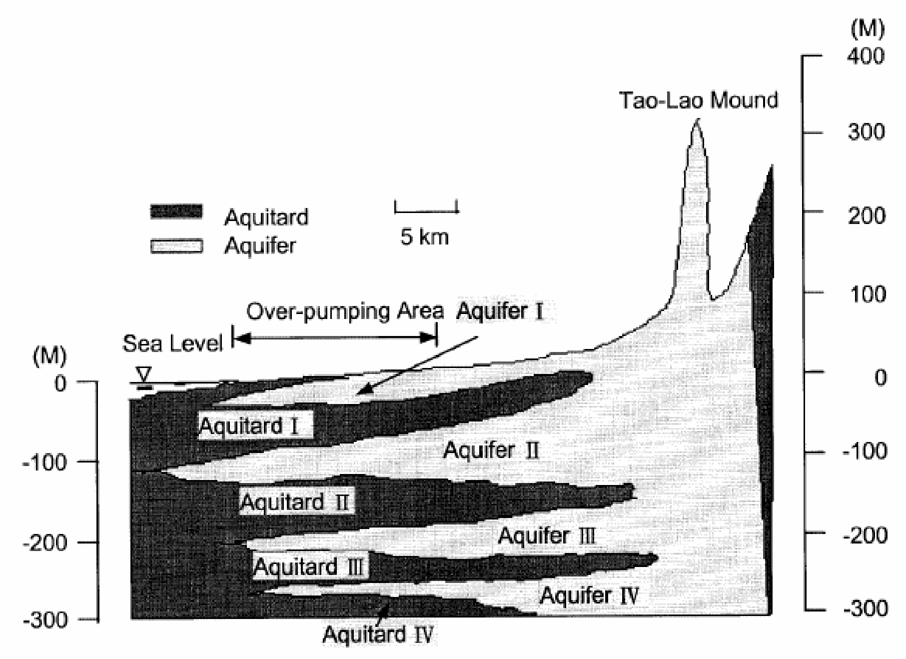

Figure 4.4. Conceptual hydrogeologic profile of the Chuoshui River alluvial fan at the cross section (AA') indicated in Figure 4.3 [*Liu et al.*, 2000].

A multi-leveled land subsidence monitoring well contains 13 subsidence measuring sensors was set up in 1989 [*TBWCP*, 1990; 1997]. The accumulated land subsidence showed monotonic increases with time in all positions relative to the reference point, sensor S1, during May 1989 to May 1997. The results also indicate that larger amounts of accumulated subsidence could be observed in the strata below the position of sensor S10. This accumulated land subsidence distribution is coincident with the hypothesis that over-pumping of groundwater is the main contributor to land subsidence, since the groundwater is primarily withdrawn from aquifer II in the depth of 50 m below the ground surface in this region (Figure 4.5).

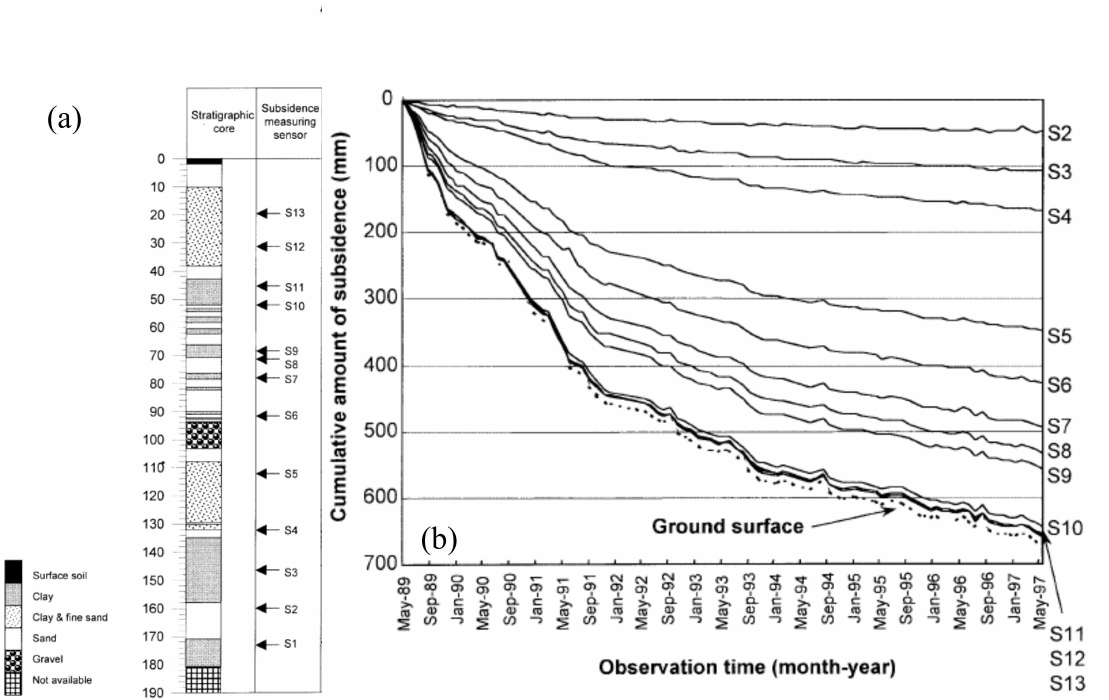

Figure 4.5. (a) Stratigraphic profile and (b) subsidence measuring sensors from 1989 to 1997 in the Yunlin coastal area [*TBWCP*, 1990; 1997].

4.2.2 Precise Leveling Measurement

In order to monitor the subsidence rate, the government has carried out the leveling measurements in this area for more than two decades. According to the precise leveling measurement maintained by ITRI, the serious subsidence rate is well known to occur along the southwestern coast of Yunlin County, and the average subsidence rate is about 10 cm before 1996 (Figure 4.6). However, Figure 4.7 shows the most subsidence area transfer happened in the inside Yunlin County with a subsidence rate of 7 cm/yr during 1996 to 1999. At the same time, subsidence along the coast has decreased from 10 cm/yr to 3 cm/yr to 5 cm/yr. In addition, the precise leveling data measured after 1999 indicate the subsidence center is located inside Yunlin County, Yuanchang Township and Tuku Township. Furthermore, the subsidence area keeps extending to Baojhong Township with maximum subsidence rate of 10 cm/yr (Figure 4.8).

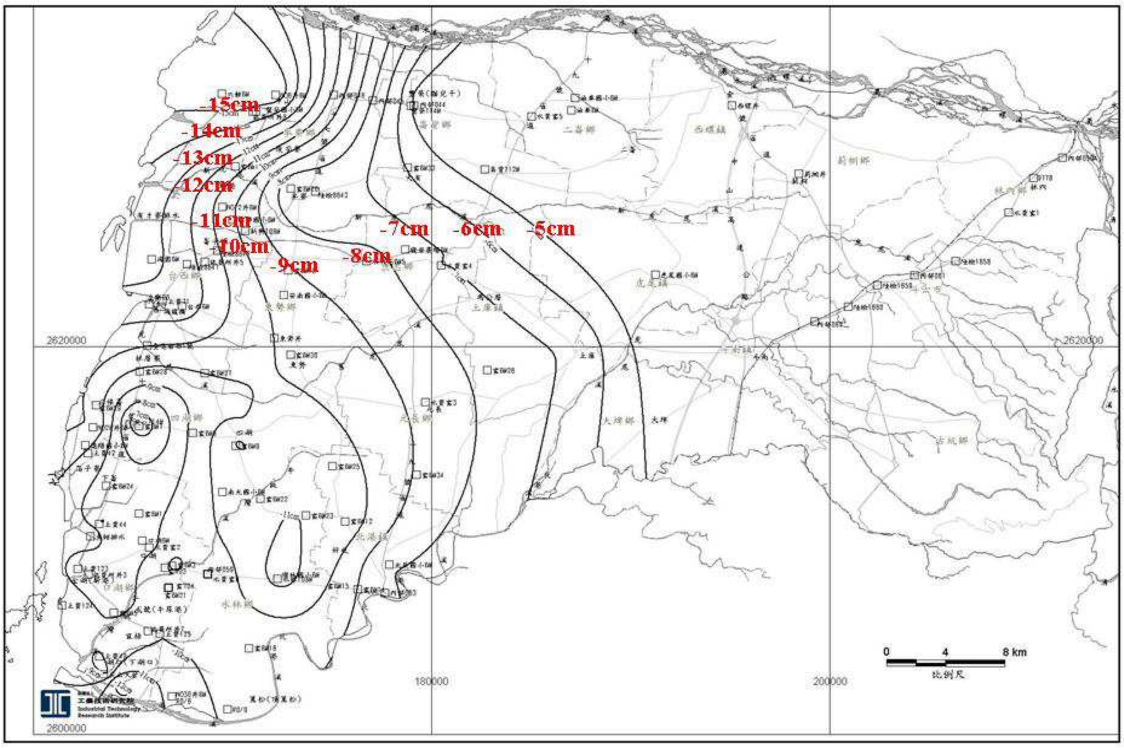

Figure 4.6. Average land subsidence of Yunlin area during 1992 to 1994 [*Land Subsidence Database*].

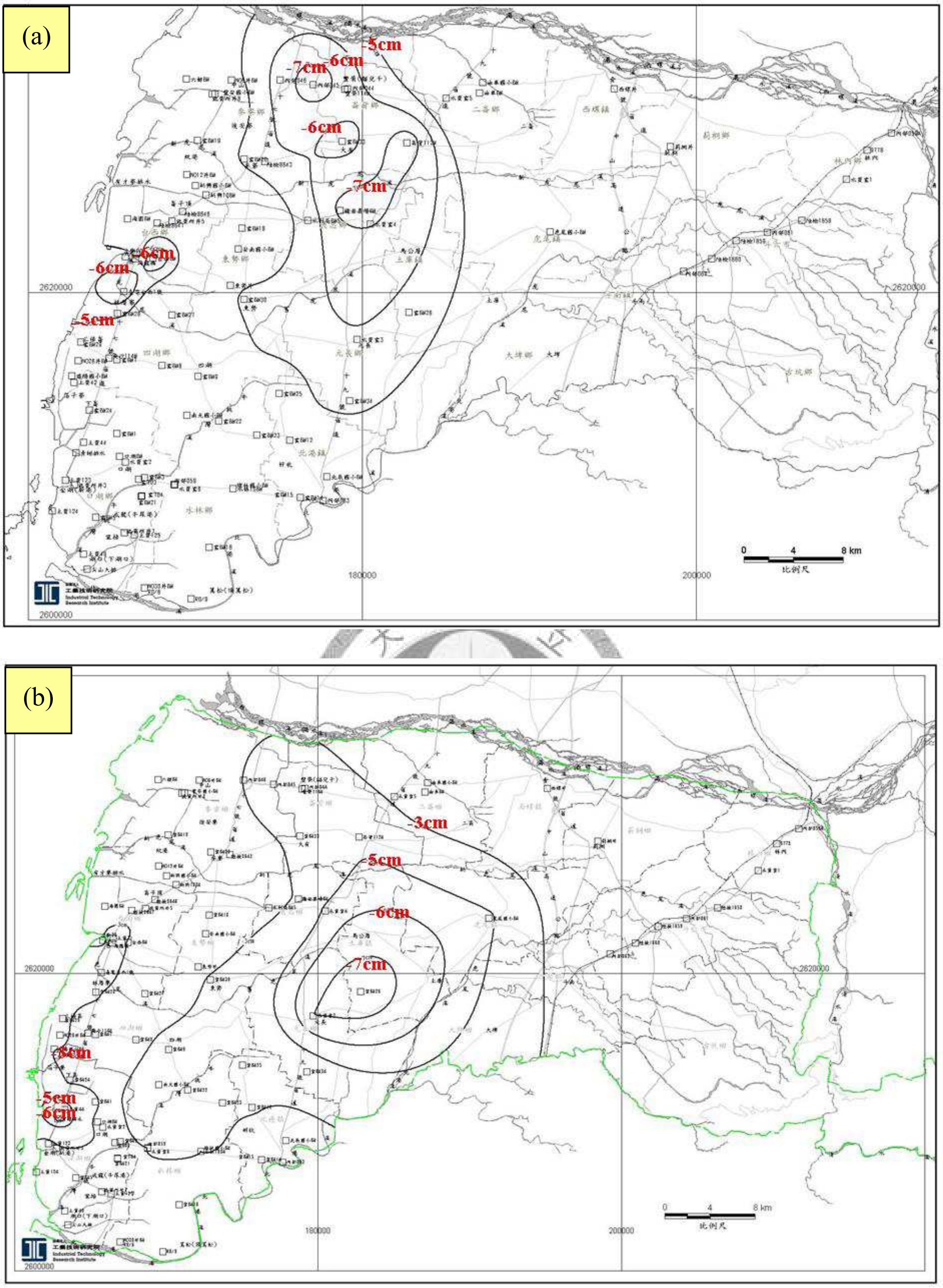

Figure 4.7. Average land subsidence of Yunlin area during (a) 1996 to 1998, and (b) 1998 to 1999 [*Land Subsidence Database*].

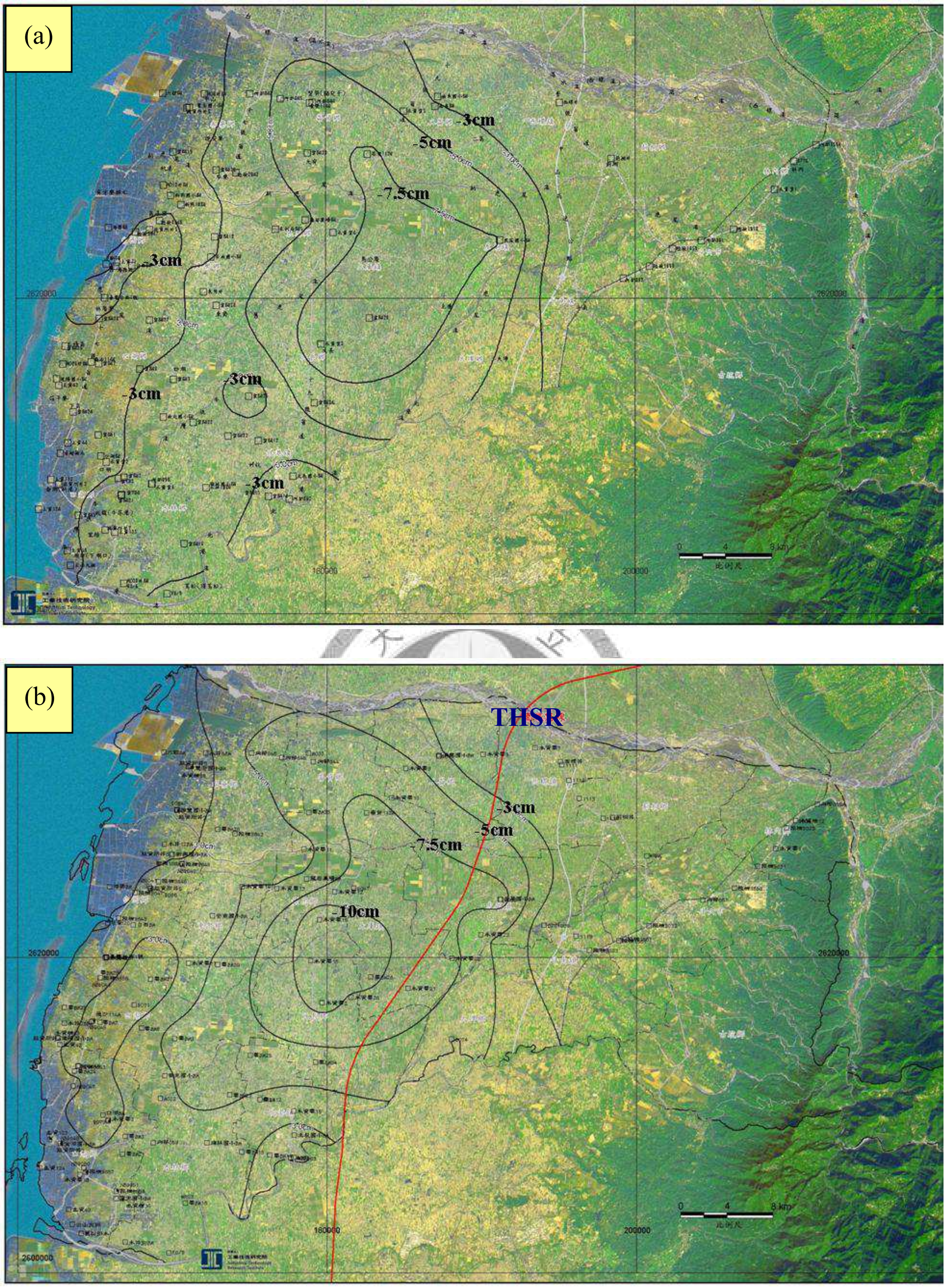

Figure 4.8. Average land subsidence of Yunlin area during (a) 1999 to 2002, and (b) 2002 to 2003 [*Land Subsidence Database*].

4.3 Analyses and Results

4.3.1 Description of Data Analyses

The SAR data set used in this case study includes 33 C-band radar images collected by the ERS-1 and ERS-2 satellites of the ESA in descending orbits (track: 232; frame: 3123) between January 1996 and June 1999. An area of about 18 km long and 12 km wide was selected from the images. Meanwhile the 'Precise Orbit' data are downloaded from the DEOS. The external DEM used to cancel the topographic component of the interferometric phase is the free distribution DEM from NASA's SRTM mission. This is an approximately 90 × 90 m (3 s arc) global DEM with a standard deviation in height of 10 m. In order to increase resolution of geocoded interferograms, the origin DEM interpolated into a finer one (45 × 45 m).

The procedure of differential InSAR is also processed by the software DIAPASON V4.0. The phase unwrapping procedure is processed by the software SNAPHU from Stanford University, USA. SNAPHU is an implementation of the statistical-cost, network-flow algorithm for phase unwrapping which is written in C language. This algorithm poses phase unwrapping as a maximum *a posteriori* probability (MAP) estimation problem, the objective of which is to compute the most likely unwrapped solution given the observable input data [*Chen and Zebker*, 2002]. It is freely available to the public, and the latest version of the code is 1.4.2 in February 2003. Finally, the PSInSAR procedure is processed by MATLAB mentioned in detail in Chapter 3.

Table 4.1. Descending orbit data processed for the Yunlin area (track: 232, frame: 3123). Perpendicular baseline is relative to 19960131 (orbit: 23767).

	Orbit	Date	Sensor	$B_{\perp}$ (m)	FDC (Hz)
1	23767	1996/01/31	ERS-1	0	32.11
2	4094	1996/02/01	ERS-2	127	-4.40
3	24268	1996/03/06	ERS-1	248	30.87
4	4595	1996/03/07	ERS-2	205	-15.69
5	24770	1996/04/10	ERS-1	103	35.24
6	5097	1996/04/11	ERS-2	26	-8.71
7	25271	1996/05/15	ERS-1	152	33.31
8	5597	1996/05/16	ERS-2	20	-8.22
9	6099	1996/06/20	ERS-2	-506	-8.32
10	7100	1996/08/29	ERS-2	-844	-17.07
11	8604	1996/12/12	ERS-2	-561	-9.42
12	8104	1997/01/16	ERS-2	-193	-13.20
13	9606	1997/02/20	ERS-2	-395	-3.94
14	10106	1997/03/27	ERS-2	-119	-3.96
15	10607	1997/05/01	ERS-2	-589	-10.16
16	11108	1997/06/05	ERS-2	-448	-7.98
17	11609	1997/07/10	ERS-2	-409	-6.78
18	12111	1997/08/14	ERS-2	-151	-14.09
19	13613	1997/11/27	ERS-2	-31	-16.47
20	14114	1998/01/01	ERS-2	25	-14.54
21	14616	1998/02/05	ERS-2	-476	-28.00
22	15117	1998/03/12	ERS-2	-530	-12.14
23	16118	1998/05/21	ERS-2	-208	4.81
24	16620	1998/06/25	ERS-2	-1275	-0.048
25	17121	1998/07/30	ERS-2	-109	-0.22
26	17622	1998/09/03	ERS-2	40	1.58
27	18623	1998/11/12	ERS-2	115	-4.97
28	19125	1998/12/17	ERS-2	-711	-10.89
29	19625	1999/01/21	ERS-2	91	-7.32
30	20126	1999/02/25	ERS-2	437	-17.26
31	20627	1999/04/01	ERS-2	-629	-6.54
32	21128	1999/05/06	ERS-2	187	0.12
33	21630	1999/06/10	ERS-2	-217	-0.78

4.3.2 Results of Land Subsidence by Conventional DinAR

In order to solve the problem of spatial decorrelation due to the dense vegetation in study area, I generate interferograms using 35 days interval to enhance the stability of phase coherence. Table 4.2 and Figure 4.9 summarize the details of 17 interferograms.

Table 4.2. Differential Interferograms for Yunlin area (track: 232; frame: 3123).

	Master Image	Orbit	Slave Image	Orbit	$B_{\perp}$ (m)
1	1996/02/01	4094	1996/03/06	24268	121
2	1996/03/06	24268	1996/04/11	5097	222
3	1996/04/11	5097	1996/05/15	25271	126
4	1996/05/15	25271	1996/06/20	6099	658
5	1996/12/12	8604	1997/01/16	9104	368
6	1997/01/16	9104	1997/02/20	9606	202
7	1997/02/20	9606	1997/03/27	10106	276
8	1997/03/27	10106	1997/05/01	10607	470
9	1997/05/01	10607	1997/06/05	11108	141
10	1997/06/05	11108	1997/07/10	11609	39
11	1997/07/10	11609	1997/08/14	12111	258
12	1997/08/14	12111	1997/09/18	12611	528
13	1998/01/01	14114	1998/02/05	14616	501
14	1998/02/05	14616	1998/03/12	15117	54
15	1998/07/30	17121	1998/09/03	17622	149
16	1999/01/21	19625	1999/02/25	20126	346
17	1999/06/10	21630	1999/07/15	22130	156

Figure 4.9 show the 17 interferograms with time interval of 35 days, with no surprise that the coherence is lost completely during the wet season (April to September) seasonal differences in the amount of atmospheric water vapor.

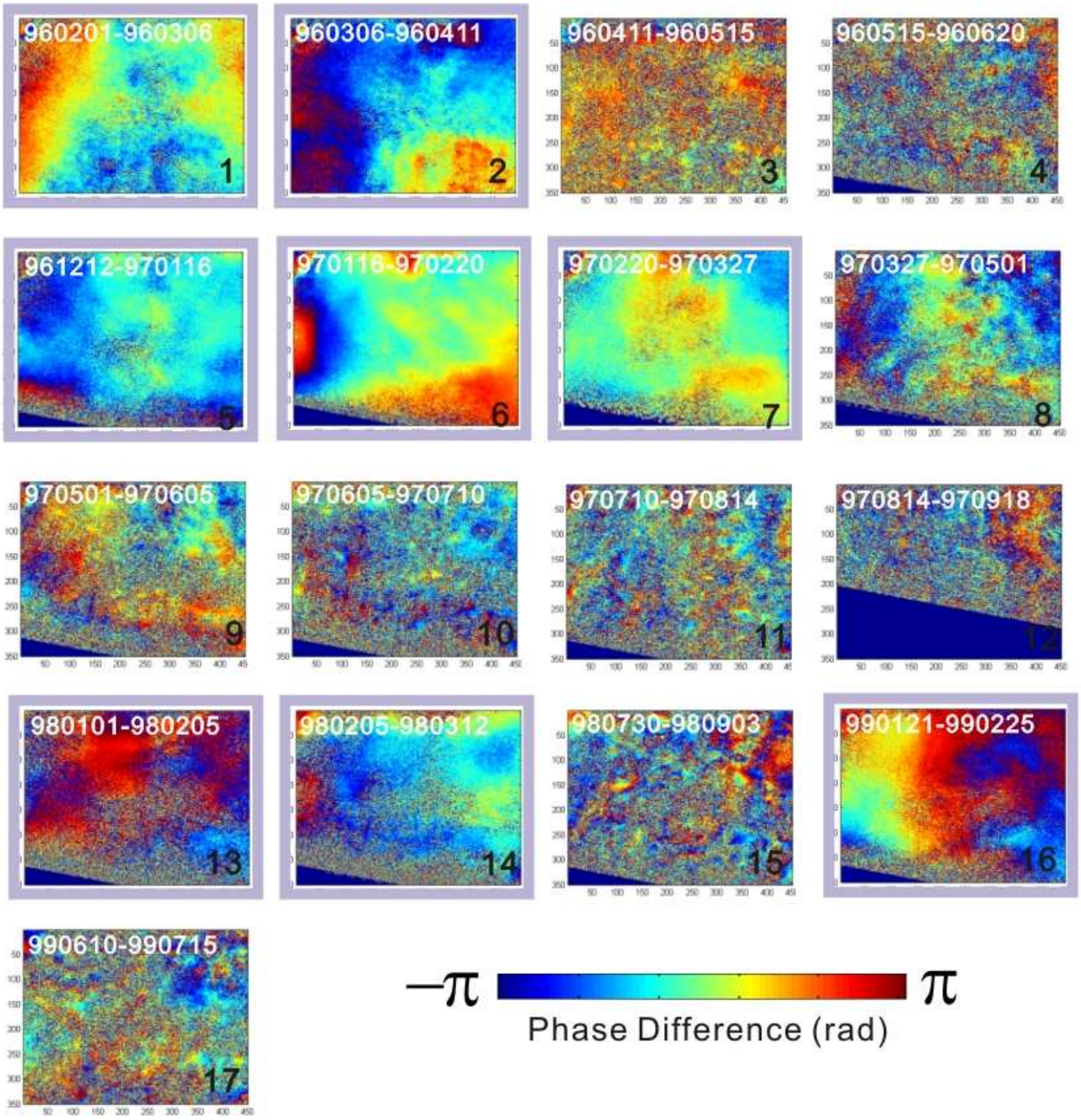

Figure 4.9. 17 interferograms produced with phase wrapped. Purple rectangular frames represent dry season interferograms for stacking in Figure 4.10.

This problem can be resolved by stacking several interferograms, hereby reducing the atmospheric noise component and obtaining the deformation in study area. 7 interferograms generated in dry seasons used to obtain the SRD rate in Yunlin area shows the same subsidence pattern with precise leveling data (Figure 4.10). Please note that the time interval of SRD rate is difference from precise leveling,

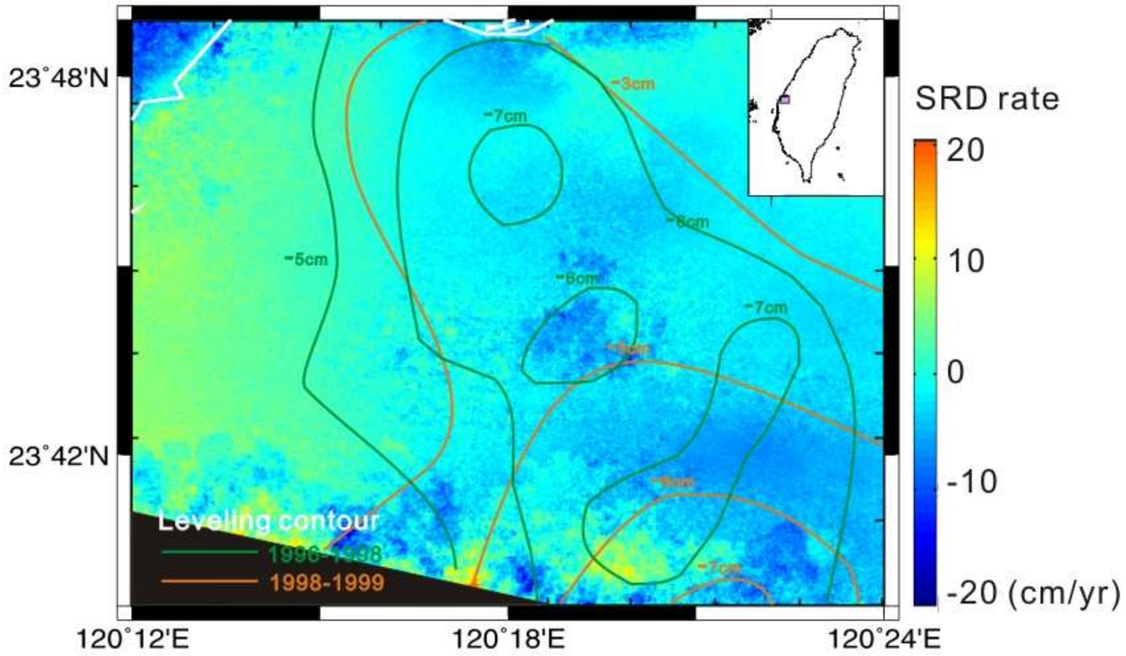

Figure 4.10. Unwrapped SRD rate for a stack of 7 interferograms of dry season and land subsidence contour from precise leveling data.

For the PSInSAR require, I select the master image using equation 2-10, and then generate 32 interferograms with 1997/06/05 (Figure 4.11). According to the dense vegetation in the study area, the 32 interferograms reveal less information of phase difference even the temporal baseline is small. However, most of the interferograms are full of perturbation that I am not able to observe any information of land subsidence.

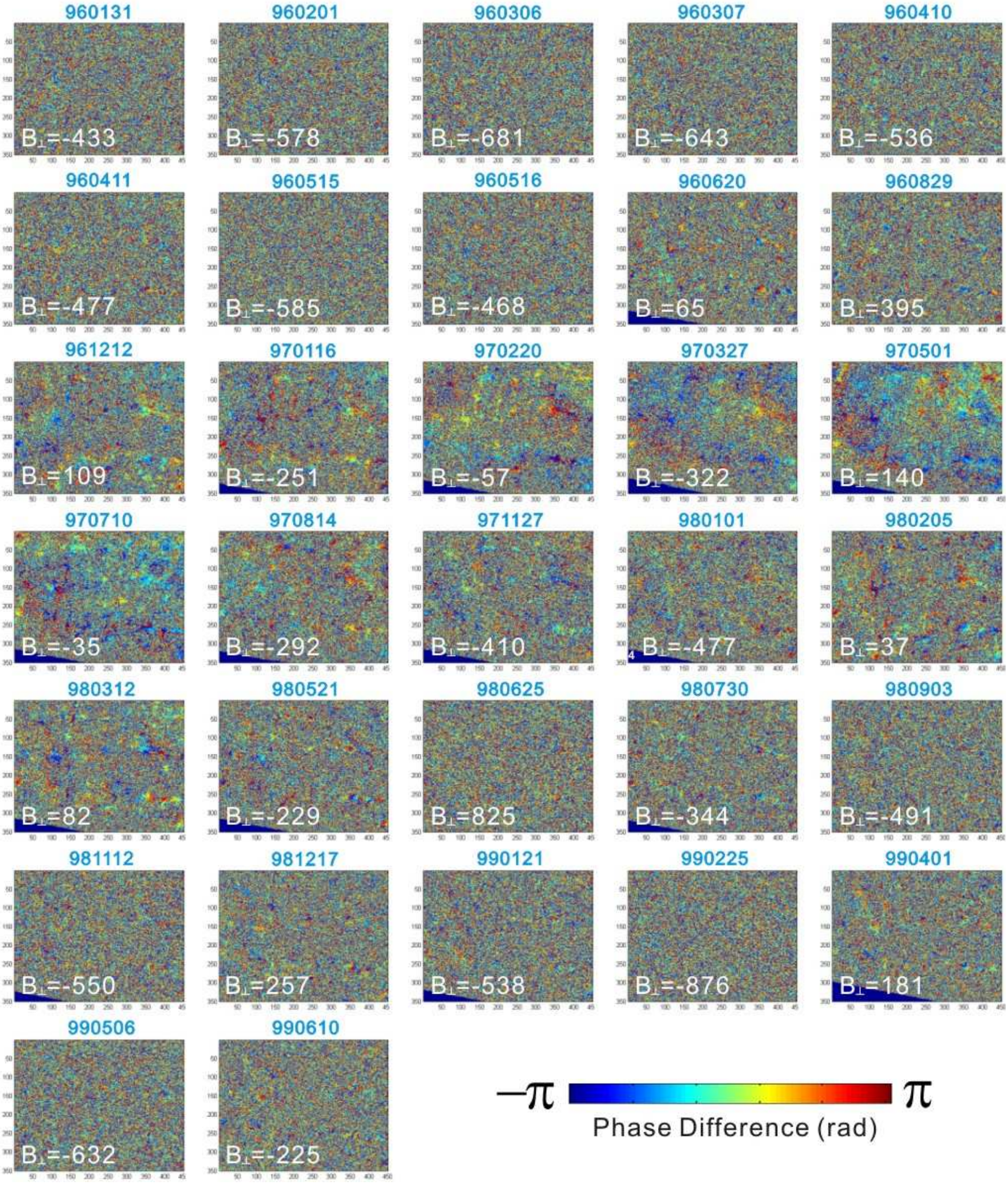

Figure 4.11. 32 interferograms produced with master image (5 June 1997) with phase wrapped.

4.3.3 Results of Land Subsidence by PSInAR

In this study, pixels with a stable coherence value higher than 0.3 in all data set have been selected to form PSC. There are 904 pixels have been chosen to connect using the Delaunay triangulation (Figure 4.12).

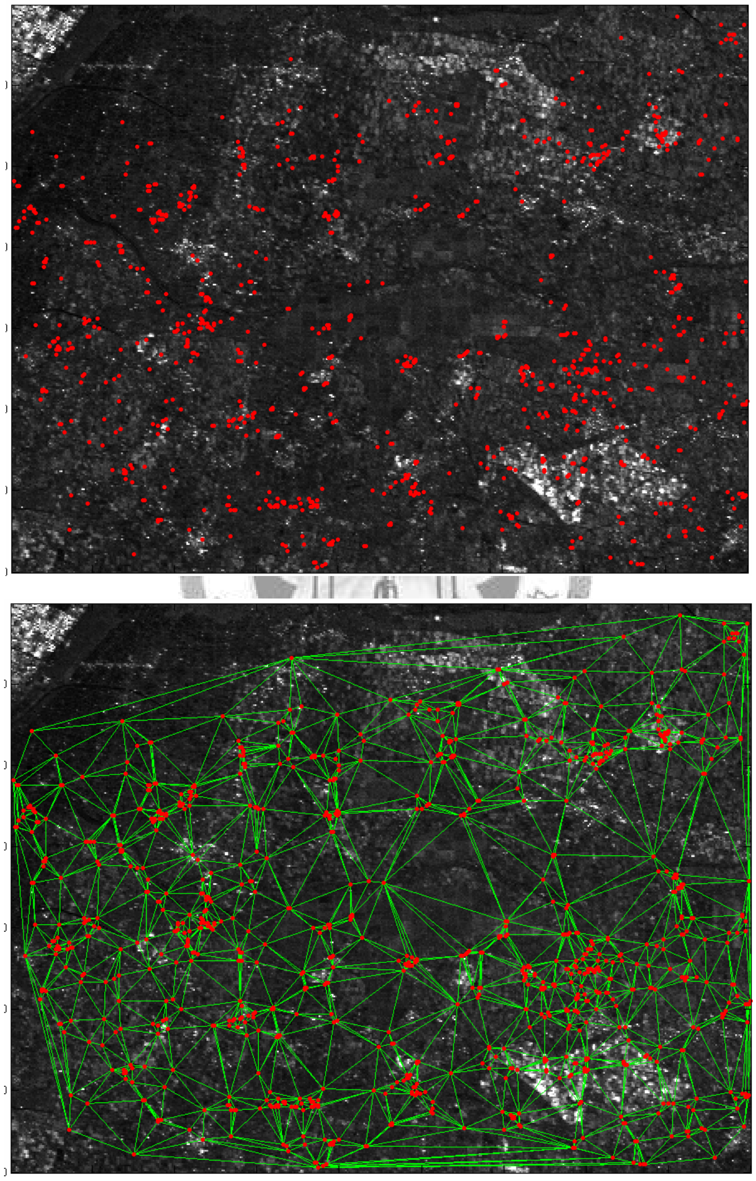

Figure 4.12. Selected points using (a) the coherence criterion and (b) the Delaunay Triangulations before removing the links over 1-km length above the amplitude image of the study area.

After processing the data using the algorithm for linear deformation estimation, there are 878 points remained from the initial 904 points according to the quality test. The details of slant range deformation rate relative to northeastern study area can be observed in Figure 4.13 and Table 4.3. According to the dense vegetation cover the whole study area, PSInSAR results only can be obtained around downtown areas (location 1 to 6 in Figure 4.13). However, the linear deformation measurement shows a similar pattern both with precise leveling and DInSAR result even the PS density is low (3.48 PS/km^2).

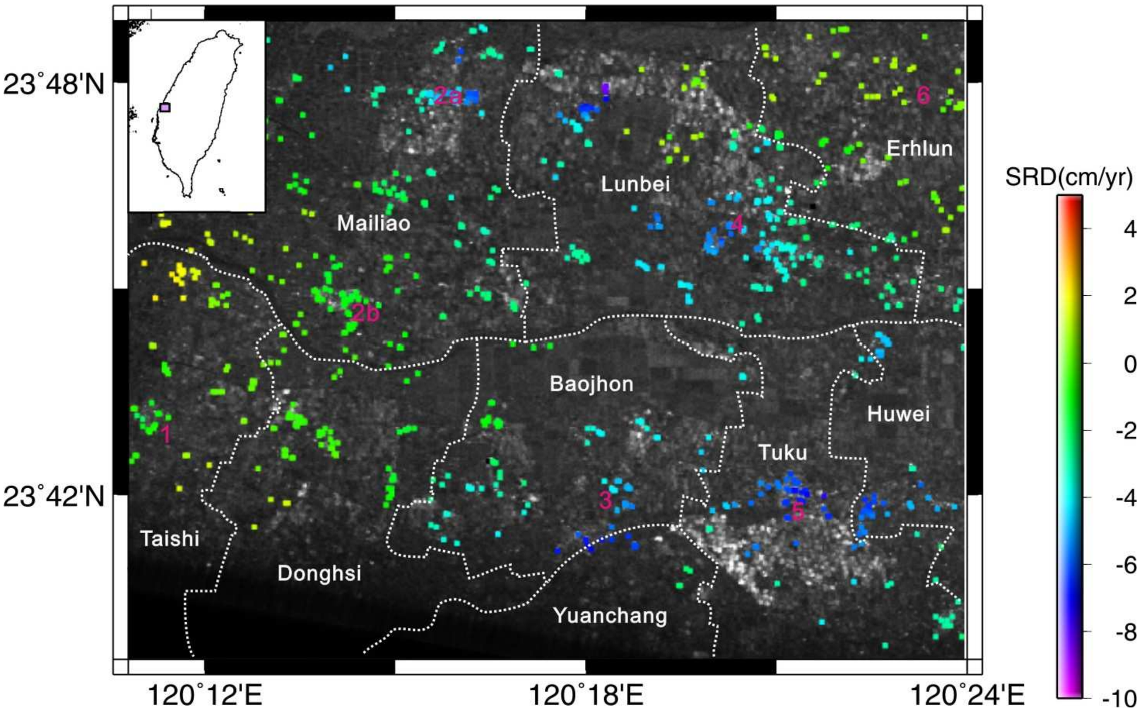

Figure 4.13. The rate of SRD (cm per year) from PS points of the study area superimposed on the amplitude image of SAR. White dot lines represent the township lines; Red numbers indicate the locations of downtown I chose.

Table 4.3 shows the average subsidence rate in six downtown areas respectively. Most area with serious subsidence located the inside Yunlin, especially in Baojhou and Tuku Township, where the conjunction of THSR and provincial Highway No.78 is just located on the eastern Tuku Township. On the contrary, the Taihai Township indicates a slower SRD rate of about -1.5 cm/yr during this time period. Moreover, the Lunbei Township reveals a decreasing subsidence rate from the eastern region to the western Lunbei, and an increasing SRD rate is predicted from the southern (-1.73 cm/yr) to the northern Mailiao (-5.18 cm/yr). This SRD rate is quite similar to the precise leveling distribution in Figure 4.7. In addition, the SRD rates are very coincidence within a downtown area that proves the confidence of our PSInSAR results.

Table 4.3. Average SRD rate of the downtown areas in study area.

	Township	Village	Downtown Area (km^2)	Subsidence Rate (cm/yr)
1	Taishi	x	1.00	-1.58
2a	Mailiao	Ciaotou	0.99	-5.18
2b		x	1.44	-1.73
3	Baojhon	x	3.20	-5.82
4	Lunbei	x	2.56	-5.00
5	Tuku	Maguang	4.00	-6.47
6	Erhlun	Youche	0.36	-0.35

4.4 Discussion

4.4.1 Comparison with Precise Leveling

Based on early repeat leveling results measured by ITRI, I chose You-Che Elementary School as the reference point with the minimum elevation change (location in Figure 4.14). Table 4.4 shows the subsidence variations of reference station and other three stations from October 1996 to February 1998. Therefore, I assume the SRD contributed only from land subsidence, and select three PS points close to these leveling stations. Figure 4.15 shows the deformation evolution of these PS points.

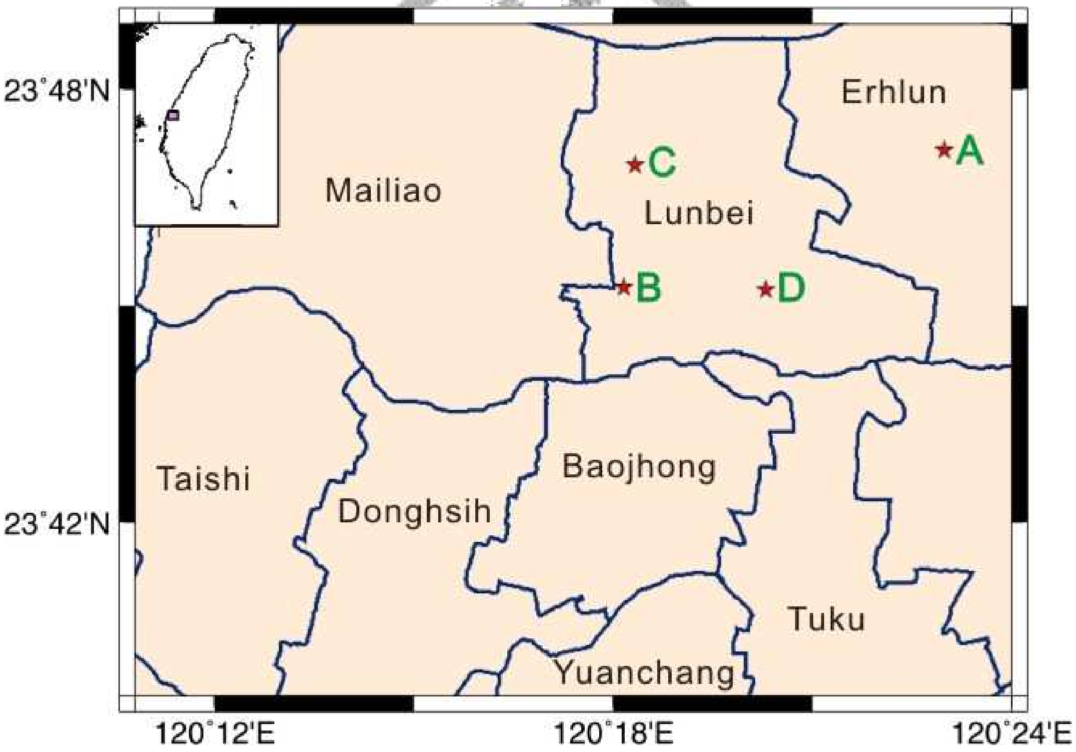

Figure 4.14. Location of precise leveling station: A: You-Che Elementary School; B: Da-You Elementary School; C: Feng-Rong 044; D: Lun-Bei 112M.

Table 4.4. Precise leveling measurements for four stations in Yunlin area from October 1996 to February 1998.

	Station Name	1996/10	1998/02	Subsidence value	Transfer to SRD value (cos23°)
A	You-Che Elementary School	1855.65 cm	1855.56 cm	0.09 cm	x
B	Da-You Elementary School	1000.03 cm	993.28 cm	6.75 cm	6.21 cm
C	Feng-Rong 044	986.08 cm	978.21 cm	7.87 cm	7.24 cm
D	Lun-Bei 112M	1580.76 cm	1571.36 cm	9.40 cm	8.65 cm

Assuming that land subsidence is the only contribution to SRD; transfer the vertical subsidence to SRD using trigonometric function. The subsidence distributions of these PS points reveal a coincident subsidence but slightly smaller than the data. However, not only vertical displacement but also horizontal displacement causes contribution to SRD. Thus, the subsidence in Yunlin area predicted by PS points should be underestimated.

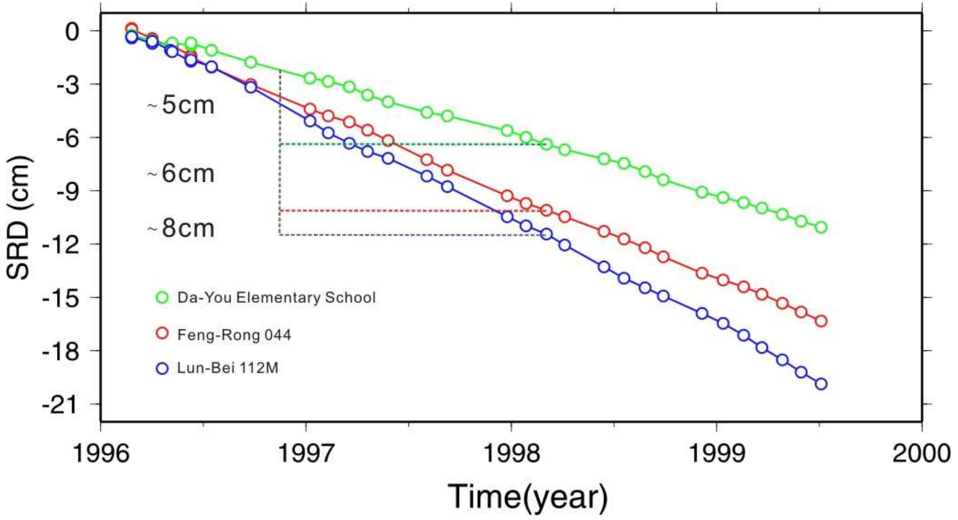

Figure 4.15. Deformation evolutions of three selected PS points near the precise leveling station.

4.4.2 Feasibility of InSAR Technique Apply on Yunlin County

In 4.3.2, I apply conventional DInSAR on Yunlin County, where the groundwater overpumping cause serious land subsidence. However, Yunlin County is one of the important agricultural production regions covered by dense vegetation and irrigation. In order to reduce the temporal and spatial decorrelation, I generate interferograms of 35 days each to obtain the most correlation between two SAR images. Moreover, due to the atmospheric affection cause huge perturbation in conventional interferograms, the stacking InSAR technique have used in advance to obtain the DInDAR results. Thus, the area of land subsidence can be observed.

Although the conventional DInSAR with stacking technique have already revealed coincident results with precise leveling measurements on the Yunlin County, one other goal of this study is to obtain the evolution on time serious. Thus, I apply PSInSAR technique here in 4.3.3. The result shows a similar distribution with both DInSAR in Figure 4.10 and precise leveling measurements in Figure 4.7 on the Yunlin County even in such a place with flourishing vegetation. Moreover, the subsidence evolution could be well demonstrated as long as the cut frequency is proper. On the other hand, considering each PS point to be a precise leveling or GPS station, this technique, I have proven that we can effective reduce labor and cost by using this technique apply on observing land subsidence in Yunlin County.

4.5 Summary

In order to overcome the spatial and temporal decorrelation caused by vegetation in Yunlin County. First, I stack 7 interferograms generated in dry seasons and obtain the SRD rate in Yunlin area. Second, the PSInSAR technique mentioned in previous chapter also have applied on here. The conclusions are listed in the followings:

1. The stacking InSAR result shows a concentrated subsidence inside Yunlin County, which is coincident with precise leveling data in Figure 4.7.
2. For the PSInSAR result, there are 878 points located around downtown area have been selected to compose the linear slant range displacement, and the pattern shows a similar pattern both with precise leveling and DInSAR result even the PS density is low (3.48 PS/km^2).
3. The most subsidence area located in Baojhou, Tuku Township and northern Mailiao with a subsidence rate of about 6 cm/yr along line of sight during 1996 to August 1999. Meanwhile, the Taishi Township located on the coastal area reveals a subsidence rate of 1.58 cm/yr.
4. Assume that SRD contributed only from land subsidence, the subsidence evolution reveals a coincident pattern but slight smaller than the data. However, without considering the horizontal displacement cause to SRD, the subsidence in Yunlin area predicted by PS points should be underestimated.
5. Both DInSAR and PSInSAR results have proven that we can effective reduce labor and cost by using this technique apply on observing land subsidence in Yunlin County.

Chapter 5

Conclusion and Future Work

5.1 Conclusions

In this study I have proven that both conventional DInSAR and PSInSAR technique can be a very effective method for measuring crustal deformation and land subsidence in Taiwan Island. Furthermore, PSInSAR technique overcomes the decorrelation problems by identifying stable point-wise targets whose echo is stronger enough to be trace in a series of interferograms. Thus, I apply this technique adopted from *Ferretti et al.* [2000] and *Mora et al.* [2003] to characterize the active deformation in Tainan Tableland (Chapter 3) and land subsidence in Yunlin County (Chapter 4) during the time period of 1996 to mid 1999.

In Chapter 3, the short-term SRD rates are 8 mm/yr on the central part of the Tainan Tableland and -10 mm/yr on the Tawan Lowland revealed by PSInSAR technique with 904 PS points (8.6 PS/km^2). After transferring SRD to vertical coordinate using GPS continuous measurements, the PS points close to the CK01 station represent a vertical velocity 5.1 mm/yr, which is very close to the long-term uplift rate from borehole data. Furthermore, the nonlinear deformation evolutions show a respectable correlation with seasonal rainfall near the Houchiali fault. Thus, the Houchiali fault might have a behavior of fault creeping during the rainy seasons. It is consistent with the observation of similar magnitude of long-term and short-term uplift rate at central part of the Tainan Tableland.

In Chapter 4, I apply both stacking DInSAR and PSInSAR to observe land subsidence contribution in the Yunlin County due to flourishing vegetation. Both of the results show an obvious concentrated subsidence pattern in Baojhou, Tuku Township and northern Mailiao inside Yunlin County, which is quite consistent with precise leveling data measured after 1996 even though the PS density is low (3.48 PS/km^2). Thus, both DInSAR and PSInSAR technique can effectively reduce labor and cost on observing land subsidence in Taiwan Island.

Both of the results in two case studies have proven that the PSInSAR technique I used can be a reliable measuring tool applies on Taiwan Island. Here, I list some suggestions to improve this processing to get the better results. Then, combining the GPS and precise leveling measurements, this technique can be a potential tool to observe the crustal deformation even in mountain area.

5.2 Future Directions

According to PSInSAR is still a developing technique, there are many group have keep publish the new algorithm such as StaMPS by *Hooper et al.* [2006], SBAS by *Berardino et al.* [2002], and *Liu et al.* [2008]. In the future, I will try to combine these different methods and retain proper algorithm for Taiwan Island. Followings are some ideas:

1. For the vegetation area like the Yunlin County, we can quote the idea of SBAS from *Berardino et al.* [2002] to enhance the correlation between each interferogram. Thus, more PS points could be generated to reduce the discontinuous of phase changes.
2. Using PS-Network method developed by *Liu et al.* [2008] to connect each two PS candidates for better calibrating the linear velocity fitness.
3. Calculating the DEM error and linear deformation velocity respectively by using idea from *Hooper et al.* [2004] in case of interfering with each other during coregistering the linear deformation.

4. Finding out the suitable cut frequency for isolate the contribution of nonlinear deformation from atmospheric delay; On the other hand, the **E**mpirical **M**ode **D**ecomposition (**EMD**) is also another method to procure this destination.

Furthermore, due to the successful in Yunlin area, the PSInSAR technique has been proven that using this pixel-by-pixel analysis can overcome the spatial decorrelation caused by dense vegetation. Thus, applying PSInSAR technique to mountain area will not be a difficult task. In addition, the L-band satellite is also an effective source to monitor the surface which with dense vegetation.

國立臺灣大學
敦品 · 勵學 · 愛國 · 愛人

Reference

Amelung, F., Oppenheimer, C., Segall, P. and Zebker, H., 2000. Ground deformation near Gada 'Ale Volcano, Afar, observed by Radar Interferometry. *Geophysical Research Letters*, 27(19): 3093-3096.

Angelier, J., Lee, J.C., Chu, H.T., Hu, J.C., Lu, C.Y., Chan, Y.C., Lin, T.J., Font, Y., Deffontaines, B. and Tsai, Y.B., 2001. Le Séisme de Chichi (1999) et sa place dans l'oregène de Taiwan. *Comptes Rendus de l'Academie des Sciences Series IIA Earth and Planetary Science:* 333, 5-21.

Berardino, P., Fornaro, G., Lanari, R. and Sansosti, E., 2002. A new algorithm for surface deformation monitoring based on small baseline differential SAR interferograms. *IEEE Transactions on Geoscience and Remote Sensing*, 40(11): 2375-2383.

Bürgmann, R., Rosen, P.A. and Fielding, E.J., 2000. Synthetic aperture radar interferometry to measure Earth's surface topography and its deformation. *Annual Review of Earth and Planetary Sciences*, 28: 169-209.

Chang, C.C. and Wang, T.N., 2006. GPS monitoring ground subsidence associated with seasonal underground water level decline: case analysis for a section of Taiwan High Speed Rail. *Surveying and Land Information Science*, 66(1): 45-54.

Chang, C.P., Wang, C.T., Chang, T.Y., Chen, K.S., Liang, L.S., Pathier, E. and Angelier, J., 2004. Application of SAR interferometry to a large thrust deformation: the 1999 M-w=7.6 Chichi earthquake in central Taiwan. *Geophysical Journal International*, 159(1): 9-16.

Chang, L., 2005. Subsurface structure features of Houchiali Fault (in Chinese). *Unpublished Master Thesis*, Institute of Seismology, National Chung Cheng University, Chia-Yi, 85p.

Chen, C.W. and Zebker, H.A., 2002. Phase unwrapping for large SAR interferograms: Statistical segmentation and generalized network models. *IEEE Transactions on Geoscience and Remote Sensing*, 40(8): 1709-1719.

Chen, Y.G., 1993. Sea-level change and neotectonics in southern part of Taiwan region since late Pleistocene (in Chinese with English abstract). *Unpublished Ph. D. Dissertation*, Department of Geosciences, National Taiwan University, Taipei, 158p.

Chen, Y.G. and Liu, T.K., 2000. Holocene uplift and subsidence along an active tectonic margin southwestern Taiwan. *Quaternary Science Reviews*, 19(9): 923-930.

Ching, K.E., Rau, R.J., Lee, J.C. and Hu, J.C., 2007. Contemporary deformation of tectonic escape in SW Taiwan from GPS observations, 1995-2005. *Earth and Planetary Science Letters*, 262(3-4): 601-619.

Colesanti, C., Ferretti, A., Prati, C. and Rocca, F., 2003. Monitoring landslides and tectonic motions with the Permanent Scatterers Technique. *Engineering Geology*, 68(1-2): 3-14.

Curlander, J.C. and Mcdonough, R.N., 1991. Syntheic Aperture Radar: Systems and Signal Processing. *John Wiley & Sons, Inc*, New York.

Deffontaines, B., Lacombe, O., Angelier, J., Chu, H.T., Mouthereau, F., Lee, C.T., Deramond, J., Lee, J.F., Yu, M.S. and Liew, P.M., 1997. Quaternary transfer faulting in the Taiwan Foothills: Evidence from a multisource approach. *Tectonophysics*, 274(1-3): 61-82.

Elachi, C. 1988. Spaceborne Radar Remote Sensing: Applications and Techniques. *Institute of Electrical and Electronics Engineers*, New York.

Ferretti, A., Prati, C. and Rocca, F., 2000. Nonlinear subsidence rate estimation using permanent scatterers in differential SAR interferometry. *IEEE Transactions on Geoscience and Remote Sensing*, 38(5): 2202-2212.

Ferretti, A., Prati, C. and Rocca, F., 2001. Permanent scatterers in SAR interferometry. *IEEE Transactions on Geoscience and Remote Sensing*, 39(1): 8-20.

Fruneau, B., Pathier, E., Raymond, D., Deffontaines, B., Lee, C.T., Wang, H.T., Angelier, J., Rudant, J.P. and Chang, C.P., 2001. Uplift of Tainan Tableland (SW

Taiwan) revealed by SAR interferometry. *Geophysical Research Letters*, 28(16): 3071-3074.

Goldstein, R.M., Engelhardt, H., Kamb, B. and Frolich, R.M., 1993. Satellite radar interferometry for monitoring ice-sheet motion: Application to an Antarctic ice stream. *Science*, 262(5139): 1525-1530.

Hanssen, R.F., 2001. Radar Interferometry: Data Interpretation and Error Analysis. *Kluwer Academic*, Dordrecht.

Hashimoto, W., 1972. Problems on the Tainan Formation and related formations, brought about C-14 dating. *Acta Geologica Taiwanica*, 15: 51-62.

Ho, C.S., 1975. An introduction to the geology of Taiwan explanatory text of the geologic map of Taiwan. *Ministry of Economic Affairs*, Taipei, Taiwan, Republic of China.

Ho, S.C., 2006. Application of space geodetic measurements to the surface deformation of Tainan Tableland, Southwestern Taiwan (in Chinese with English abstract). *Unpublished Master Thesis*, Institute of Geophysics, National Central University, Chungli, 142p.

Hooper, A., Zebker, H., Segall, P. and Kampes, B., 2004. A new method for measuring deformation on volcanoes and other natural terrains using InSAR persistent scatterers. *Geophysical Research Letters*, 31(23), L23611:1-5.

Hooper, A., 2006. Persistent scatterer radar interferometry for crustal deformation studies and modeling of volcanic deformation. *Unpublished Ph. D. Dissertation*, Institute of Geophysics, Stanford University, USA, 144p.

Hsieh, S.H., 1972. Subsurface geology and gravity anomalies of theTainan and Chungchou structures of the coastal plain of southwestern Taiwan. *Petroleum Geology of Taiwan*, 10: 323-338.

Hu, J.C., Yu, S.B., Angelier, J. and Chu H.T., 2001. Active deformation of Taiwan from GPS measurements and numerical simulations. *Journal of Geophysical Research*, 106: 2265-2280.

Huang, M.H., 2006. The case studies of the crustal deformation in Taiwan based on SAR interferometry. *Unpublished Master Thesis*, Department of Geosciences, National Taiwan University, Taipei, 185pp.

Huang, M.H., Hu, J.C., Hsieh, C.S., Ching, K.E., Rau, R.J., Pathier, E., Fruneau, B. and Deffontaines, B., 2006. A growing structure near the deformation front in SW Taiwan as deduced from SAR interferometry and geodetic observation. *Geophysical Research Letters*, 33(12), L12305:1-5.

Huang, S.T., Yang, K.M., Hung, J.H., Wu, J.C., Ting, H.H., Mei, W.W., Hsu, S.H. and Lee, M., 2004. Deformation front development at the northeast margin of the Tainan basin, Tainan-Kaohsiung area, Taiwan. *Marine Geophysical Researches*, 25(1-2): 139-156.

Kampes, B.M., 2005. Radar Interferometry: Persistent Scatterer Technique. *Springer*, Germany.

Knöpfle, W., Strunz, G. and Roth, A., 1998. Mosaicking of Digital Elevation Models derived by SAR Interferometry. *International Archives of Photogrammetry and Remote Sensing*, 32(4): 306-313.

Kuo, H.Y., Wang, C.Y., Chiu, G.T. and Lee, C.Y., 1998. Houchiali Fault: An active fault? (in Chinese). *7th Conference of Geophysics Society, Taiwan Region*: 429-437.

Lacombe, O., Mouthereau, F., Deffontaines, B., Angelier, J., Chu, H.T. and Lee, C.T., 1999. Geometry and Quaternary kinematics of fold-and-thrust units of southwestern Taiwan. *Tectonics*, 18(6): 1198-1223.

Lee, Y.S., Hsei, K.S., Huang, T.Y., Ho, T.T., Chen, H.W. and Chang, H.C., 1999. Evolution of Foreland basin, southwestern Taiwan. *1999 Annual Meeting of China Geology Society*: 246-248.

Lin, A.T.S., 2001. Cenozoic stratigraphy and tectonic development of the west Taiwan basin. *Unpublished Ph. D. Dissertation*, University of Oxford, 246p.

Lin, A.T. and Watts, A.B., 2002. Origin of the West Taiwan basin by orogenic loading and flexure of a rifted continental margin. *Journal of Geophysical Research-Solid Earth*, 107(B9).

Lin, C.C., 1957. Geomorphology of Taiwan. *Committee of Historical Archives of Taiwan Province*, 424 pp.

Lin, C.C., 1963. Quaternary in Taiwan. *Taiwan Hisotrica*, 14(1):1-53; 14(2):13-51.

Lin, C.C., 1969. Holocene geology of Taiwan. *Acta Geologica Taiwanica*, 13: 83-126.

Liu, C.H., Pan, Y.W., Liao, J.J., Huang, C.T. and Ouyang, S., 2004. Characterization of land subsidence in the Choshui River alluvial fan, Taiwan. *Environmental Geology*, 45(8): 1154-1166.

Liu, C.W., Lin, W.S., Shang, C. and Liu, S.H., 2000. The effect of clay dehydration on land subsidence in the Yun-Lin coastal area, Taiwan. *Environmental Geology*, 40(4-5): 518-527.

Land Subsidence Database, Water Resources Agency, Ministry of Economic Affairs, and Industrial Technology Research Institute. http://www.subsidence.org.tw/.

LSPRC (Land Subsidence Prevention and Reclamation Corps), 2007. Land subsidence potential analysis and warning system development (in Chinese). *Report of Water Resource Agency*, Taipei.

Massonnet, D. and Feigl, K.L., 1998. Radar interferometry and its application to changes in the earth's surface. *Reviews of Geophysics*, 36(4): 441-500.

Massonnet, D., Rossi, M., Carmona, C., Adragna, F., Peltzer, G., Feigl, K. and Rabaute, T., 1993. The displacement field of the Landers earthquake mapped by radar interferometry. *Nature*, 364(6433): 138-142.

Mora, O., Mallorqui, J.J. and Broquetas, A., 2003. Linear and nonlinear terrain deformation maps from a reduced set of interferometric SAR images. *IEEE Transactions on Geoscience and Remote Sensing*, 41(10): 2243-2253.

Mouthereau, F., Deffontaines, B., Lacombe, O. and Angelier, J., 2002. Variations along the strike of the Taiwan thrust belt: Basement control on structural style, wedge geometry, and kinematics. In *Geology and Geophysics of an Arc-Continent Collision, Taiwan*, edited by Byrne, T.B. and Liu, C.S., *Geological Society of America*, Special Paper 358(31-54).

Mouthereau, F., Lacombe, O., Deffontaines, B., Angelier, J. and Chu, H.T., 1999. Quaternary transfer faulting and belt front deformation at Pakuashan (western Taiwan). *Tectonics*, 18(2): 215-230.

Pathier, E., Fruneau, B., Deffontaines, B., Angelier, J., Chang, C.P., Yu, S.B. and Lee, C.T., 2003. Coseismic displacements of the footwall of the Chelungpu fault caused by the 1999, Taiwan, Chi-Chi earthquake from InSAR and GPS data, *Earth Planet Science Letters*, 212: 73-88.

Rau, R.J., Ching, K.E., Hsieh, T.J., Yu, C.I., Hou, C.S., Lee, Y.H., Hu, J.C., Chan, J.C., Lee, J.C., Hung, J.H. and Lin, C.W., 2004. Surface deformation and earthquake potential of Tainan Tableland, southwestern Taiwan. *Special Publication, Central Geological Survey*, 14: 147-156.

Rogers, A.E.E. and Ingalls, R.P., 1969. Venus - mapping surface reflectivity by radar interferometry. *Science*, 165(3895): 797-799.

Rosen, P.A., Hensley, S., Joughin, I.R., Li, F.K., Madsen, S.N., Rodriguez, E. and Goldstein, R.M., 2000. Synthetic aperture radar interferometry - Invited paper. *Proceedings of the IEEE*, 88(3): 333-382.

Rumsey, H.C., Morris, G.A., Green, R.R. and Goldstei.Rm, 1974. Radar brightness and altitude image of a portion of Venus. *Icarus*, 23(1): 1-7.

Sun, R., Sung, Q.C. and Liu, T.K., 1998. Near-surface evidence of recent Taiwan Orogeny detected by a shallow seismic method. *Earth and Planetary Science Letters*, 163(1-4): 291-300.

Sun, S.C., 1964. Photogeologic study of Tainan-Kaohsiung Coastal plain area. *Petroleum Geology of Taiwan*, 3: 39-51.

Tang, C.P. and Tang, S.Y., 2006. Democratization and capacity building for environmental governance: managing land subsidence in Taiwan. *Environment* *and Planning A*, 38(6): 1131-1147.

Teng, L.S., 1987. Stratigraphic records of the late Cenozoic Penglai orogeny of Taiwan. *Acta Geologica Taiwanica*, 25: 205-224.

TPWCB (Taiwan Provincial Water Conservancy Bureau), 1990. Investigation on the ground water level and land subsidence in the multi-level subsidence monitoring well located in Chuoshui alluvial fan, Taiwan (in Chinese). *TPWCB*, Taiwan.

TPWCB (Taiwan Provincial Water Conservancy Bureau), 1997. Project of investigation of land subsidence in the coastal area of western Taiwan and I-Lan county－ investigation of land subsidence in the Yun-Lin area (in Chinese). *TPWCB*, Taiwan.

Wu, T.J., 1990. ^{14}C dating and neotectonic implications of the Tainan Formation on Tainan Tableland (in Chinese). *Unpublished Master Thesis*, Department of Geology, National Taiwan University, Taipei, 71p.

Wu, T.J., Chen, Y.G. and Liu, T.K., 1992. Sedimentary history and neotectonic implication of Tainan formation on Tainan Tableland (in Chinese, with English abstract). *Ti-Chih*, 12(2): 167-184.

Yu, S.B., Chen, H.Y. and Kuo, L.C., 1997. Velocity field of GPS stations in the Taiwan area. *Tectonophysics*, 274(1-3): 41-59.

Yu, S.B., Kuo, L.C., Punongbayan, R.S. and Ramos, E.G., 1999. GPS observation of crustal deformation in the Taiwan-Luzon region. *Geophysical Research Letters*, 26(7): 923-926.

Zang, S.X., Chen, Q.Y., Ning, J.Y., Shen, Z.K. and Liu, Y.G., 2002. Motion of the Philippine Sea plate consistent with the NUVEL-1A model. *Geophysical Journal International*, 150(3): 809-819.

Zebker, H.A. and Goldstein, R.M., 1986. Topographic mapping from interferometric synthetic aperture radar observations. *Journal of Geophysical Research-Solid Earth and Planets*, 91(B5): 4993-4999.

Zebker, H.A., Rosen, P.A., Goldstein, R.M., Gabriel, A. and Werner, C.L., 1994. On the derivation of coseismic displacement-fields using differential radar interferometry: The Landers earthquake. *Journal of Geophysical Research-Solid Earth*, 99(B10): 19617-19634.

Zebker, H.A. and Villasenor, J., 1992. Decorrelation in interferometric radar echoes. *IEEE Transactions on Geoscience and Remote Sensing*, 30(5): 950-959.

Zhang, Z.C., 2005. Plan our country water resources policy: take Yunlin County as the example (in Chinese, with English abstract). *Unpublished Master Thesis*, National Sun Yat-sen University, Kaohsiung, 92p.

Zhou, F.H., 2007. Active structure of fold-and-thrust belt deduced by sequence stratigraphy analysis during the Holocene, Tainan(in Chinese, with English abstract). *Unpublished Master Thesis*, Department of Geology, National Taiwan University, Taipei, 115p.

Zisk, S.H., 1972. Lunar Topography - First radar-interferometer measurements of Alphonsus-Ptolemaeus-Arzachel region. *Science*, 178(4064): 977-980.

Appendix A

Followings are MATLAB programs and parameters I used in this study:

	programs	process	parameter
1	select_PSC_coh.m	*2.4.3* Persistent scatterers identificationn	coh >= 0.3
2	Mora_triangle.m	*2.4.4* Delauney triangulation	x
3	Mora_pha_diff.m	*2.4.4* Calculating phase difference between 2 PS	x
4	Mora_best_solu.m	*2.4.4* Linear model adjustment	**Chapter 3** h_int = 1; % 1 m v_int = 0.001; % 1 mm range = 300000; % r×sin(23) v = 1:61 % +- 3cm h = 1:41 % +- 20m **Chapter 4** h_int = 1; % 1 m v_int = 0.0025; % 2.5 mm range = 300000; % r×sin(23) v = 1:81 % +- 10cm h = 1:21 % +- 10m
5	Mora_lin.m	*2.4.4* Least mean square	ga >= 0.7
6	Mora_res.m	*2.4.5* Calculating phase residual	x
7	Ferr_atmos.m	*2.4.5* Isolating nonlinear deformation from atmospheric phase	x
8	def.m	*Step 5)* Integrating linear and nonlinear deformation	x